Characterization of testosterone and androgen receptor action in human and rhesus macaque heart muscle cells

Dissertation

for the award of the degree

"Doctor rerum naturalium"

of the Georg-August-Universität Göttingen

within the doctoral program of the IMPRS Molecular Biology

of the Georg-August University School of Science (GAUSS)

submitted by

Yuliia Tereshchenko

from Mykolaiv, Ukraine

Göttingen 2024

Thesis Advisory Committee:

Prof. Dr. Rüdiger Behr, Platform Degenerative Diseases, German Primate Center (Deutsches Primatenzentrum, DPZ), Göttingen.

Prof. Dr. Stefan Jakobs, Research group Structure and Dynamics of Mitochondria, Max Planck Institute for Multidisciplinary Sciences, Göttingen.

Dr. Ufuk Günesdogan, Department Developmental Biology, Göttingen Center for Molecular Biosciences, Göttingen.

Prof. Dr. Kathrin Streckfuß-Bömeke, Institute of Pharmacology and Toxicology, Würzburg University, Würzburg.

Members of the Examination Board:

Referee: Prof. Dr. Rüdiger Behr, Platform Degenerative Diseases, German Primate Center (Deutsches Primatenzentrum, DPZ), Göttingen.

2nd Referee: Prof. Dr. Stefan Jakobs, Research group Structure and Dynamics of Mitochondria, Max Planck Institute for Multidisciplinary Sciences, Göttingen.

Further members of the examination board:

Dr. Ufuk Günesdogan, Department Developmental Biology, Göttingen Center for Molecular Biosciences, Göttingen.

Prof. Dr. Lutz Walter, Department of Primate Genetics, German Primate Center, Göttingen.

Prof. Dr. Kai Tittmann, Department of Molecular Enzymology, Schwann-Schleiden Research Center, Göttingen.

Dr. Michael Heide, Platform Degenerative Diseases, German Primate Center, Göttingen.

Date of oral examination: 13th March 2024

Table of Contents

1 Abstract

Androgens are sex steroid hormones that influence various processes in reproductive tissues and peripheral organs. Their lipophilic nature enables free diffusion through the plasma membrane. In the cytoplasm, testosterone (T) binds to its receptor, the androgen receptor (AR), and the complex then translocates to the nucleus for activation or inhibition of gene expression. Although the effects of androgens are studied greatly in healthy and diseased reproductive tissues, little is known about their cellular and molecular action in the cardiovascular system. Clinical research reported the impact of high and low T levels on the human heart and vasculature, but the data are currently conflicting. Additionally, most of the molecular and cellular processes triggered by androgens in heart muscle cells were researched using rodents. These models vastly contributed to our understanding of biological processes, though are partially limited due to differences in heart physiology to humans. This work focused on studying the impact of male physiological (25 nM) and supraphysiological (100 nM) concentrations of T on primate cardiomyocytes (CMs) of human and rhesus macaque origin. For the first time, AR was detected in CM nuclei of male rhesus macaque tissue. Notably, no signal was detected in female heart cells. For further *in vitro* studies we used an induced pluripotent stem cell (iPSC) model. AR was detected in human and rhesus macaque iPSCs and was induced and translocated by T. A directed cardiac differentiation protocol was optimized and used to generate CMs from male and female human and rhesus macaque cell lines. Non-treated cells showed cytoplasmic AR staining while T-treated cells displayed mostly nuclear signals. T treatment induced AR abundance in male rhesus iPSCs and iPSC-CMs. Interestingly, we detected an AR-V7 isoform with no T-binding capabilities in human iPSC-CMs and human left ventricular tissue. Since T may also exhibit AR-independent action, we generated a clonal AR knock-out (KO) human male iPSC line to investigate AR-independent effects. Further analysis of the AR KO cell line showed fewer CMs generated after differentiation, a higher proliferation rate, and a more disorganized contractile apparatus compared with wild-type (WT) cells. The analysis of differentially expressed genes in KO and WT cells further highlighted a more immature state of KO CMs. While 24 hours of T treatment resulted in a decrease in Ca^{2+} current density, 48 hours of exposure did not result in significant changes between treated and non-treated groups of WT cells. Overall, the data has shown a more drastic effect of the AR KO itself than T treatment. That is why we hypothesized T conversion to other androgens. LC-MS/MS analysis demonstrated low levels of T in cell culture media 48 hours after T addition confirming our assumption. Moreover, androstenedione, a weaker androgen than T, was detected in human samples, but almost none in rhesus. In conclusion, this work demonstrates relevant effects of the T / AR system on proliferation, cytoskeleton organization, electrophysiological parameters, and gene expression of primate CMs.

2 Abbreviations

2-NBDG	2-(7-Nitro-2,1,3-benzoxadiazol-4-yl)-D-glucosamine
4E-BP1	Eukaryotic translation initiation factor 4e-binding protein 1
AAS	Androgenic anabolic steroids
Akt	Protein kinase B
AMPK	AMP-activated protein kinase
ANGPT1	Angiopoietin-1
ANOVA	Analysis of variance
AP-2α	Activating protein-2 alpha
APC	Allophycocyanin
AR	Androgen receptor
ARE	Androgen response element
AR-FL	Androgen receptor full-length
AR-V7	Androgen receptor variant 7
ARVC	Arrhythmogenic right ventricular cardiomyopathy
AMP	Adenosine triphosphate
BMP4	Bone morphogenetic protein 4
BSA	Bovine serum albumin
CaMKII	Calcium/calmodulin-dependent protein kinase II
CAMK2B	Calcium/calmodulin-dependent protein kinase II beta
cAMP	Cyclic adenosine monophosphate
CDK1	Cyclin-dependent kinase 1
CES1	Carboxylesterase 1
c-Myc	Cellular myelocytomatosis proto-oncogene
COL11A1	Collagen type XI alpha 1 chain
COL12A1	Collagen type XII alpha 1 chain
COL1A1	Collagen type I alpha 1 chain
COL1A2	Collagen type I alpha 2 chain
COL6A2	Collagen type VI alpha 2 chain
COL6A3	Collagen type VI alpha 3 chain
COL9A3	Collagen type IX alpha 3 chain
COS-1	CV-1 in origin with SV40 genetic material
CRISPR	Clustered regularly interspaced short palindromic repeats
CRYAA	Crystallin alpha A
CRYBA1	Crystallin beta A1
CRYBA2	Crystallin beta A2
CRYBA4	Crystallin beta A4

CRYBB1	Crystallin beta B1
CRYBB2	Crystallin beta B2
CRYBB3	Crystallin beta B3
CRYGC	Crystallin gamma C
CRYGD	Crystallin gamma D
CRYGS	Crystallin gamma S
cTNT	Cardiac troponin T
Cx43	Connexin 43
CYP19A1	Cytochrome P450 family 19 subfamily A member 1
DAB	3,3'-Diaminobenzidine
DAPI	4',6-Diamidino-2-phenylindole
DHEA	Dehydroepiandrosterone
DHEAS	Dehydroepiandrosterone sulfate
DHT	Dihydrotestosterone
DMEM	Dulbecco's modified eagle medium
DMSO	Dimethyl sulfoxide
DPBS	Dulbecco's phosphate-buffered saline
DTT	Dithiothreitol
ECL	Enhanced chemiluminescence
EDTA	Ethylenediaminetetraacetic acid
EGTA	Ethylene glycol-bis(β-aminoethyl ether)-N,N,N',N'-tetraacetic acid
EIA	Enzyme immunoassay
ELISA	Enzyme-linked immunosorbent assay
ERK1/2	Extracellular signal-regulated kinase 1/2
ESC	Embryonic stem cell
estradiol-6-CMO-BSA	6-Carboxymethoxyestradiol-17-BSA
EZH2	Enhancer of zeste homolog 2
FACS	Fluorescence-activated cell sorting
FBN1	Fibrillin-1
FITC	Fluorescein isothiocyanate
FOXA1	Forkhead box A1
GAPDH	Glyceraldehyde 3-phosphate dehydrogenase
GATA2	GATA binding protein 2
GFP	Green fluorescent protein
GLUT4	Glucose transporter 4
HAND1	Heart- and neural crest derivatives-expressed protein 1

HCN2	Hyperpolarization-activated cyclic nucleotide-gated channel 2
HDAC4/5	Histone deacetylase 4/5
HEPES	4-(2-Hydroxyethyl)-1-piperazineethanesulfonic acid
HF	Heart failure
HNF4A	Hepatocyte nuclear factor 4 alpha
HPG axis	Hypothalamic-pituitary-gonadal axis
HRP	Horseradish peroxidase
ICH	Immunohistochemistry
IF	Immunofluorescence
IGF2	Insulin-like growth factor 2
iPSC	Induced pluripotent stem cell
IWR-1	Inhibitor of Wnt response 1
KCNC3	Potassium voltage-gated channel subfamily C member 3
KCNIP	Potassium voltage-gated channel interacting protein
KLF4	Krüppel-like factor 4
KO	Knockout
LA	Left atria
LC-MS/MS	Liquid chromatography-tandem mass spectrometry
LIN28A	Lin-28 homolog A
MAPK11	Mitogen-activated protein kinase 11
MBTE	Mitochondrial biogenesis transcription factor E
MEF2	Myocyte enhancer factor 2
MEK	Mitogen-activated protein kinase kinase
MLC2a	Myosin light chain 2 atrial
MLC2v	Myosin light chain 2 ventricular
mTORC1	mammalian target of rapamycin complex 1
MYH11	Myosin heavy chain 11
MYH6	Myosin heavy chain 6
NHP	Non-human primate
OCT4A	Octamer-binding transcription factor 4
p300	E1A-binding protein p300
PCR	Polymerase chain reaction
PFA	Paraformaldehyde
PI3K	Phosphoinositide 3-kinase
PIAS1	Protein inhibitor of activated STAT 1
PNK	Polynucleotide kinase
PPARc	Peroxisome proliferator-activated receptor gamma

PSC	Pro-survival compound
RIPA	Radioimmunoprecipitation assay buffer
RPMI	Roswell Park Memorial Institute
RT	Room temperature
RT-qPCR	Reverse transcription-quantitative polymerase chain reaction
RXRG	Retinoid X receptor gamma
S6K1	Ribosomal protein S6 kinase beta-1
SALL4	Sal-like protein 4
SD	Standard deviation
SDS	Sodium dodecyl sulfate
SDS-PAGE	Sodium dodecyl sulfate-polyacrylamide gel electrophoresis
SGCG	Sarcoglycan gamma
SHBG	Sex hormone-binding globulin
SKA	Spindle and kinetochore-associated protein 1
SOC	Super optimal broth
SOS	sarcomere organization score
SOX2	SRY-box transcription factor 2
SRD5A1	5-Alpha reductase 1
SRD5A2	5-Alpha reductase 2
SRD5A3	5-Alpha reductase 3
STRA6	Stimulated by retinoic acid gene 6 protein
T	Testosterone
TAE	Tris-acetate-EDTA
TEMED	N,N,N',N'-Tetramethylethylenediamine
TMB	3,3',5,5'-Tetramethylbenzidine
UHPLC	Ultra-high-performance liquid chromatography
WB	Western blotting
WT	Wild-type
ZNF506	Zinc finger protein 506
ZNF558	Zinc finger protein 558
ZNF662	Zinc finger protein 662
ZNF69	Zinc finger protein 69
β-MHC	Beta-myosin heavy chain

3 Introduction

The anatomically distinct structures hypothalamus, pituitary gland and gonads form a functional endocrine unit, the so-called hypothalamic-pituitary-gonadal axis (HPG axis). The HPG axis regulates a number of body systems, including the reproductive organs and functions. One very important hormone, which is produced mainly in the testes and to a lesser extent in the ovaries and the adrenal glands under the control of the HPG axis, is testosterone (T). This steroid hormone is typically regarded as a classic “male” sex hormone. Testosterone is well studied in the reproductive organs and during the formation of prostate cancer, but its action in other organs is largely under-investigated and yet to be determined[1]. This work aims to investigate aspects of the action and function of T and its receptor, i.e. the androgen receptor, in primate heart muscle cells. Moreover, when triggered by the ligand-receptor system, what changes are induced in cardiomyocytes differentiated from induced pluripotent stem cells? This first chapter will introduce the study by first discussing the background, context, and research problems. The second section will outline the research aims, objectives, and questions.

3.1 Generation of testosterone and androgen metabolites

Androgens are sex steroid hormones produced by adrenal glands, testes, and ovaries in both men and women[2]. Their production involves a complicated pathway involving a variety of enzymes expressed not only in the tissues of synthesis but also in the peripheral organs[3] (Fig. 1). Like other steroid hormones, T is derived from cholesterol. Initially, a mitochondrial cytochrome P450 oxidase performs oxidative cleavage of cholesterol’s side chain. This results in the generation of pregnenolone, a molecule with six carbon atoms less than cholesterol. This molecule is then modified by steroid-17α-Hydroxylase, which removes another two carbon atoms yielding the production of various C19 steroids, including dehydroepiandrosterone (DHEA), one of the first androgen metabolites. The enzyme 3β-hydroxysteroid dehydrogenase additionally oxidizes the 3β-hydroxyl group producing androstenedione. Eventually, 17β-hydroxysteroid dehydrogenase reduces the C17 keto group of androstenedione and produces T. Another enzyme, 5α-reductase, catalyzes the reduction of the C4-5 double bond in the A ring of T, producing dihydrotestosterone (DHT), a more potent androgen compared with T[4].

A series of androgen conversions can also happen in the various peripheral tissues[5]. Dehydroepiandrosterone sulfate is generated from DHEA by sulfotransferase[6]. This metabolite is present in serum at the highest concentration compared with others reaching the µM range[7]. Androstenediol is produced from androstenedione by the same enzyme as T, however, by reduction of the C17 keto group[3]. This metabolite can be also aromatized to

17β-estradiol expanding the peripheral effects to input from estrogens[8]. Notably, androstenedione is an important prehormone that can be converted to T or estrone in the peripheral tissues of female bodies[9].

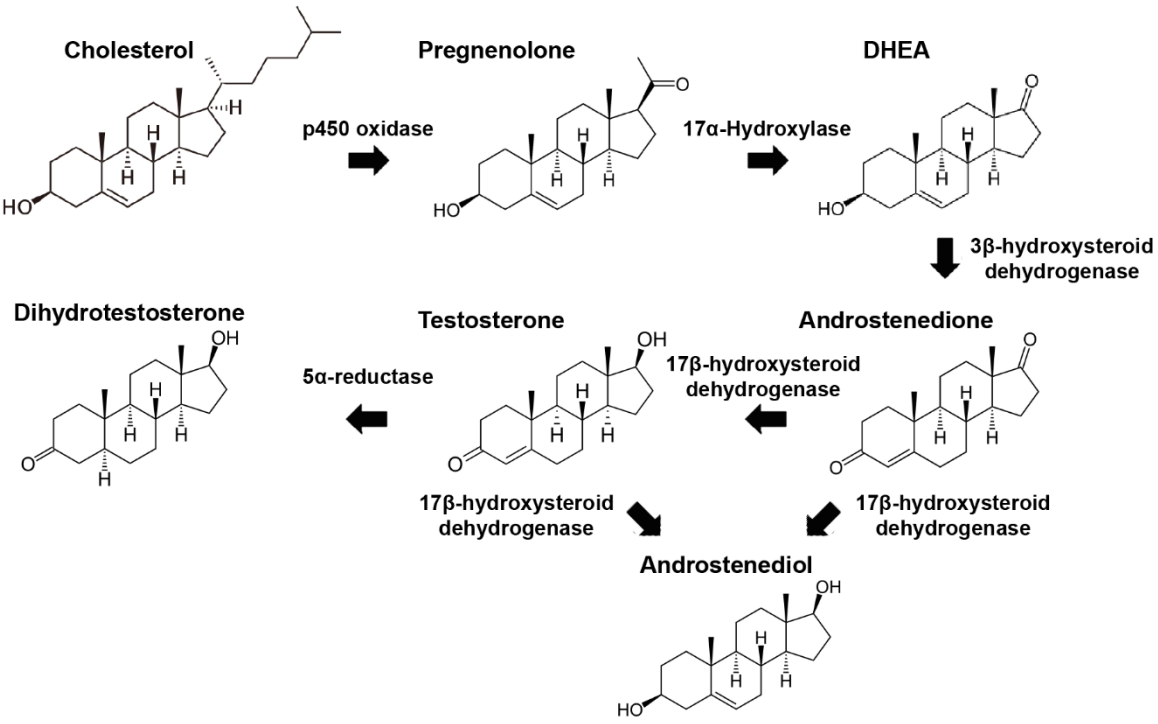

Figure 1. Overview of steroidogenesis with a focus on testosterone and dihydrotestosterone synthesis. DHEA stands for dehydroepiandrosterone.

All androgen metabolites, namely dehydroepiandrosterone sulfate, dehydroepiandrosterone, androstenedione, androstenediol, T, and DHT are released in the bloodstream[2]. These androgens circulate primarily bound to plasma proteins such as sex-hormone-binding globulin (SHBG), albumin, and rarely cortisol-binding globulins[10] (Fig. 2). Higher portions of T and DHT are transported via SHBG, while DHEA and androstenedione are transported by albumin[11]. A small portion of them present in a free unbound form is considered the bioavailable fraction[2].

Although SHBG binding restricts hormones from free transfer to various organs, this protein can bind to its respective SHBG receptor or be internalized inside the cells including heart muscle cells[12]. This process is facilitated by low-density lipoprotein-related protein 2 in rats and can trigger internal signaling responses in the cells. For example, SHBG internalization leads to increased levels of intracellular cAMP in fibroblast-like COS-1 cells[13]. Its expression is controlled by proliferator-activated receptor c (PPARc) and AMP-activated protein kinase that is activated by T in cardiac cells[14,15]. However, not much is known about local SHBG circulating levels and internalization and androgen uptake in cardiomyocytes.

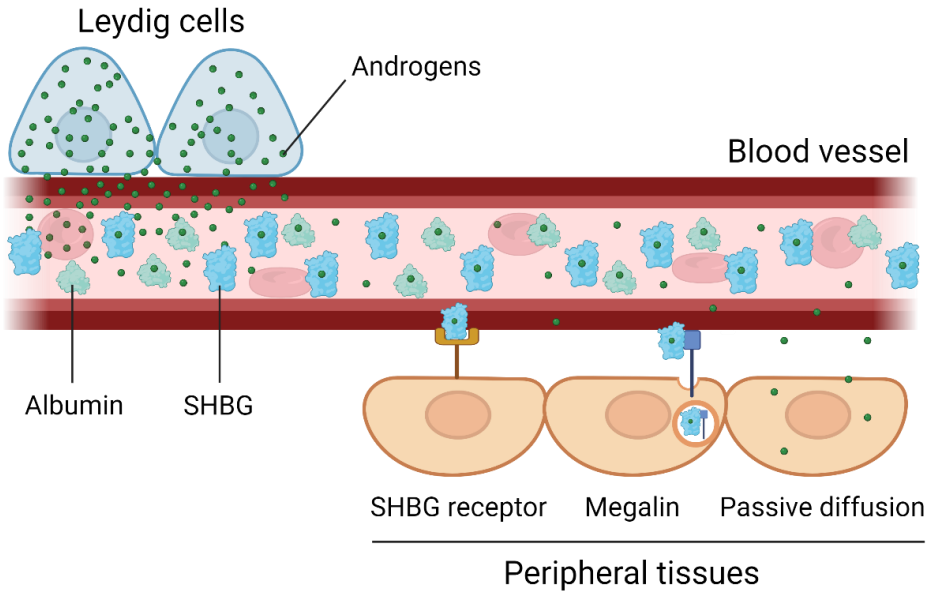

Figure 2. Proposed mechanism of androgen release to the bloodstream and uptake by peripheral tissues. Androgens are produced mainly by Leydig cells in the testis. The lipophilic nature of the androgens allows them to cross the plasma membrane and enter the blood vessels. From there androgens bind to sex-hormone-binding globulin (SHBG) tightly or weakly to albumins. A small portion of testosterone is left unbound and can freely cross the walls of blood vessels and be picked up by peripheral tissue by passive diffusion. Moreover, SHBG together with androgens can bind to SHBG receptor or be internalized by Megalin via the action of low-density lipoprotein-related protein 2. Created using Biorender.

Upon the delivery of the androgens to the peripheral tissues, they can diffuse through the membrane and bind to the androgen receptor (AR) or further undergo conversion to other metabolites[16]. Androstenedione and DHEA can bind to AR although with lower affinity compared with T and DHT[17,18].

In many androgen-responsive tissues T is further converted to DHT and mediates various intracellular events by 5α-reductase[19]. This enzyme is expressed in many human tissues of both sexes including the prostate, adipose tissue, mammary gland, and others. Not much is known about the presence of androgen-converting enzymes in the heart tissue. The data from the Human Protein Atlas[20] show no presence of sulfotransferase, steroid sulfatase, or steroid-17α-Hydroxylase in the heart. However, low levels of 3β-hydroxysteroid dehydrogenase and medium levels of 17β-hydroxysteroid dehydrogenase were detected in cardiomyocytes. Moreover, only 5α-reductase type 3 but not type 1 is present in human male and female hearts. The data for 5α-reductase type 2 are currently not available. This indicates that androgens can be metabolized by the human heart muscle cells.

In conclusion, androgens form a highly regulated complex network of action not only in central but also in peripheral tissues. A lot is known about androgen production and circulation in the bloodstream, but tissue-specific actions and responses, including the heart, are yet to be determined. Not only do different concentrations of each androgen influence the cells individually, but their heterogeneous response involves binding to AR or further local conversion to more or less active androgen metabolites. Additionally, not much is known about the uptake of other androgen metabolites by the heart compared with T. Moreover, SHBG internalization serves as an additional variable in androgen action. The investigation of various androgen metabolites' actions in the heart can expand our knowledge about their influence on cardiovascular physiology.

3.2 Androgen receptor action, post-translational modifications, and variants

Androgens are hydrophobic molecules that can enter the cell through the plasma membrane[21]. In the cytoplasm, T binds to the AR (also known as nuclear receptor subfamily 3, group C, member 4; NR3C4) or exhibits receptor-independent effects[16]. Moreover, T can be converted to other more or less potent androgens as described above. The effects that do not involve AR are, however, studied very poorly. The binding affinity of the receptor to the ligand corresponds to the physiological concentration of androgens. The levels of circulating steroids closely align with the concentrations needed for achieving half-maximal saturation of the receptor's binding site[22].

After the binding of T, two molecules of the AR form a dimer. This complex is then translocated from the cytoplasm into the nucleus[23]. There, the complex binds to the so-called androgen response element (ARE) that leads to activation or repression of gene transcription[24]. The consensus binding sequence of 5'-GGTACANNNTGTTCT-3' is composed of two incomplete 6-bp indirect repeats separated by a 3-pb spacer. The androgen receptor is composed of an N-terminal (transactivation) domain, DNA-binding domain, hinge region, and ligand-binding domain[23] (Fig. 3). The DNA-binding domain plays an essential role in binding to DNA / chromatin via two zinc fingers and C-terminal extension[25]. The P-box in the first zinc finger domain is responsible for DNA-receptor contacts[26].

The dimer further connects to tissue-specific pioneering factors that may vary significantly between the tissues[27]. These proteins make chromatin and cis elements open for receptor interaction. Genome-wide studies suggest that the AR primarily binds to accessible chromatin[28]. In the mouse prostate, FOXA1 plays a role as a pioneering factor, in the kidney HNF4A, in the epididymis AP-2α, and others[29].

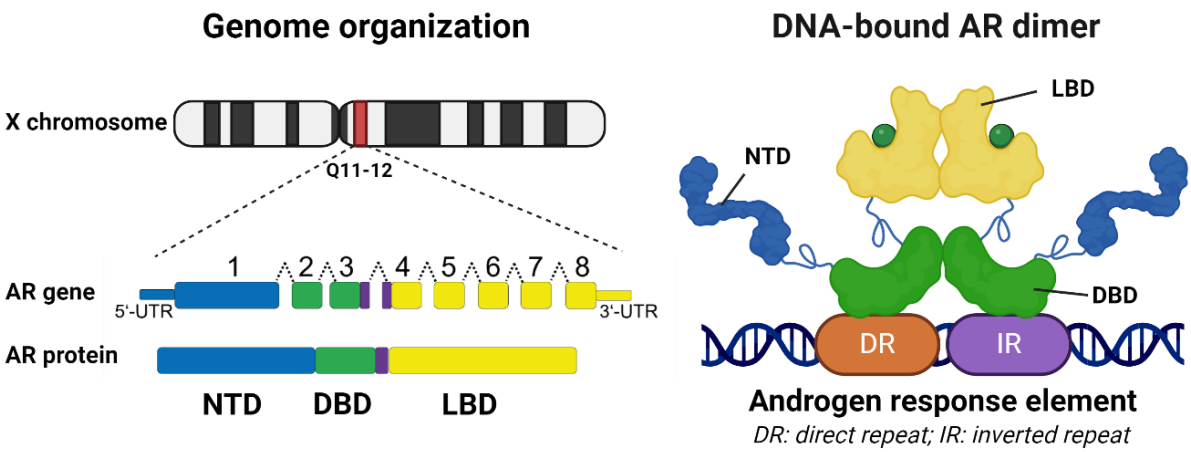

Figure 3. Genome organization and model of AR homodimer binding to androgen response element (ARE) in DNA. The AR gene is located on the long arm of the X chromosome Xq11–12. After the translation of all 8 exons, the protein consists of the N-terminal domain (NTD) depicted in blue, the DNA-binding domain (DBD) depicted in green, the hinge region depicted in purple, and the ligand-binding domain (LBD) depicted in yellow. After binding to androgens, the AR forms a homodimer and translocates to the nucleus where it binds to ARE via its DBD. Created using Biorender.

CHiP techniques detected AR occupation of various regulatory regions within the genome, but far from the proximal promoters[30] (Fig. 4). For example, 80-90% of AR binds primarily to non-promoter regions, particularly enhancer elements[31,32]. After binding of the receptor to chromatin, other coregulatory proteins can bind to facilitate precise action. Additional proteins, such as the Mediator complex, facilitate the looping of the enhancer region close to the promoter that allows regulation of gene expression[33]. Moreover, de-novo sequencing and enrichment analyses have shown the presence of cis-elements for several collaborating transcription factors within steroid binding sites[28,34]. Such interplay between local chromatin structure, collaborating transcription factors, and co-regulators allows receptor-selective and tissue-specific actions of AR in different tissues. However, since most of the research was done in cancer cell lines more data on the AR binding to ARE are needed in healthy tissues.

AR can undergo posttranslational modifications such as methylation (e.g. by EZH2), phosphorylation (e.g. by CDK1), acetylation (e.g. by p300), SUMOylation (e.g. by PIAS1), and ubiquitination (e.g. by SPOP)[35]. The functions of these modifications are versatile and impact protein stability, cellular localization, and transcriptional activity. For example, most AR phosphorylation sites in the N-terminal domain positively regulate its transcriptional activity, while others impact oppositely[35]. Not much is known about the degradation of AR

followed by protein ubiquitination. Most of these findings reflect the modification of AR in cancer cells and there remains a need to investigate AR modifications in healthy cells.

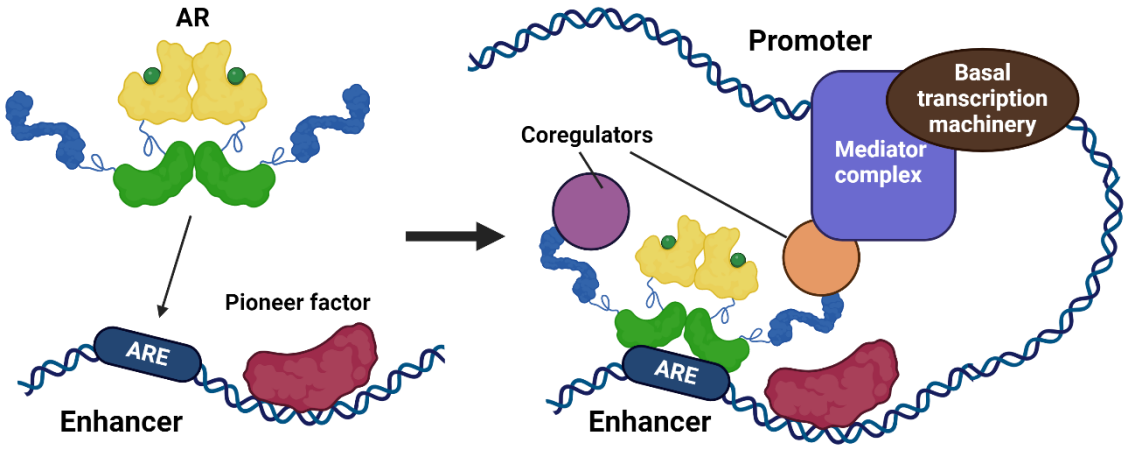

Figure 4. AR binding to open chromatin close to pioneer factors and further recruitment of gene expression protein machinery. AR homodimer binds to ARE in chromatin primed by pioneer factors. AREs are detected usually in enhancer regions of various genes. After AR binds to DNA, coregulatory proteins interact with NTD and recruit the proteins that influence chromatin organization and histones. These include the DNA looping by the Mediator complex essential for binding to basal transcription machinery in the promoter region. Created using Biorender.

AR is not only post-transcriptionally modified, but it also exists in several variants in different cell types[36]. The canonical isoform, known as AR-full length (AR-FL), is mostly studied based on the current literature. However, other important variants have been found both in cancer cells and in healthy tissues[37]. For example, AR-V7 is a truncated version of AR-FL lacking a ligand-binding domain making its action independent of binding to androgens[38]. This isoform and others may form homo- and heterodimers with each other and AR-FL and exhibit various functions[39]. Some studies addressed such interactions; however, they are limited to cancer cells and have not been described in healthy tissue.

3.3 Cardiovascular system overview

The cardiovascular system consists of the heart and blood vessels that connect all organs to transport nutrients, gases, hormones, and waste products. At the center lies a muscular organ, the heart, that creates the pressure for pumping blood ensuring its continuous flow to all organs[40]. This organ is composed of four chambers – two atria and two ventricles (Fig. 5). The atria contract to push the blood inside the ventricle. The right ventricle pumps deoxygenated blood to the lungs and the left ventricle pumps oxygenated blood that goes

to the aorta and spreads throughout the rest of the body. Specific valves mainly made of connective tissue ensure the unidirectional blood flow, while the conduction system maintains a rhythmic heartbeat[41]. The coronary arteries deliver nutrients and oxygen to the heart itself.

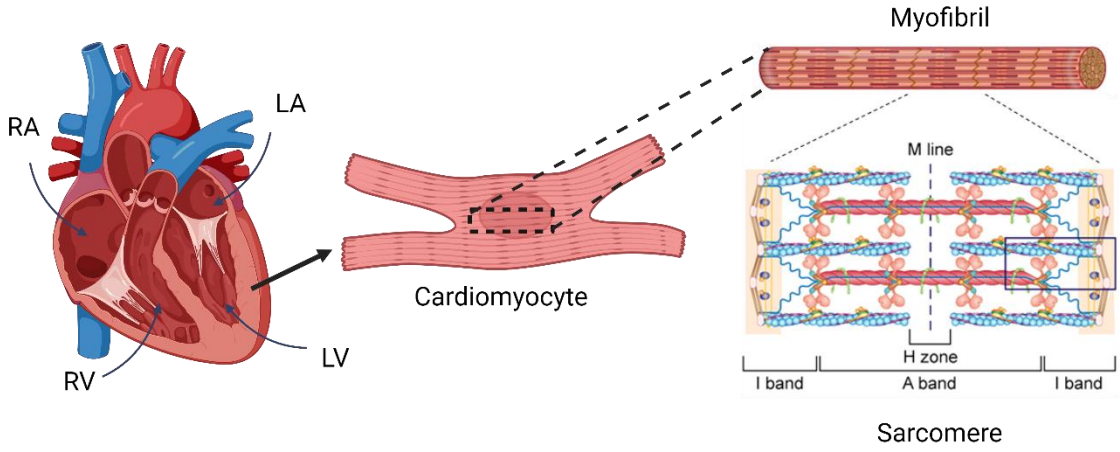

Figure 5. Hierarchical structure of the heart. It contains the main four chambers: right atrium (RA), right ventricle (RV), left atrium (LA), and left ventricle (LV). The myocardium is composed of heart muscle cells – cardiomyocytes. Each cell contains muscle fibers called myofibrils. These structures are formed by sarcomeres connected in series. Shortening and lengthening of sarcomeres leads to muscle contraction. Created using Biorender.

The heart consists of various cell types that play a specific role in maintaining the function of this organ[42]. The outer membrane encasing the heart is called the pericardium and consists of mesothelial cells that provide support and lubrication during heart contraction[43]. The myocardium, on the other hand, is responsible for pumping the blood by cardiomyocytes, heart muscle cells, and cardiac fibroblasts that create a supporting elastic structure[44]. Additionally, multiple big and small vessels made of endothelial cells, smooth muscle cells, and pericytes permeate the tissue[45]. The inner lining of the heart is comprised of connective tissue and endothelium forming a wall between the heart and the blood.

Cardiomyocytes are specialized muscle cells that are unique to the heart[46]. The organized arrangement of cytoskeletal proteins makes contraction possible[47]. Proteins like cardiac Troponin T, actin, myosin, Titin, α-actinin, and others form sarcomeres, contractile units of muscle cells. Actin and myosin filaments are the main components for muscle contraction that create a typical striated pattern visible in the cells under the microscope. While actin is connected to Z-disks at their ends, myosin filaments are anchored at the M-line for additional stabilization. Together, actin and myosin filaments overlap creating an H-zone where only myosin is present. Other proteins support such actin-myosin apparatus and anchor them to one another and the ends of sarcomeres. The sliding filament theory states

that upon Ca^{2+} release myosin heads form cross-bridges with actin, pulling them toward the center of the sarcomere[48]. Calcium binds to troponin T causing a conformational change, which then moves tropomyosin and opens the myosin-binding sites of actin. ATP hydrolysis leads to the further pulling of actin by myosin heads. This process results in the shortening of sarcomeres that altogether produce contraction of the muscle. Another ATP binds to the myosin heads, causing their detachment from actin and the muscle relaxes until the next intracellular Ca^{2+} wave. The morphological branching of cardiomyocytes allows them to transmit electrical signal propagation efficiently[49].

The proper arrangement of the sarcomere proteins is essential for synchronized contraction throughout the entire muscle. Understanding the formation of this machinery is still, however, limited. The influence of multiple effector molecules is currently studied in cardiomyocytes including their effect on sarcomere structure and organization.

3.4 Testosterone in cardiovascular diseases

The influence of T on the cardiovascular system and diseases has been intensely studied in the clinical literature with different and sometimes opposing outcomes[50]. Age-related declines in T levels are associated with an increased risk of heart disease[51]. Some studies have also associated low T levels with an increase in mortality[52]. However, higher levels of T have been found to correlate with other cardiovascular diseases[53,54]. Additionally, anabolic androgenic steroids (AAS) have been widely abused in sports and their effects showed unhealthy morphological and functional changes in the heart[55].

One study investigated free T, DHEAS, and insulin-like growth factor 1 levels in healthy men and men with chronic heart failure[56]. T deficiencies were found in young and old chronic heart failure patients, which also correlated with more severe chronic heart failure. Notably, deficiencies in other anabolic hormones have been associated with increased mortality, so they can be used as prognostic markers. Another study included men over 60 years old with chronic heart failure and reduced left ventricular ejection fraction, which reflects the proportion of blood ejected from the left ventricle with each contraction[57]. Low levels of T were associated with reduced left ventricular ejection fraction and N-terminal prohormone of brain natriuretic peptide. However, no significant link was detected between survival and T concentration in serum after adjusting for clinical variables.

Testosterone levels were also found to correlate with the length of hospitalization and readmission rates[58]. Patients with low T levels experienced more severe cardiac dysfunction and a higher likelihood of having heart-related issues due to reduced blood supply[59]. Left ventricular ejection fraction, the glomerular filtration rate of the kidney, and free T levels

were found to be predictors of mortality. Another study included patients diagnosed with heart failure who had reduced or preserved ejection fraction[60]. Lower DHEAS and T levels and higher SHBG levels were predictors of all-cause mortality risk.

Testosterone replacement therapy has been investigated for the possible beneficial systemic effect in T-deficient men diagnosed with HF[61]. On one hand, the data from meta-analyses of randomized trials showed that androgen replacement significantly improved electrocardiogram indicators[62,63]. However, no changes were detected in ejection fraction, systolic and diastolic blood pressure, and cardiac pro-inflammatory markers. On the other hand, another study of eight randomized controlled trials revealed no significant effect of physiological T-range supplementation on cardiac function and clinical outcome[64].

Arrhythmogenic Right Ventricular Cardiomyopathy (ARVC) is a genetic cardiomyopathy characterized by the replacement of the right ventricle myocardium with fibrous tissue and fat[65]. This leads to structural changes like myocardial thinning and dilation that cause cardiac dysfunction. Recent studies have found that 75% of the diagnosed patients are male, while only 25% are female[66]. Men with ARVC also exhibit a higher risk of ventricular arrhythmias in their lifetime. Male patients exhibited higher T levels with a specific cut-off that predicted further unfavorable outcomes[67]. Studies in cardiomyocytes generated from induced pluripotent cells of ARVC patients further showed 5 ng/mL T (17.3 nM) impact on elevating apoptosis and lipogenesis, key features of ARVC[67]. However, T did not change these parameters in healthy cells.

Many other data show the presence or absence of high T levels as a link to the outcome for other cardiovascular diseases such as dilated cardiomyopathy, myocarditis, hypertrophic cardiomyopathy, and others[68]. Both excess and lack of this androgen may lead to negative physiological outcomes. As described in this section, the present data are conflicting with each other. More importantly, some studies have shown no link between T and cardiac performance[68]. It is further not well studied whether T levels may directly cause the development of cardiac dysfunction.

3.5 The effects of androgens on heart muscle cells

The androgen receptor was found in cardiomyocytes of rats, mice, and primates[69–72]. Several studies have shown the impact of supraphysiologic (100 nM) T concentration on cardiac electrophysiology, gene expression, and signaling pathways[73–80] (Fig. 6) Cultured rat cardiomyocytes and hearts obtained from adult male orchiectomized (ORX) rats have shown that T supplementation leads to the rapid phosphorylation (Thr286) of Ca^{2+}-calmodulin kinase II (CaMKII) and the phospholamban[73]. These proteins play a significant

role in the regulation of muscle contraction[81]. CamKII activation also has been shown to activate myocyte enhancer factor-2 (MEF2) expression possibly through HDAC4/5 histone deacetylase[82]. Eventually, the enlarged hearts of T-treated ORX rats showed an increase not only in phosphorylation levels of CaMKII and phospholamban but also in AR and MEF2 protein levels[73]. This shows the activation of MEF2, a transcription factor in cardiomyocytes, through AR and CaMKII signaling. Furthermore, left ventricle/body weight ratio, left ventricle/tibia length ratio, myosin heavy chain β (β-MHC), and SKA protein levels increased in the T-treated ORX rats compared with non-treated ORX and control rats. Beta-MHC and SKA have been used as markers for cardiac hypertrophy, an increase of the myocardium volume via cell enlargement.

T also contributes to the development of cardiac hypertrophy via another signaling pathway. Phosphorylation of the mammalian target of rapamycin complex 1 (mTORC1) is induced by T in cultured neonatal rat cardiomyocytes[77]. Moreover, its downstream targets like ribosomal protein S6 kinase beta-1 (S6K1) and initiation factor 4E-binding protein 1 (4E-BP1) have been also phosphorylated. Activation of these two proteins is essential for the induction of cardiac hypertrophy *in vivo*[83]. Rapamycin and siRNA to mTOR have blocked the phosphorylation of S6K1 in T-treated cardiomyocytes[77]. Additionally, inhibition of ERK1/2, but not Akt, blocked S6K1 phosphorylation initiated by T induction. This means that the MEK/ERK1/2 pathway, but not PI3K/Akt, is needed to activate the mTORC1 pathway with subsequent phosphorylation of S6K1 to induce cardiac hypertrophy.

Glucose uptake and glycolysis are induced in T-treated hypertrophied cardiomyocytes by measuring extracellular acidification rate and fluorescent glucose analog 2-NBDG[76]. Additionally, hypertrophic markers like cell size and β-MHC levels were increased in 100 nM T-treated cardiomyocytes. T treatment elevated Hexokinase 2 mRNA levels in cardiomyocytes. This impact was further abolished by GLUT4 and AR inhibitors indinavir and bicalutamide, respectively. The authors also showed the requirement of AMP-activated protein kinase, AMPK, for T-induced cardiac hypertrophy. Several studies have investigated the androgen action independent of its receptor using AR inhibitors and knock-out approaches[78,84,85]. This non-genomic action is studied within the time frame of seconds or minutes in AR knock-out models. Upon entry to the membrane, 100 nM T impacts calcium homeostasis in the absence of AR[78]. A rapid T exposure of up to 7 min increases intracellular [Ca^{2+}] in cultured rat cardiomyocytes measured by high-affinity Ca^{2+} dye fluo3-AM. The absence of AR in the perinuclear zone was confirmed with immunocytochemical analysis[78]. Inhibitors of phospholipase C and inositol 1,4,5-trisphosphate receptor, but not AR, abolished the Ca^{2+} signal. This means that intracellular storages are involved in [Ca^{2+}] increase of T-treated cardiomyocytes via receptor-independent action. Notably, pertussis

toxin and an inhibitor of βγ-subunits of G protein abolished Ca^{2+} elevation confirming the membrane-bound action of T.

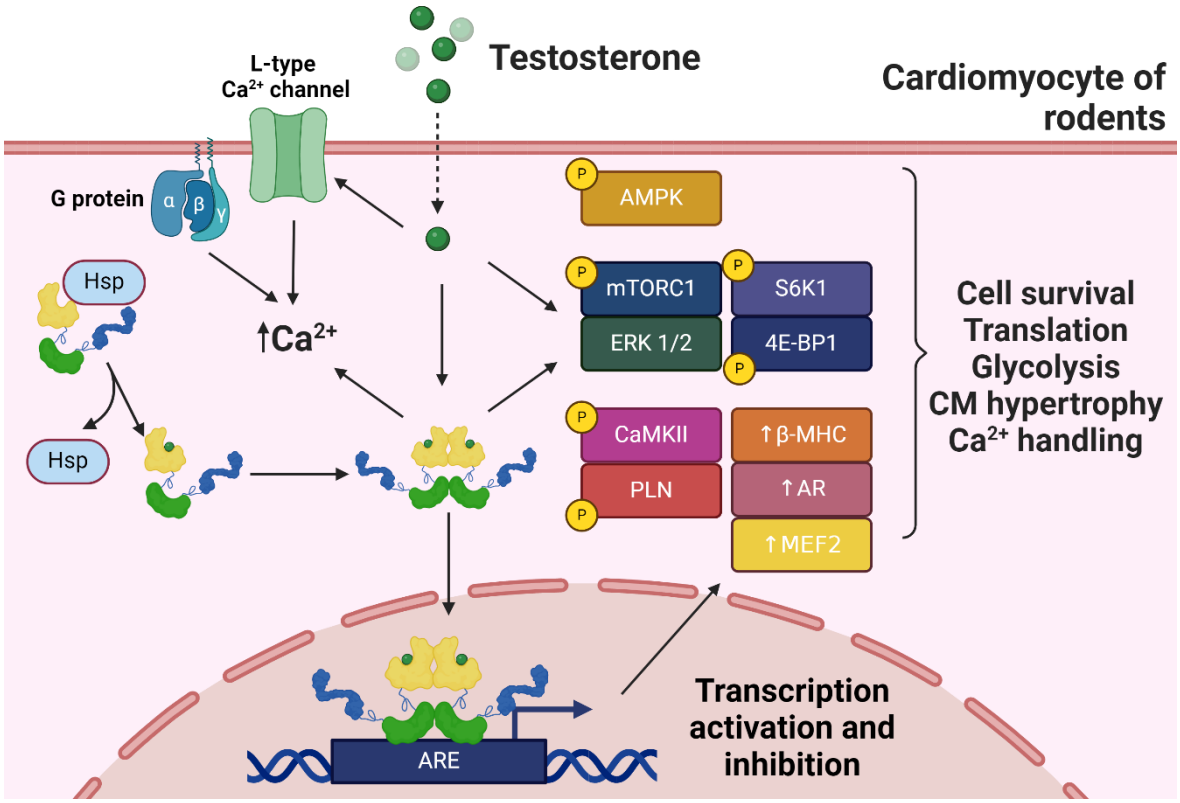

Figure 6. Proposed mechanism androgen action (in)dependent of AR presence in CMs of rodents. Testosterone or other types of androgens are capable of crossing the plasma membrane and binding to AR. Heat shock proteins (Hsp) release AR that further forms dimers and binds to ARE to activate or inhibit gene expression. Studies have shown the phosphorylation and increased quantities of different proteins in rats and mice with or without AR action using androgen antagonists. The changes in proteome impact cell survival, translation, glycolysis, and Ca^{2+} handling - all the processes involved in cardiac development and hypertrophy. AMP-activated protein kinase (AMPK), mammalian target of rapamycin complex 1 (mTORC1), Ribosomal protein S6 kinase beta-1 (S6K1), Extracellular signal-regulated kinase 1/2 (ERK1/2), 4E-binding protein 1 (4E-BP1), Ca^{2+}-calmodulin kinase II (CaMKII), phospholamban (PLN), myosin heavy chain β (β-MHC), myocyte enhancer factor-2 (MEF2). Created using Biorender.

Another study has investigated short and long incubation of cardiomyocytes with T[85]. 24-30 h pretreatment with 100 nM T led to an increase in whole-cell L-type Ca^{2+} channel current, which was caused by elevated expression levels of alpha 1C subunit of L-type Ca2+ channel and single-channel activity. Such pretreatment also resulted in increased Ca^{2+} sparks and improved myocyte contractility with no alteration of sarcoplasmic reticulum Ca^{2+}

load. All effects mentioned were abolished in the group that was additionally treated with flutamide, an AR inhibitor. On the other hand, cardiomyocytes were also exposed in the minutes-range in whole-cell configuration and consecutively superfused with the control solution and 1, 10, and 100 nM T. Such treatment resulted in opposite effects compared with 24-hour treatment. Short-term T exposure decreased the frequency of Ca^{2+} sparks, inhibited the L-type Ca^{2+} channel, and suppressed the contractility of cardiomyocytes. Authors suggested that T might act through the lipid phase of the membrane close to L-type Ca^{2+} channels.

Only one study has shown the generation of AR KO and further exposure of cardiomyocytes to T in comparison to the control group with AR present[84]. The authors focused on the investigation of left atria (LA) electrophysiology and arrhythmogenesis. Adult male AR KO mice had larger LA diameter and reduced LA fractional shortening, the change in diameter during active contraction. Additionally, AR KO cardiomyocytes exhibited lower negative resting membrane potential and a bigger 90% action potential duration than wild-type group. Isoproterenol, a beta-adrenergic receptor agonist, hypocalcemic solutions, and Ouabain, an inhibitor of Na/K-ATPase, increased the amplitude of delayed afterdepolarizations in AR KO, but not WT LA. AR KO LA expressed more of CaMKII, Na^{2+}/Ca^{2+} exchanger, phosphorylated phospholamban, and fewer ion channel subunits Cav1.1 Kir2.1, Kir3.1 compared with wild-type LA. These findings point to a shift in atrial electrophysiology toward arrhythmogenesis by AR KO.

All studies described above show the influence of T in cardiomyocytes of rats and mice. However, only one study addressed the impact of androgens in human heart muscle cells[86]. Treatment of isolated cardiomyocytes with 100 nM DHT for 24-30 h increased whole-cell L-type Ca^{2+} current density with no shift in the current-voltage relation. This was further supported by the increased expression of the Cav1.2 subunit of L-type calcium channels in DHT-treated cardiomyocytes. Authors claim that these data may explain the supraphysiological effects of androgens on the cardiovascular system.

To date, no study investigated the effects of physiological concentrations (25-35 nM) of T in human ventricular cardiomyocytes. Additionally, rodent models provide information on AR-dependent and independent mechanisms using a higher T concentration than found in the serum. Although widely used in research, humans and rodents differ in physiological and genetic parameters[87–89]. Therefore, other models are needed for further research in cardiovascular biology.

3.6 Use of induced pluripotent stem cells and cardiac differentiation *in vitro*

Induced Pluripotent Stem Cells (iPSCs) are generated by reprogramming adult somatic cells to pluripotency[90] (Fig. 7). This is achieved by the introduction of transcription factors like OCT4A, SOX2, KLF4, c-Myc, and LIN28A[91]. These pluripotency factors guide the cellular fate towards embryonic developmental potential and self-renewal, conferring the ability to cells to differentiate into all cell types of interest.

iPSCs represent an alternative to animal experiments in such directions as drug toxicity tests, disease modeling, and regenerative therapies[92]. This is particularly important for the field of cardiovascular diseases due to the limited regenerative potential of the heart[93]. Once the cardiac tissue is damaged, e.g. after myocardial infarction, mostly fibrotic tissue is formed at the repair site[94]. This can further lead to the reduction of cardiac function[95]. In severe cases, transplantation is required to save the lives of the patients[96]. This however may trigger an immune response with rejection of transplant. The ability to derive cardiomyocytes from iPSCs in a controlled manner enables the generation of patient-specific cells. Such cardiac tissues may further reduce the risk of rejection by the immune system or be used for studying various diseases found in patients with genetic mutations[97].

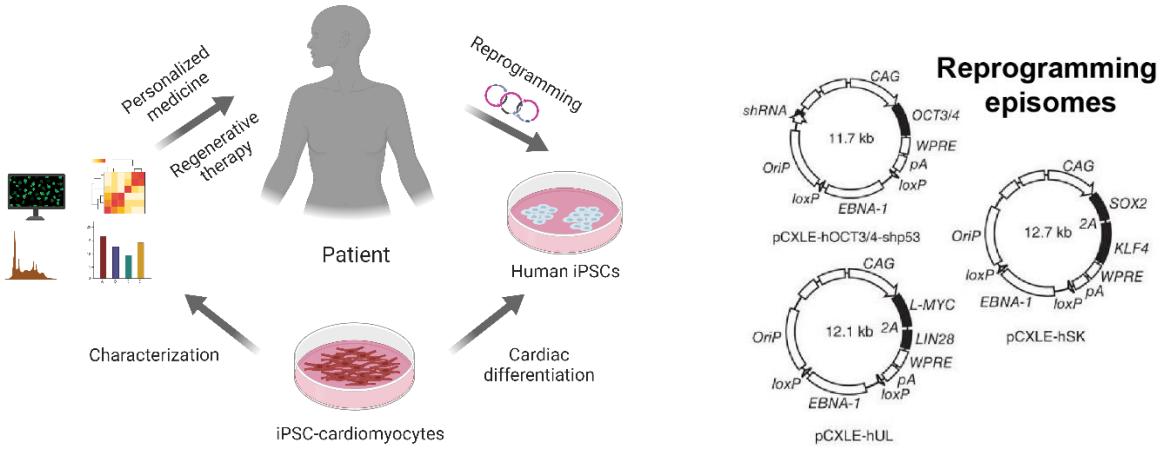

Figure 7. Generation of iPSC as a tool for a personalized approach in medicine. Schematic overview of iPSC generation and its use for differentiation to heart muscle cells with the following characterization done for personalized medicine and regenerative therapy. Non-integrative episomes developed by Okita et al.[98] depicted on the right contain pluripotency factors for reprogramming of somatic cells to iPSCs. Created using Biorender.

While physiological parameters can be widely studied in the actual heart, invasive studies of molecular and cellular processes are usually not possible for ethical reasons. Here, iPSC-derived cardiomyocytes (iPSC-CMs) can be an excellent substitute. Researchers can also

mimic human cardiac development using this *in vitro* model[99]. The promising iPSCs tool has, however, its challenges. To date, certain limitations have been found in the generation of iPSC-CMs. The most important one addresses the issue of not fully recapitulating the complexity of the adult human heart[100]. The adult cardiomyocytes are considered mature, while iPSC-CMs are immature based on various factors. The structure and morphology of lab-grown cardiomyocytes resemble the ones found in the fetus[100]. iPSC-derived cells are roundish and more multiangular compared to the elongated, “brick-like” shape of adult cardiomyocytes. This is further reflected by the sarcomere length and structure, which is shorter and more disorganized in iPSC-CMs[100]. The lack of t-tubules, structures essential for proper excitation, reduces the contraction rates[101]. Calcium handling, needed for sarcomere shortening, is less efficient in iPSC-CMs[100]. An important switch from a highly proliferative state (hyperplasia) to size enlargement of the cells (hypertrophy) happens in the early postnatal period and is not always visible in iPSC-based cultures[102]. All this is further supported by different gene expression profiles compared to those found in adult cardiomyocytes[103]. Additionally, differentiation to cardiomyocytes leads to high heterogeneity in terms of subtype specification and further challenges in reproducing experiments[104]. Researchers are working to optimize differentiation protocols in order to yield a higher proportion of cardiomyocytes[99].

Despite the limitations, iPSCs provide an excellent tool for studying the development and physiology of cardiomyocytes. Specific differentiation protocols have been developed to generate ventricular and atrial cardiomyocytes[99]. iPSC technology has opened new possibilities for exploring the effects of different biological molecules, including hormones. Dexamethasone, a synthetic analog of glucocorticosteroids, and triiodothyronine's influence on cardiac tissue have been investigated using iPSCs[105,106]. Only one study described above addressed the influence of T on human iPSC-CMs with a focus on the ARVC model[67].

3.7 Non-human primate models

Given the complexity of cardiovascular diseases, a proper choice of animal models is required for preclinical testing. As described above, rodents have been used in most studies about T effects on cardiac tissues. These models have been extensively used in basic research, although they fail to recapitulate certain physiological and pathological parameters in humans[87,88]. Large domestic animals like dogs, goats, sheep, and pigs are also used for research, although to a lesser extent[107]. This is further complicated by a lack of information, higher maintenance costs and ethical concerns due to limited research in these species.

Another model – non-human primates (NHP) – has been used for decades in preclinical studies[108]. Genetic Phylogenetic proximity to *Homo sapiens* makes the NHP the closest model for humans. Similar physiology, anatomy, immunology, and developmental programming suggests higher levels of research translatability from these models[109]. Compared with polytocous animals, primates share a similar hypothalamic-pituitary-adrenal axis important for T production[110]. Human and NHP brains are especially similar in the hippocampus structure, cortical development, and organization[111]. NHPs naturally develop many cardiovascular diseases and are widely studied in that area[108]. Rhesus monkeys develop atherosclerosis, and the appearing lesions resemble the ones in humans[112]. Cardiovascular diseases are accompanied by complex clinical phenotypes, which makes an even more restricted range of choices from available models.

While the main focus lies on the generation of human iPSCs, a slower pace of the development of the iPSC technology is encountered in the NHP models[113]. Relevant progress was made in the generation of NHP embryonic pluripotent stem cells (ESCs) by different approaches. Multiple ESC lines are available from rhesus macaque, marmoset, cynomolgus monkey, and baboon[113]. However, this approach involves embryo destruction thereby raising ethical concerns[114]. Multiple NHP iPSC lines have been generated in our lab in recent years, including rhesus macaque, marmoset, baboon, and cynomolgus monkey[115]. For that, we used NHP skin fibroblasts, a more gentle, less laborious, and ethical approach compared to the use of embryos. These cells were further used to generate a cardiac differentiation protocol for the available NHP iPSCs, which allows for direct translatability[115].

3.8 Aims of this thesis

Cardiac differentiation of human and NHP iPSCs offers a unique platform to investigate the impact of T on the cellular and molecular level. Notably, rhesus macaque and humans share the same serum T levels of around 7-10 ng/mL (25-35 nM) in males[116,117]. Although widely studied in rodents, T has been used mostly in supraphysiological concentrations. Despite numerous studies described above, only presence but not localization of AR has been investigated in the cardiomyocytes. This creates a research gap studied in this project about the T impact and localization of AR in T-treated and non-treated human cardiomyocytes. Additionally, due to the unavailability of human tissue, we used rhesus macaque heart tissues as the *in vivo* counterpart of iPSC-CMs and tested similarities of T and AR action between rhesus and human iPSC-CMs.

The scientific objectives of this thesis included:

1) Fine-tuning of a cardiac differentiation protocol of human and rhesus macaque iPSCs.
2) Detection of AR in male and female rhesus macaque healthy adult heart tissues.
3) Localization of AR in iPSCs and iPSC- CMs.
4) Investigation of physiological (25 nM) and supraphysiological (100 nM) T effects on male human and rhesus iPSC-CMs.
5) Generation of a human AR KO iPSC line, its differentiation to cardiomyocytes, and comparison of T effects on cellular parameters of cardiomyocytes with and without AR.
6) Investigation of androgen metabolites in the media of iPSC-CMs treated and non-treated with T.

This work builds a foundation for future understanding and investigation of T and AR action in primate cardiomyocytes.

4 Material and Methods

4.1 Materials

4.1.1 Cell lines

Table 1. Cell lines of human and rhesus macaque origin.

Cell line	Name	Species	Sex	Origin	Tissue	Plasmid Integration
hiPSC1	iLonza2.2	*Homo sapiens*	Male	DPZ	Foreskin fibroblasts (purchased from Lonza)	No
hiPSC2	iLonza2.4	*Homo sapiens*	Female	DPZ	Foreskin fibroblasts (purchased from Lonza)	No
RhiPSC1	iRh33.1	*Macaca mulatta*	Male	DPZ	Skin fibroblasts	Yes
RhiPSC2	iRh24.4	*Macaca mulatta*	Female	DPZ	Skin fibroblasts	No
22RV1	22RV1	*Homo sapiens*	Male	DSMZ	Prostate carcinoma	No

4.1.2 Tissue samples

Table 2. Tissue samples of rhesus macaque.

Species	Number	Sex	Origin	Tissue
Macaca mulatta	2245 (1)	Male	DPZ	Heart
Macaca mulatta	2519 (2)	Male	DPZ	Heart
Macaca mulatta	16100 (3)	Male	DPZ	Heart
Macaca mulatta	16120 (4)	Male	DPZ	Testis
Macaca mulatta	2447	Male	DPZ	Liver
Macaca mulatta	15292	Male	DPZ	Testis
Macaca mulatta	2375 (1)	Female	DPZ	Heart
Macaca mulatta	2243 (2)	Female	DPZ	Heart
Macaca mulatta	2718 (3)	Female	DPZ	Heart
Macaca mulatta	2544 (4)	Female	DPZ	Heart
Macaca mulatta	2602 (5)	Female	DPZ	Heart

Macaca mulatta	0026	Male	DPZ	Left ventricle, heart
Macaca mulatta	2488	Male	DPZ	Left ventricle, heart
Macaca mulatta	2486	Male	DPZ	Left ventricle, heart
Macaca mulatta	16166	Female	DPZ	Left ventricle, heart
Macaca mulatta	2975	Female	DPZ	Left ventricle, heart
Macaca mulatta	2980	Female	DPZ	Left ventricle, heart
Macaca mulatta	2509	Female	DPZ	Left ventricle, heart

4.1.3 Cell culture medium and supplements

Table 3. Cell culture medium and supplements.

Component	Supplier
Activin-A ^{H2O}	R&D Systems, 338-AC
Albumin Human*	Sigma-Aldrich, #A9731
B-27™ supplement (50x), serum-free	Thermo Fisher Scientific, 17504044
B-27™ supplement, minus insulin	Thermo Fisher Scientific, A1895601
Bone morphogenetic protein 4 (BMP4) ^{BSA}	PeproTech, #120-05
Bovine albumin fraction V solution (BSA, 7.5 %)	Thermo Fisher Scientific, #15260037
Chir99021 ^{DMSO}	Stemgent, 04-0004
Dulbecco's modified Eagle medium, GlutaMAX™ (DMEM)	Thermo Fisher Scientific, 31966021
DMSO	Sigma-Aldrich, #D2650
DPBS	Thermo Fisher Scientific, 14190144
Fetal bovine serum	Thermo Fisher Scientific, 16140071
Geltrex™	Thermo Fisher Scientific, A1413202
L-Glutamine (200 mM)	Thermo Fisher Scientific, 25030081
HEPES	Roth, HN78.1
IWR-1 ^{DMSO}	Sigma-Aldrich, I0161
L-Ascorbic acid 2-phosphate (L-AA) ^{H2O}	Sigma-Aldrich, A8960
Lactate	Sigma-Aldrich, L4263
Penicillin-Streptomycin (P/S)	Thermo Fisher Scientific, 15140122
Roswell Park Memorial Institute medium (RPMI 1640)	Thermo Fisher Scientific, 11875093
RPMI 1640 medium, no glucose	Thermo Fisher Scientific, 11879020
Pro-survival compound ^{DMSO}	Merck Millipore, 529659

StemMACS™ IPS-Brew XF	Miltenyi Biotec, 130-104-368
StemPro Accutase®	Thermo Fisher Scientific, A1110501
Sodium pyruvate (100mM)	Thermo Fisher Scientific, 11360070
Testosterone (final DMSO c <0.01%)	Sigma, #T1500
TrypLE™ Express Enzyme (1X)	Gibco, 12604013
Versene 1:5000 (1X)	Gibco, 15040-033

* dissolved in media; ^{DMSO} dissolved in DMSO; ^{H_2O} dissolved in ddH_2O; ^{BSA} dissolved in PBS/BSA. All chemical solutions used for cell culture were sterile-filtered.

4.1.4 Antibodies

Table 4. Primary antibodies used in FACS, immunofluorescence imaging and Western Blot analysis.

Method	Antigen	Type	Dilution	Supplier
FACS	Cardiac troponin T (cTNT), FITC-conjugated	Clone REA400	1:50	Miltenyi Biotec, #130-119-575
FACS	Cardiac troponin T (cTNT), APC-conjugated	Clone REA400	1:50	Miltenyi Biotec, #130-120-403
FACS	IgG Control REA400	Clone REA400	1:50	Miltenyi Biotec, #130-119-575
IF/WB/ IHC	Androgen Receptor	polyclonal rabbit IgG	1:200	Cell signaling, #5153
IF	Aromatase	Monoclonal rabbit IgG	1:500	Cell signaling, # 14528S
IF	Cardiac troponin T	monoclonal mouse IgG	1:200	Thermo Fisher Scientific, MA5-12960
IF	Connexin43	polyclonal rabbit IgG	1:1000	Abcam, #ab11370
IF/WB	LIN28A	polyclonal rabbit IgG	1:800	Cell signaling, #3978S
IF/IHC	Mouse IgG isotype control	Polyclonal mouse IgG	variable*	Antibodies online, ABIN930032
IF/IHC	Rabbit IgG isotype control	polyclonal rabbit IgG	variable*	Antibodies online, ABIN376827

IF	Myosin light chain 2a	monoclonal mouse IgG	1:200	Synaptic systems, 311 011
IF	Myosin light chain 2v	polyclonal rabbit IgG	1:200	Proteintech, #10906-1-AP
IF/WB	NANOG	monoclonal rabbit IgG	1:400	Cell signaling, #4903
IF/WB	OCT4A	polyclonal rabbit IgG	1:400	Abcam, #ab19857
IF/WB	SALL4	Polyclonal rabbit IgG	1:400	Sigma, HPA015791
IF/WB/ IHC	SRD5A2	Monoclonal rabbit IgG	1:200	Thermo Fisher Scientific, MA537985
IF/IHC	SRD5A3	Polyclonal rabbit IgG	1:400	Sigma, HPA027006
IF	α-actinin	mouse IgG	1:1000	Sigma-Aldrich, #A7811
WB	α-tubulin	monoclonal mouse IgG	1:2000	Sigma, T9026

Antibodies were diluted in 1% BSA/DPBS or 0.1% Triton X-100 /BSA (DPBS according to the method. FACS - Fluorescence-activated cell sorting, IF – Immunofluorescence staining, WB – Western blot analysis. *IgG antibodies were used with various concentrations respective to the working dilution of each primary antibody.

Table 5. Secondary antibodies used in immunofluorescence imaging.

Method	Antigen	Type	Dilution	Supplier
IF	Alexa 488 conjugated	donkey-α-rabbit IgG	1:500	Thermo Fisher Scientific, A21206
IF	Alexa 488 conjugated	goat-α-mouse IgG	1:500	Thermo Fisher Scientific, A28175
IF	Alexa 555 conjugated	donkey-α-rabbit IgG	1:500	Thermo Fisher Scientific, A31572
IF	Alexa 555 conjugated	goat-α-mouse IgG	1:500	Thermo Fisher Scientific, A21422

IF – Immunofluorescence staining

4.1.5 Molecular biology kits, chemicals, and solutions

Table 6. Molecular biology kits.

Kit	Supplier
DNeasy® Blood and Tissue Kit	Qiagen, 69504
EdU Click-555 Roti® Imaging kit	Roth, 1Y72.1
EnVision FLEX Mini Kit, High pH	Agilent, K802321-2
EnVision FLEX Mini Kit, High pH	Agilent, K802321-2
GeneJet Plasmid Miniprep Kit	Thermo Fisher Scientific, K0502
Lipofectamine 3000	Thermo Fisher Scientific, L3000001
NucleoSpin® Gel and PCR Clean-up	MACHERY-NAGEL, 740609.250
Omniscript RT Kit (200)	QIAGEN, 205113
Pierce™ BCA Protein Assay Kit	Thermo Fisher Scientific, 23227
Pierce™ ECL Western Blotting Substrate	Thermo Fisher Scientific, 32209
Plasmid Maxi Kit (25)	QIAGEN, 12163
ReliaPrep™ RNA Miniprep Systems	Promega, Z611

Table 7. Chemicals and solutions.

Substance	Supplier
17ß-estradiol-6-CMO-BSA	Arbor Assay, C266-6ML
17ß-estradiol-HRP	Arbor Assay, C267-6ML
Acetic acid	Roth, 3738.1
Acetonitrile	Th. Geyer, 2697
Acrylamide solution	Sigma-Aldrich, A4058
Agarose	Biozym LE, 840004
Ammonium acetate	Merck, 631-61-8
Ampicillin	Roth, K029.2
BbsI-HF®	NEB, R3539S
Bromophenol Blue	Sigma-Aldrich, B8026
$CaCl_2$	Sigma-Aldrich, 21114
CsCl	Sigma-Aldrich, 289329
CsOH	Sigma-Aldrich, 232068
D3-testosterone-glucuronide (D3-T-gluc)	NMI
DAPI (4′, 6-diamidino-2-phenylindoledihydrochloride)	Sigma-Aldrich, #D9542
Dithiothreitol	Thermo Fisher Scientific, R0861
DNase/RNase-Free Distilled Water	Qiagen, 129114

EDTA	Roth, 8043.2
EGTA	Roth, 3054.3
Ethanol	Roth, 1HPH.1
Ethidium bromide (10 mg/ml)	Roth, 2218
Fluoromount-G™	Thermo Fisher Scientific, #00-4958-02
Formaldehyde solution, 35%	Roth, 4980.2
Gel Loading Dye, Purple (6X)	New England BioLabs, #B7024S
GeneRuler 1 kb DNA Ladder	Thermo Fisher Scientific, #SM0331
Glucose	Sigma-Aldrich, G8270
Glycergel Mounting Medium, Aqueous	Agilent, C056330-2
Glycerine	Sigma-Aldrich, G5516
Glycine	Roth, 3790
Halt™ Protease Inhibitor Cocktail (100X)	Thermo Fisher Scientific, 78442
HEPES	Thermo Fisher Scientific, 15630056
Human Adult Normal Tissue: Heart: Ventricle (left), RNA	Biocat, R1234138-50-BC
K_2CO_3	Roth, P743.2
KH_2PO_4	KMF
LB agar	Sigma-Aldrich, L2897
LB broth	Sigma-Aldrich, L3022
Methanol	Roth, T909.1
Meyer’s Hemalaun solution	Merck, 1.092.490.500
Mg-ATP	Sigma-Aldrich, A9187
$MgCl_2$	Sigma-Aldrich, 63020
Na_2HPO_4	Serva, 13472-35-0
NaCl	Roth, 3957.2
$NaHCO_3$	KMF
Omniscript RT Kit (200)	QIAGEN, 205113
Paraffin (Paraplast)	Roth, X880.1
Paraformaldehyde (PFA)	Merck Millipore, #104005
Picric acid	Pan Reac Applichem, A2520,25000
RNase-free water	Qiagen, 129112
RIPA lysis buffer	Thermo Fisher Scientific, 89901
Rotiphorese® 50x TAE Puffer	Roth, #CL86
Sodium dodecyl sulfate	Sigma-Aldrich, L3771
Spectra™ Multicolor Broad Range Protein Ladder	Thermo Fisher Scientific, 26634

SYBR™ Green PCR Master Mix	Thermo Fisher Scientific, 4309155
T4 PNK	NEB, M0201
T4 DNA ligase	NEB, M0202
Taq DNA Polymerase	NEB, M0273S
t-Butylmethylether (MBTE)	Sigma-Aldrich, 5.89595
TEA-Cl	Sigma-Aldrich, 86614
TEMED	Thermo Fisher Scientific, 17919
Testosterone-3-CMO-BSA	Clinical Endocrinology Laboratory, UC Davis, USA, R156/7
TMB X-tra (& prestained)	Kementec, 4800
Transfer membrane Immobilon®-P	Roth, T831.1
tri-Sodium citrate Dehydrate	Roth, 4088.3
Tris	Roth, 2449.2
Triton™ X-100	MP Biomedicals, #02300221
Tween 20	Sigma-Aldrich, P9416
Xylol	Roth, 9713.1
β-glucuronidase	Roche, BGALS-RO

4.1.6 Oligonucleotides

Table 8. Oligonucleotides used for PCR and sgRNA for CRISPR/Cas9 system.

Oligonucleotide	Sequence 5'-3'	Amplicon length, bp	Annealing temperature	Species
AR, forward	AGCCAGTGTGTCCGAATGAG	112	60°C	*Homo sapiens, Macaca mulatta*
AR, reverse	CCACTGGAATAATGCTGAAGAGT	112	60°C	*Homo sapiens, Macaca mulatta*
AR-V7, forward	GAGATGAAGCTTCTGGGTGTC	205	52°C	*Homo sapiens*
AR-V7, reverse	CGGAATTTTTCTCCCAGAGTCATC	205	52°C	*Homo sapiens*
CYP19A1, forward	ATGCGAGTCTGGATCTCTGG	964	57.3°C	*Homo sapiens, Macaca mulatta*
CYP19A1, reverse	ACTCGAGTCTGTGCATCCTT	964	57.3°C	*Homo sapiens, Macaca mulatta*

GAPDH_1, forward	GGTCACCAGGGCTGCTTTTA	82	60°C	*Homo sapiens, Macaca mulatta*
GAPDH_1, reverse	AACCATGTAGTTGAGGTCAATGAAG	82	60°C	*Homo sapiens, Macaca mulatta*
GAPDH_2, forward	AGGTCGGAGTCAACGGATTTG	254	58.1°C	*Homo sapiens, Macaca mulatta*
GAPDH_2, reverse	ATCGCCCCACTTGATTTTGG	254	58.1°C	*Homo sapiens, Macaca mulatta*
sgRNA 5, forward	CCGTCCAAGACCTACCGAGG	20	-	*Homo sapiens, Macaca mulatta*
sgRNA 5, reverse	CCTCGGTAGGTCTTGGACGG	20	-	*Homo sapiens, Macaca mulatta*
SRD5A1, forward	CCGTTTTCTAATAGGTTTTGGC	183	57.2°C	*Homo sapiens, Macaca mulatta*
SRD5A1, reverse	GCATAGCCACACCACTCCAT	183	57.2°C	*Homo sapiens, Macaca mulatta*
SRD5A2, forward	TCAATCGAGGGAGGCCTTATC	265	58.5°C	*Homo sapiens, Macaca mulatta*
SRD5A2, reverse	ACATACGTAAACAAGCCACCTT	265	58.5°C	*Homo sapiens, Macaca mulatta*
SRD5A3, forward	TGATGCAAGCACGGTGGT	124	58.4°C	*Homo sapiens, Macaca mulatta*
SRD5A3, reverse	TGAATGACCACTCCTGCTTTATT	124	58.4°C	*Homo sapiens, Macaca mulatta*

4.2 Methods

4.2.1 Cell biology tools

4.2.1.1 Cell culture and lines

Induced PSCs

Induced pluripotent stem cell lines were generated previously[115] and kept in the Degenerative Diseases Platform stock of the German Primate Center (DPZ) (Table 1). Cells were sourced from the working stock of the same passage and used for no more than 10-20 passages. Rhesus monkey RhiPSC1 and RhiPSC2 and human hiPSC1 and hiPSC2 cells were generated previously by episomal reprogramming and maintained at 37°C, 5% CO_2. Cells were fed daily with iPS-B+ medium containing StemMACS™ IPS-Brew XF, 0.5 µM Chir99021, and 1 µM IWR-1 in feeder-free conditions on plates/wells coated with 0.17 mg/mL of Geltrex™.

Passaging: Versene 1:5000 (1X) was used to pass the cells. For this, the medium was removed, and Versene was added for 2 min at RT, after which the reagent was removed and added freshly again for another round of 2 min at RT. Next, Versene was taken out and cells were detached by pipetting in iPS-B+ supplemented with 5 µM Pro-survival compound (PSC, added only on the day of passaging) and transferred to the new plate coated with Geltrex™. The morphology of iPSCs was checked daily using an inverted microscope (Zeiss, Axio Vert. A1).

Cells used for the testosterone (T) experiment were cultured in control groups of iPS-B+ and iPS-B+ supplemented with DMSO (1:2500 as used from 100 nM T). Treatment groups were fed with media additionally supplemented with 25 or 100 nM T.

Freezing: Cells were dissociated with Versene as described above and detached by pipetting with 1 mL Freezing medium containing iPS-B+, 20% v/v DMSO, 10 µM PSC. The cell suspension was transferred to cryotubes and frozen at -80°C in Mr. Frosty (Nalgene, ThermoFisher Scientific). Eventually, cryotubes were transferred to -150°C for long-term storage.

Thawing: Cryopreserved cells were thawed in a water bath of 25-37°C for 2 min and resuspended in 10 mL DMEM. Then the cells were centrifuged at 200 x g for 5 min at RT, and the supernatant was discarded. The cell pellet was resuspended in iPS-B+ supplemented with 5 µM PSC and seeded in new plates. The next day the media was exchanged to the iPS-B+ without PSC.

Prostate carcinoma cells

The 22RV1 prostate carcinoma cell line was obtained from DSMZ. Most importantly, androgen receptor variants are present and active in these cells thereby allowing its use as positive control. Cells were fed every 2-3 days with RPMI 1640 media containing penicillin (100 units/ml), streptomycin (100 µg/ml), 20 mM L-Glutamine, and 10% FBS at 37°C in a 5% CO_2 incubator. On the day of splitting, cells were washed once with DPBS and incubated with TrypLE™ Express Enzyme (1X) for 5 min, 37°C. Next, cells were transferred to the falcon with twice the volume of media and centrifuged at 200 x g, for 5 min at RT. The supernatant was removed, and the cells of the desired number were transferred to the new plate.

4.2.1.2 Cardiomyocyte differentiation

The cardiomyocyte differentiation protocol was earlier developed by Dr. Michael Stauske[115], (Fig. 8). In the present project, this protocol was further adapted to each of the cell lines, which is described in detail in the Results section. Shortly, human and rhesus iPS cells were plated on a 12-well plate coated with Geltrex™ and grown in iPS-B+ changed daily for two days. Only hiPSC2 cells were cultured for three days before differentiation. To start cardiac differentiation, the medium was changed on day 0 and 24 hours after to Mesodermal induction medium containing RPMI 1640 medium, B27™ (50x) minus insulin, 200 µM L-Ascorbic acid 2-phosphate, 1mM sodium pyruvate, 1 µM Chir99021, 5 ng/mL BMP4, and 9 ng/mL Activin-A. On days 3 and 5, the medium was replaced by a Cardiac induction medium containing RPMI 1640, B27™ (50x) minus insulin, 1 mM sodium pyruvate, 200 µM L-ascorbic acid 2-phosphate, 5 µM IWR-1. On day 7, the medium was replaced by a Cardiomyocyte cultivation medium containing RPMI 1640, B27™ (50x) with insulin, 200 µM L-ascorbic acid 2-phosphate. Cardiomyocytes were further propagated in this medium until day 12, changed every 2-3 days. Cells were monitored daily, and since day 5 the contractile activity was assessed using bright field microscopy. The first visible cell contractions (“beating”) usually occurred around day 6-9 depending on the cell lines. Afterward, cells were split and used for the selection phase or fixed for flow cytometry analysis.

Passaging and Pelleting: TrypLE™ Express Enzyme (1X) was used to pass cardiomyocytes. The cells were washed with 1 mL/well DPBS and incubated with the enzyme for 10-20 min at 37°C. Then cardiomyocytes were detached and transferred to a tube with twice the volume of the Cardiomyocyte cultivation media supplemented with 10 µM PSC to inactivate the dissociation reagent. Next, cells were centrifuged at 300 x g, for 5-10 min. The supernatant was discarded, and the cells were plated on new Geltrex™-

coated 6-well plates or were used for direct lysis or cell pellets frozen at -80°C for further analysis.

Selection: Cells were split on day 12 using TrypLE™ Express Enzyme (1X) as described above. The next day after splitting, the medium was changed, and the cells were propagated to form a monolayer (2-3 days). Afterward, the medium was replaced by a Selection medium containing RPMI 1640 without glucose, 4 mM lactate/HEPES solution, 0.2 mg/ml L-ascorbic acid 2-phosphate, 0.5 mg/ml recombinant human albumin. The medium was changed every 2-3 days for a week. On day 7, the medium was replaced by the Cardiomyocyte cultivation medium, and cells were left to recover for the next 3-7 days. Then, cells were split using TrypLE™ Express Enzyme (1X), as described above, to the new plates and used for downstream applications.

Cells used for the T experiment were cultured in control groups of Cardiomyocyte cultivation media and Cardiomyocyte cultivation media supplemented with DMSO (1:2500) equivalent of DMSO in 100 nM T. Treatment groups were fed with media additionally supplemented with 25 or 100 nM T. The cells were then incubated for 48 hours or 7 days for further analyses.

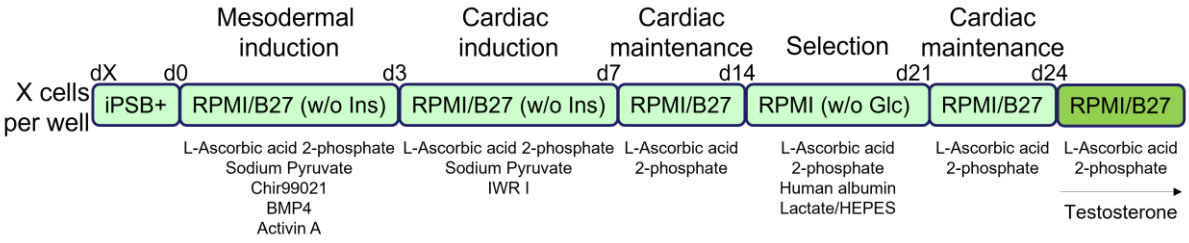

Figure 8. Scheme of the cardiomyocyte differentiation protocol.

4.2.1.3 Fluorescence-activated cell sorting (FACS)

To perform FACS analysis, cardiomyocytes were digested with prewarmed TrypLE™ Express Enzyme (1X) for 10-20 min at 37°C. The dissociation reaction was inactivated with twice the volume of the Cardiomyocyte cultivation medium. Afterward, cells were detached by pipetting and transferred to a 15 mL falcon tube. Next, the samples were centrifuged at 300 x g, 5-10 min, RT, and the supernatant was discarded. DPBS containing 4% paraformaldehyde was used for fixation for 20-30 min, after which cells were centrifuged again. Next, the samples were washed with DPBS and centrifuged. The supernatant was discarded, and cells were resuspended in 0.1% Triton X-100 in 1% BSA/DPBS for permeabilization and blocking on a platform shaker at +4°C overnight or longer.

On the scanning day, pre-treated cells were washed with DPBS and centrifuged. After removing DPBS, cells were resuspended in respective antibody solutions according to Table 4, diluted in 1% BSA/DPBS, and incubated at 37°C for 1 hour. Next, cells were washed once with DPBS and centrifuged at 300 x g for 5 min. Eventually, cells were resuspended in 200-400 µL/tube FACS buffer containing 1% BSA/DPBS, 2 mM EDTA, and transferred to a sorting tube using 100 um cell strainers (pluriStrainer® 100 µm, Pluriselect).

The cells were then scanned with Sony SH800S sorter using a gating strategy via dot plot (Fig. 9). Each analysis contained unstained, IgG-stained and cTNT-FITC stained samples. To effectively separate negative and positive population, unstained and IgG-stained samples were used to identify non-cardiac population and place Gate C. Gate D further contained only cTNT-positive cells. The data were exported using CVS files and analyzed by GraphPad Prism 8 software (Version 8.0.1).

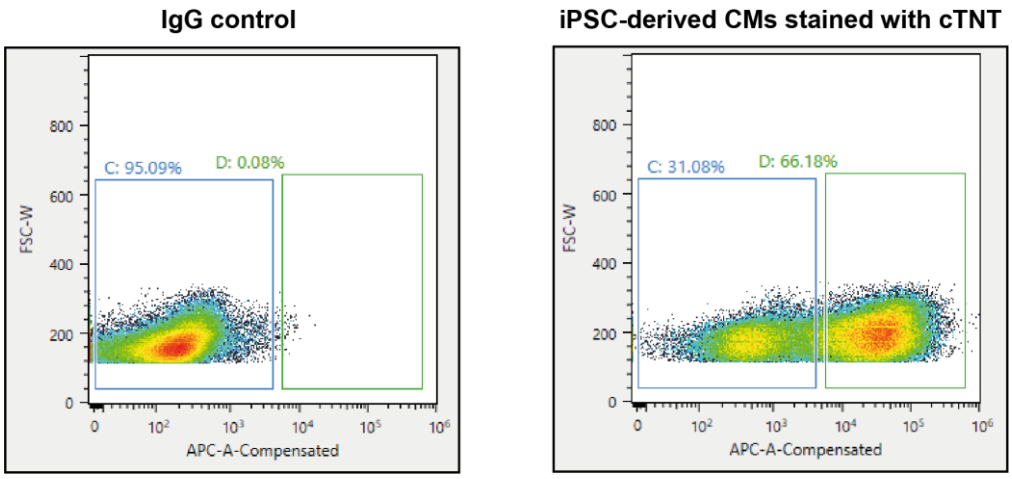

Figure 9. Gating strategy using dot plot with measured negative control (IgG) and sample. The sorting analysis was performed using a gating strategy via dot plot. Unstained and IgG-stained samples were used to define negative control gate C. Examined samples were stained with FITC- or APC-conjugated cardiac troponin T (cTNT) and scanned in separate channels. Scanning was performed using a Sony SH800S Flow cytometer. Lasers of 488 and 565 nm were used to detect FITC or APC-conjugated cTNT, respectively. The cells were sorted using 100 µm sorting chips. The data were analyzed in GraphPad Prism 8.

4.2.1.4 Immunofluorescence staining

Cells were seeded on glass coverslips (Mensel-Gläser, #CB00200RA1) coated with Geltrex™ in 6-well plates. Cardiomyocytes were seeded at 300,000 cells/well to detect cardiac markers, AR, and androgen-converting enzymes. Human iPS cells were seeded at 200,000 cells/well, and rhesus iPS cells were seeded at 100,000 cells/well to detect pluripotency markers and AR.

Initially, the cells were washed once with DPBS and fixed with 4% paraformaldehyde in DPBS for 20 min. Next, cells were washed three times with DPBS and permeabilized using 0.1% Triton X-100 in 1%BSA/DPBS. After that, the cells were washed three times with DPBS and blocked with 1% BSA in DPBS at +4°C overnight or longer.

Following blocking, cells were washed three times with DPBS and incubated with 100 µL/coverslip of primary antibodies at 37°C for 1 hour or at +4°C overnight and washed thrice with DPBS the next day. Then, cells were incubated with 100 µL/coverslip secondary antibodies at 37°C for 1 hour and washed three times with DPBS again. Next, nuclei were stained with 1 mL/coverslip of 0.1-0.2 µg/mL DAPI diluted in H_2O for 5 min in the dark. Residues of DAPI were washed thrice with DPBS and once with H_2O. Coverslips were then mounted on slides using 40 µL/slide Fluoromount-G™. The slides were sealed with nail polish and stored at +4°C in the dark.

Immunostainings were imaged using an epifluorescence microscope Zeiss Observer Z1, and a confocal microscope Zeiss LSM 800. Pictures were further analyzed using ImageJ software.

Primary antibodies were diluted in 1% BSA/DPBS according to Table 4. Secondary antibodies were diluted in 1%BSA/DPBS, according to Table 5.

4.2.1.5 Proliferation analysis

EdU Click-555 Roti® Imaging kit was used for the detection of proliferating cardiomyocytes. 300,000 cells/well were seeded on Geltrex-coated glass coverslips in 6-well plates. The next day, cells were exposed to T or DMSO. After 24 hours, half of the media was exchanged to the identical one but containing EdU based on the groups analyzed. After 48 hours of exposure to EdU, the cells were processed according to the manufacturer's instructions. The nuclei were stained with DAPI. Coverslips were mounted on slides using 40 µL/slide Fluoromount-G™. Mounting was sealed with nail polish, and slides were stored

at +4°C in the dark. Immunostainings were imaged using Zeiss Observer Z1, and three replicas were analyzed using ImageJ software using nuclei counting macro:

“setAutoThreshold("Default dark no-reset");

//run("Threshold...");

setThreshold(33, 255, "raw");

//setThreshold(33, 255);

setOption("BlackBackground", true);

run("Convert to Mask");

run("Watershed");

run("Set Measurements...", "area mean min limit display redirect=None decimal=3");

run("Analyze Particles...", "size=0.001-Infinity display exclude summarize");”

The data generated in the excel sheet was then analyzed using GraphPad Prism 8.

4.2.1.6 Sarcomere analysis

Cytoskeletal analysis of cardiomyocytes was done using SotaTool according to the developers’ instructions[118]. 250,000 cells/well were seeded on Geltrex-coated glass coverslips in 6-well plates. After splitting recovery, the cells were treated or not treated with T for 7 days. The media was exchanged every 2-3 days. After hormonal exposure, the cells were fixed and processed according to the immunofluorescence staining section detecting sarcomere protein α-actinin.

Immunostainings were imaged using a confocal microscope Zeiss LSM 800 and three replicas analyzed. At least 10 pictures were visualized from each replica and further segmented 4x4 by the software (Fig. 10). The program then analyzed segments to calculate parameters such as sarcomere length (μm) and sarcomere organisation score. This method is based on gray-level co-occurrence matrix, which translates images into arrays of i columns and j rows, one for each gray level of the original image. The sarcomeres form repeated striations that can be transformed to correlation graphs with damped oscillations. The software then finds and selects the angle at which the correlation peak is maximum to identify the direction of most clearly present sarcomeres. At this point the striation-striation difference can be determined via x-axis (Offset). It is defined as the distance and the angle α with the highest linear dependency between gray values. Sarcomere organization score is identified as the maximum peak value of the correlation graphs.

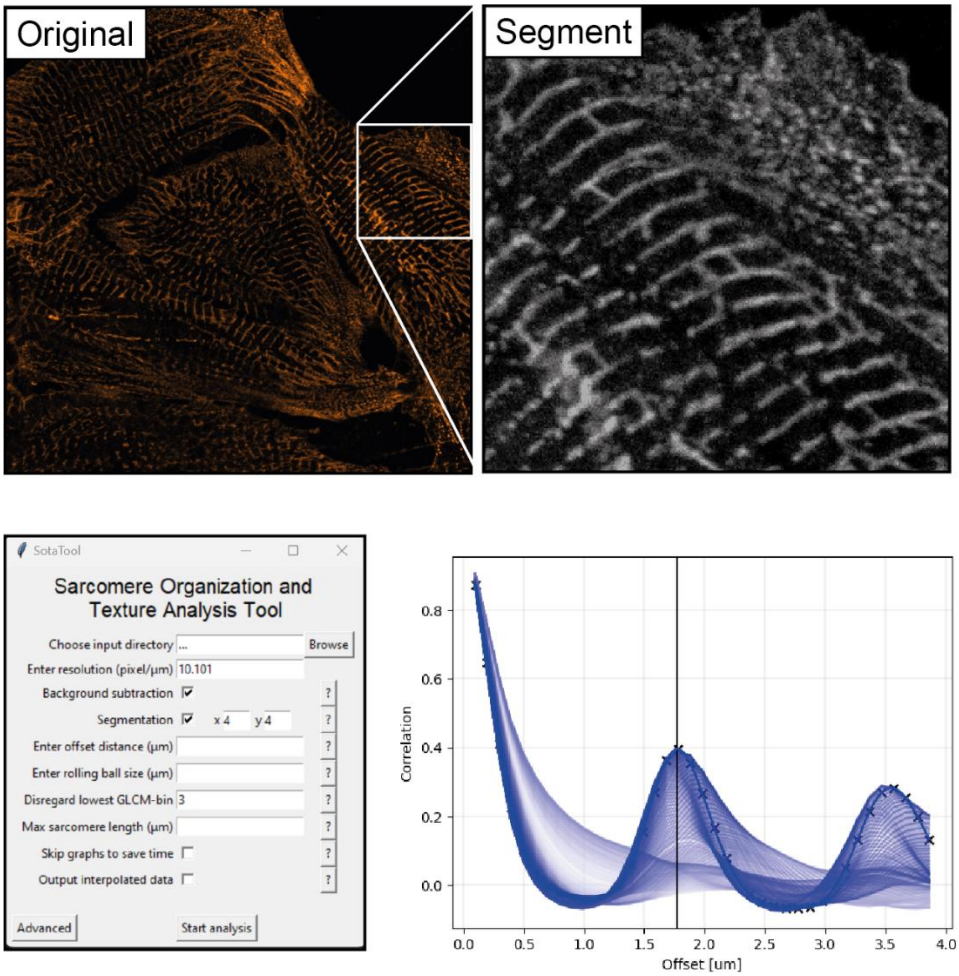

Figure 10. Representative pictures of analyzed cells stained with α-actinin and SotaTool interface with analysis output. The software interface with chosen image segmentation after analysis provides results in sarcomere analysis following signal correlation. The straight line determines the highest correlation score, while the respective x-axis number refers to sarcomere length (Offset).

4.2.1.7 Immunohistochemistry staining

Paraffinized tissues were kindly provided by the Pathology Unit and Degenerative Diseases Platform, DPZ (Table 2). Organ samples were previously fixed in Bouin's solution (75% picric acid, 25% formaldehyde, 5% glacial acetic acid), 4% PFA or 10% Formalin immediately after recovery for at least 6 hours. After several washes in 70% ethanol for at least two days, the tissues were embedded in paraffin and sectioned at 5 µm for immunohistochemistry staining or 3 µm for immunofluorescence staining.

Initially, the tissues were deparaffinized using Xylol incubation in three glass cuvettes at RT for 5, 2, and 2 minutes, respectively, under the laboratory hood. Next the blocks were

sequentially rehydrated in glass cuvettes starting with 100% (2 min), 90% (2 min), 80% (1 min) and 70% (1 min) ethanol and finishing with ddH_2O at RT. Next, antigen retrieval was performed using 10 mM sodium citrate buffer (pH 6,0). The slides were microwaved for 10 minutes at medium-high level. After that, the slides cooled for at least 30 minutes. The samples were further washed for 5 min with a washing buffer containing 0.05 M Tris, 0.15 M NaCl (pH 7,6) at the orbital shaker. Following, the tissue sections were incubated for 15 min in Peroxidase Block solution from Envision FLEX Mini Kit, High Ph. After incubation, the slides were washed for 5 min at RT. Next, the primary antibodies diluted in 3% BSA/DPBS were placed onto tissue sections (30 uL/small section, 40-50 uL/big section). The incubation was then carried out overnight in a humidified chamber.

Next day, the slides were washed twice for 10 minutes at RT. Tissue sections were incubated for 30 minutes with EnVision FLEX/HRP dextran coupled secondary antibodies developed against mouse and rabbit immunoglobulins. After that, the slides were washed twice for 10 minutes at RT. Next, the staining substrate DAB from the kit was used to generate a brown color, which reflects protein detection. One drop of Chromogen was mixed with 1 mL of Substrate buffer and immediately placed on tissue sections (30 uL/small section, 40-50 uL/big section). The reaction was stopped with water when the color intensity had reached its peak (5-15 min for different antibodies). The slides were further counterstained with Mayer's Hemalaun solution for 1-3 min, then dipped in 0.1 HCl and rinsed twice in tap water cuvettes. Next, the slides were placed under flowing water for 10-15 min to rinse the leftovers. Glycergel (DAKO) was used to preserve the slides. This water mounting medium was heated up to 50°C and 3-4 drops were placed on the glass slide. Next, the coverslip was placed on top and the leftover Glycergel was collected on the edge of the slide with paper tissues. The slides were left to dry under the laboratory hood. Tissue sections were then analyzed using a microscope (Zeiss, Axio Vert. A1).

4.2.1.8 Patch-clamp analysis

Human iPSC-CMs plated 15,000 cells/well on glass coverslips were treated with 25 nM and 100 nM T for 24 and 48 hours. Control groups comprised cells with standard media and DMSO (1:2500) according to its amount for the 100 nM T group. Cells were then placed in a recording chamber perfused with a sodium-free extracellular solution containing (in mM): TEA-Cl 136, $CaCl_2$ 2, $MgCl_2$ 2, HEPES 25, and glucose 20; pH adjusted to 7.4 with CsOH. The pipette solution contained (in mM): CsCl 130, EGTA 10, Mg-ATP 2, and HEPES 25; pH was adjusted to 7.2 with CsOH. The cells were patch-clamped at room temperature using an EPC-10 amplifier (HEKA Electronics, Germany) controlled by *Patchmaster* software. All

voltages were corrected for the liquid junction potential of 6.7 mV offline. Cells were kept at a holding potential of -76.7 mV. During recording the leak current was subtracted using a p/10 protocol during which the cells were depolarized ten times to measure the leak current values. The latter were further subtracted from the measurement as a background signal. Current voltage relationships (IVs) were recorded by applying 10 ms-long step depolarisations of voltages ranging from -76.7 to 78.3 mV, in 5 mV steps.

4.2.2 Molecular Biology methods

4.2.2.1 RNA isolation and PCR

RNA was extracted using ReliaPrep™ RNA Miniprep Systems from human and rhesus samples (cells and tissues) according to the manufacturer's instructions with the following modifications.

iPSC and iPSC-CMs: The media was removed and 500 µL LBA was added per one well of a 6-well plate to lyse the cells. Next, the samples were transferred to 1.5 mL tubes and centrifuged at 14,000 x g for 2-5 min. The supernatant was then processed according to the manufacturer's instructions. DNase treatment is included in the kit and was performed accordingly. Eventually, every sample yielded 20-30 µL of eluted RNA.

Tissues: The samples were retrieved from -80°C storage and placed in the liquid nitrogen container. Next, each cryotube was handled individually. For this, the frozen tissue was placed on a 10 cm plastic dish, and the small piece was cut before excessive thawing. Next, the slices were placed in tubes, and their weight was measured. Up to 30 µg of tissue was processed using the manufacturer's instructions. Every sample was eluted in 30 µL of RNase-free water.

The RNA concentration was measured using a Qubit 4 Fluorometer by incubating 1 µL of RNA sample with a Qubit™ RNA Broad Range Assay kit.

For cDNA synthesis, 500 ng or 1 µg of total RNA was reverse transcribed with Oligo(dT) primers using Omniscript RT Kit (200) according to the manufacturer's instructions. Next, both cDNA-containing samples and negative controls were used for PCR with primers to detect genes of interest (Table 8). GAPDH primers were used to check the presence of gDNA and the quality of samples. Finally, generated extracts were visualized using 1-2% DNA agarose gel electrophoresis containing Ethidium bromide (EtBr). Samples were mixed with 2 µl of Gel Loading Dye each and run in 1X TAE Buffer at 100 V for 30 min; 1 kB plus DNA Ladder was used as a reference. Gels were imaged via the Intas illuminator.

A StepOnePlus System (Applied Biosystems, USA) was used to perform real-time quantitative PCR. Complementary DNA was diluted in H_2O in a 1:5 (for 500 ng RNA) and 1:2.5 (for 1 µg RNA) ratio. The RT-qPCR was measured in MicroAmp® Fast 96-well Reaction Plates; each well contained 1 µL of cDNA dilution, 10 µL of Power SYBR® Green PCR Master Mix, 2 µL of each 2 µM primer mix (Table 8) and 5 µL of Nuclease-free water. The results were further exported via Microsoft Excel and analyzed in GraphPad Prism 8.

4.2.2.2 Total RNA sequencing

The total RNA of cardiomyocyte cultures was isolated as described above. RNA quality was assessed by measuring the RIN (RNA integrity number) using a Fragment Analyzer (Advanced Bioanalytical) selecting samples with a RIN>8.

Library preparation for RNA sequencing was performed using the Illumina Stranded mRNA Prep (Cat. N°20040534) and RNA UD Indexes Set A, Ligation 96 Indexes (Illumina Cat. N°2 0091655) starting from 200 ng of total RNA. Accurate quantification of cDNA libraries was performed by using the QuantiFluor dsDNA System (Promega). The size range of final cDNA libraries was determined by applying the DNA 1000 chip on the Fragment Analyzer (average 290–320 bp). cDNA libraries were amplified and sequenced by using the NovaSeq6000 instrument (PE 100 cycles; S2 flow cell ~20-25 Mio reads per sample).

Raw read & Quality check: Sequence images were transformed with Illumina software BaseCaller to BCL files, which was demultiplexed to fastq files with bcl2fastq v2.20. The sequencing quality was asserted using FastQC[119].

Mapping & Normalization: Sequences were aligned to the reference genome Homo sapiens (GRCh38.p13, Ensembl) using the RNA-Seq alignment tool[120] allowing for 2 mismatches within 50 bases. Subsequently, read counting was performed using featureCounts[121].Read counts were analyzed in the R/Bioconductor environment (version 4.3.1, www.bioconductor.org) using the DESeq2[122] package version 1.40.2. Candidate genes were filtered using an absolute log2 fold-change >1 and FDR-corrected p-value <0.05.

Differentially expressed genes that were potentially regulated were selected for gene set enrichment analysis (GSEA) embedded into the R package WebGestaltR[123].

4.2.2.3 CRISPR/Cas9 vectors preparation

For the generation of the androgen receptor knock-out cell line two vectors were used, Ptt-PB-eCas9-GFP-gRNA and pBase-tdTomato, kindly provided by Stoyan Petkov, PhD, and Dr. Rodriguez Polo.

Ptt-PB-eCas9-GFP-gRNA was generated by cloning the CRISPR/Cas9 system from pCAG-eCas9-GFP-U6-gRNA (addgene #79145) into a PiggyBac vector backbone with the addition of neomycin-resistant cassette by Stoyan Petkov. The detailed protocol was published recently[124].

Single guide RNA 5 was designed to mutate AR in human exon 1 using the Zhang Lab CRISPR Design website (https://zlab.bio/guide-design-resources). The RNA guides were ordered as oligonucleotides (Table 8) from Sigma-Aldrich and cloned individually into Ptt-PB-eCas9-GFP-gRNA vectors. For this purpose, the vector was linearized using the restriction enzyme BbsI-HF® and purified from DNA agarose gel using the NucleoSpin® Gel and PCR Clean-up Kit. Strands of sgRNAs were assembled by aligning each pair of oligonucleotides by incubation with T4 PNK for 30 min at 37°C following 5 min at 95°C and gradually reducing the temperature to 4°C. Eventually, the guides were ligated individually into the linearized vectors with T4 DNA ligase (NEB, M0202).

4.2.2.4 Transformation and plasmid isolation

I transformed competent DH5α bacteria (genotype: F- ϕ80lacZ∆M15 ∆(lacZYA-argF)U169 recA1 endA1 hsdR17(rk- , mk+) phoA supE44 thi-1 gyrA96 relA1 λ-) with the generated vectors using a heat-shock protocol. First, bacteria were incubated with 5 µL of plasmid on ice for 30 min. Then the heat-shock was performed by 30 sec incubation of bacteria at 42°C. Following the 5 min incubation on ice, bacteria were then recovered during incubation in SOC medium for two hours at 37°C and plated into LB agar dishes with 100 µg/mL ampicillin. The dishes were incubated overnight at 37°C and screened for colonies in the morning.

For mini/maxi preparation, the same culture conditions were used, and the bacteria cultured in liquid LB/Ampicillin media with the potential positive clone from transformation with a final volume of 3 mL for up to 20 µg of plasmid using GeneJet Plasmid Miniprep Kit or 100 mL for up to 500 µg of plasmid using QIAGEN-tip 500 Maxi kit according to manufacturers' instructions. Plasmids were then sequenced to detect sgRNA insert and used for maxi preparation to produce a higher yield used for further transfection.

4.2.2.5 Transfection of induced pluripotent stem cells

I transfected the hiPSC1 line using lipofection as the lipid-based method using Lipofectamine™ 3000 Transfection Reagent according to the manufacturer's instructions. Initially, cells were cultured in a 6-well plate until ~ 70% confluence. To increase transfection efficiency, cells were detached with StemPro Accutase® by incubation for 5 min. Then the cells were transferred to a 15 mL tube and diluted 1:1 within iPS-B+ medium for human cells to inactivate the reagent. Next, the samples were centrifuged for 5 minutes at 200 x g and seeded on the new plate with fresh medium. Two µg of Ptt-PB-eCas9-GFP-gRNA and three µg of pBase-Tomato were added to the transfection reaction (Fig. 11). No plasmids were added to generate negative control. Transfection with Ptt-PB-eCas9-GFP with no sgRNA and pBase-Tomato was used as positive control. Next, the reaction cocktail in Opti-MEM™ media was added to each single well with the detached iPSCs. After a few hours, the media was exchanged to iPS-B+ supplemented with 5 µM Pro-survival compound.

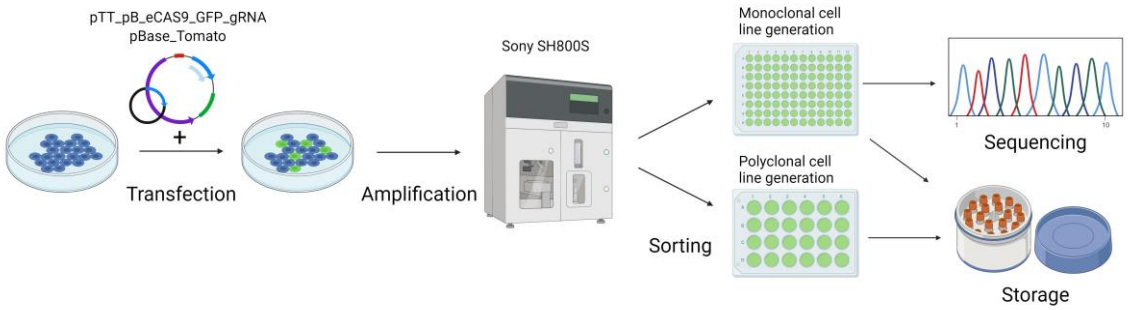

Figure 11. Schematic overview of the generation of AR KO iPSCs. Created with Biorender.

The next day, fresh media was added, and cells were daily checked for viability and fluorescence. The cultures were propagated for one passage and then used for single-cell sorting using a Sony SH800S sorter as published previously [124]. Shortly, transfected cells were sorted based on fluorescence from GFP fused with eCas9. For that, cells were detached using pre-warmed Versene, 5 min. Next, cells were transferred to a 15 mL falcon tube with DMEM and centrifuged for 200 x g, 5 min, at 4°C. The samples were then transferred to a new falcon tube using 40 um strainer and sorted one cell/well in 96-well plates at 4°C. Next, transfected cells were propagated, pelleted, and genomic DNA was extracted using DNeasy® Blood and Tissue Kit. DNA samples were sent to LGC genomics for mutation analysis by sequencing. Eventually, only transfection with sgRNA5 resulted in a mutation.

4.2.2.6 Protein isolation and Western Blot

Induced PS cells and iPSC-CMs were harvested on ice by washing twice with ice-cold DPBS and detached with a cell scraper. Next, the cell suspension was centrifuged at 2000 x g, +4°C, and the supernatant was removed. Cells were then resuspended in 400 uL for iPSCs and 300 uL for iPSC-CMs of RIPA lysis buffer supplemented with Halt™ Protease Inhibitor Cocktail (100X). Next, the lysate was centrifuged at 14,000 x g for 15 min, and the supernatant was transferred to the new labeled tube. The protein concentration was measured using PierceTM BCA Protein Assay Kit by measuring the absorption spectra using IMPLEN P300 NanoPhotometer. Next, the samples were boiled for 10 minutes at 95 °C in the Loading buffer 6x Laemmli (0.35 M pH 6.8 Tris-HCl, 30% Glycerine, 10% SDS, 9.3% DTT, 0.02% Bromophenol Blue) to denature proteins. The protein samples were stored at -20 °C.

For SDS-PAGE, 7.5% or 10% polyacrylamide gels were prepared in advance, consisting of resolving (7.5% or 10% Acrylamide, 375 mM pH 8.8 Tris-HCl, 0.1% SDS, 0.1% APS, 0.4% TEMED) and stacking (5% Acrylamide, 126 mM pH 6.8 Tris-HCl, 0.1% SDS, 0.1% APS, 0.3% TEMED) gel. 20 µg of protein was loaded into the stacking gel. Spectra™ Multicolor Broad Range Protein Ladder was used to monitor protein molecular weight. Electrophoresis was carried out at 25 mA in an electrophoresis chamber filled with SDS-PAGE running buffer (25 mM Tris-HCl, 3.5 mM SDS, 192 mM Glycine). Protein separation was conducted for 2.5-3 hours.

Following SDS-PAGE, proteins were transferred to Immobilon®-P membrane. Gels and membranes were placed in a semi-dry chamber in a sandwich-based method of the following order. Lower panel (anode), two filter papers soaked with Anode buffer 1 (0.3 M Tris/HCl, 20% methanol), one filter paper and membrane soaked with Anode buffer 2 (0.025 M Tris/HCl, 20% methanol), SDS-PAGE gel, three filter papers soaked with Cathode buffer (0.025 M Tris/HCl, 20% methanol, 0.04 M glycine) and eventually upper panel, cathode. The transfer was carried out at 145 mA, 100 V, for 45 minutes at RT. Afterward, the membranes were blocked in 5% milk powder in 0.1% Tween 20/Tris-buffered saline (TBS-T) overnight at 4°C. Next, the membrane was washed thrice for 5 minutes with TBS-T. The primary antibodies were then added to the respective blot and incubated overnight at +4 °C on a roller. All primary antibodies were diluted 1:1000 in TBS-T except AR and α-tubulin, which were diluted 1:2000 in TBS-T. Unbound antibodies were washed away three times, 5 minutes, with TBS-T, and HRP-coupled secondary antibodies diluted in 1% BSA in TBS-T were added for 1 hour at room temperature, followed by three times washing with TBS-T for 5 minutes each. For antibody detection by chemiluminescence, Pierce™ ECL Western

Blotting Substrate solution was added. The emitted light was detected by a ChemiDoc MP Imaging System (Bio-Rad), and images analyzed using the ImageJ software.

4.2.2.7 Sample extraction and hormone analysis by LC-MS/MS

Cardiomyocytes were plated at 300,000 cells/well on glass coverslips of 6-well plates and treated with DMSO (control), 25 nM T, and 100 nM T (Fig. 12). Twenty-four and 48 hours later, 1 mL/well of media was collected from each group and frozen at -20°C. Subsequent analysis was kindly done by Dr. Annekathrin Keiler, Institute of Doping Analysis and Sports Biochemistry, Dresden. One mL of the cell culture supernatant was supplemented with 10 µL of IS D3-T-gluc (1µg/mL) to prepare loading solution. The solid phase extraction was performed on Waters Oasis HLB cartridges 1 cm^3 (30 mg, Walters) according to the manufacturer's protocol.

Shortly, cartridges were conditioned with 1 mL methanol and then equilibrated with 1 mL water. Next, the cell culture supernatants containing IS were loaded on the cartridge. Following the washing step with 1 mL water, the analytes were eluted with 1 mL methanol. The eluates were divided into two fractions of 0.5 mL each and independently evaporated under the effect of N2 to dryness. Fraction 1 was reconstituted with 50-µl mobile phase A/mobile phase B (3:2, v/v) and measured subsequently via liquid chromatography–tandem mass spectrometry (LC–MS/MS) analysis. The aqueous mobile phase A consisted of 2 mM ammonium acetate, 0.1% acetic acid (v/v) in water/acetonitrile (95:5, v/v), and the organic phase B consisted of 2 mM ammonium acetate, 0.1% acetic acid (v/v) in water/acetonitrile (5:95, v/v). After addition of 1 mL of phosphate buffer (0.5 M KH_2PO_4 + 0.5 M Na_2HPO_4, 8:5, v/v, pH 6.5) and 20 µl of β-glucuronidase (140 U/ml), fraction 2 underwent hydrolysis at 55° C for 1 h. Following pH adjustment by adding solid carbonate buffer ($NaHCO_3$ + K_2CO_3, 84:138, m/m), liquid-liquid extraction was performed using 2.5 mL MBTE. The organic phase was evaporated to dryness and dissolved in 50 µL mobile phase A/mobile phase B (2:3, v/v).

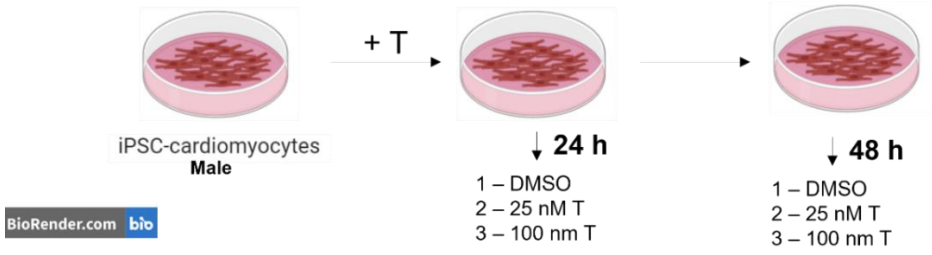

Figure 12. Schematic overview of media retrieval samples from hiPSC1 and RhiPSC1-CMs treated and non-treated with T. Created using Biorender.

An Agilent 1290 system was used to perform the ultra-high performance liquid chromatography (UHPLC) separation with a ZORBAX Eclipse XDB-C8 3.5 µm x 2.1 mm x 100 mm column (Agilent Technologies). The temperature of the column was set to 40°C, and the sample injection volume was 10 µl for MS and 1 µl for MS/MS analyses. The column was equilibrated for 2.5 min at 80% A with a flow rate of 180 µl/min. This was followed by a 1-minute period at 80% A at a flow rate of 200 µl/min. Afterward, it decreased to 40% A over 7 min at 350 µl/min and to 0% A for 1.5 min with a flow rate of 450 µl/min. It was then increased to 80% A for 0.4 min at 300 µl/min before being held at 80% A for 0.1 min with a flow rate of 180 µl/min. A hybrid quadrupole time-of-flight (ToF) mass spectrometer (TripleTOF® 6600, AB Sciex, Darmstadt, Germany) was coupled to the UHPLC. The ion source temperature was set to 600°C, and the ion spray voltage was with the curtain gas pressure set to 40 psi. Ion source gas pressure 1 and 2 were set to 55 psi. For MS experiments, mass spectra were obtained over a scan range of 100–800 Da in positive mode. The analysis was achieved using Analyst TF® 1.71 and Peak View® 2.2 (AB Sciex, Darmstadt, Germany).

4.2.2.4 Testosterone and estradiol measurement in rhesus macaque samples using ELISA

The serum of rhesus macaque was kindly provided by the Pathology Unit and Degenerative Diseases Platform, DPZ. The serum was analyzed for concentrations of immunoreactive T and immunoreactive 17ß-estradiol in the DPZ´s Endocrinology Laboratory using an enzyme immunoassay. Prior to hormone measurements, serum samples (150 µl each) were extracted with 1.5 ml diethyl ether by vortexing for 10 min at 2000 rpm on a multi-tube vortexer. For separation of the organic and water phase, the samples were placed in a bath of methanol/dry ice for 2 min. After the water phase had frozen, the liquid ether phase was decanted into a new tube. The water phase was then thawed, and the extraction was repeated.

After the second ether phase was combined with the initial extract, the samples were placed into a heating block at 30°C for evaporation under a stream of nitrogen. After the ether was completely evaporated, 300 µL of assay buffer (PBS, pH 7.2) was added to each sample tube. The solution was then vortexed for 5 min and left at +4°C overnight.

The next day, T and 17ß-estradiol were measured in the sample extracts using in-house microtiter plate enzyme immunoassay (EIA) procedures. T was determined by an EIA using an antiserum raised in rabbits against testosterone-3-CMO-BSA. Prior to assay, samples

were diluted 1:20 in assay buffer and subsequently measured as described[125]. In brief, duplicate 50 µl aliquots of diluted samples were combined with 50 µL HRP-labelled T and 50 µL T antiserum and incubated overnight at 4°C. Following incubation, the plates were washed four times. 100 µL of TMB substrate solution was added and the plates were incubated in the dark at room temperature for 1 hour. The enzyme reaction was finally stopped by the addition of 50µl 2M H_2SO_4 to each well and optical density was measured at 450 nm (reference 630 nm) in a plate spectrophotometer (EL 808, BioTek Instruments GmbH; Bad Friedrichshall, Germany).

17ß-estradiol was determined by an EIA using an antiserum raised in sheep against 17ß-estradiol-6-CMO-BSA and 17ß-estradiol-HRP as enzyme labels. Prior to assay, samples were diluted 1:2 in assay buffer and samples were measured in duplicate in the same way as described for the measurement of T. The data were further processed by Microsoft Excel.

4.2.3 Statistical analysis

The raw data was generated and stored in Excel files. Statistical analysis and graph generation were conducted using GraphPad Prism 8 software (Version 8.0.1). Experimental data obtained from qPCR, Western blot, patch clamp, sarcomere, and proliferation analyses are presented as mean ± standard deviation (SD). For comparison of two data sets, a two-tailed unpaired Student's t-test was applied. For the comparison of more than two variables, a two-way repeated analysis of variance (ANOVA) with a post-hoc Tukey test was applied. Since patch-clamp analysis produced non-parametric data, Kruskal Wallis with post hoc Dunn's test was used for analysis. Statistical significance is expressed by the p-value represented as (*) $p < 0.05$, (**) $p < 0.01$, (***) $p < 0.001$, (****) $p < 0.0001$.

5 Results

5.1 Fine-tuning the protocol for cardiac differentiation of primate iPSCs

The focus of this project lies on investigating the androgen receptor-mediated T action in primate cardiomyocytes. In pursuit of lacking *in vivo* and *in vitro* data, heart tissue sections from rhesus macaque and iPSC-CMs were utilized. The initial step involved the generation of cardiac cells from primate iPSCs available in the Platform Degenerative Diseases (PDE).

Two human (male hiPSC1 and female hiPSC2) and two rhesus macaque (male RhiPSC1 and female RhiPSC2) iPS cell lines were employed to generate cardiomyocytes (Fig. 13). Human iPSCs exhibited features indicative of stem cell colonies such as radiant well-defined cell borders and high nuclei/cytoplasm volume ratios. Rhesus iPS cells displayed less compactly arranged colonies with less defined cell borders.

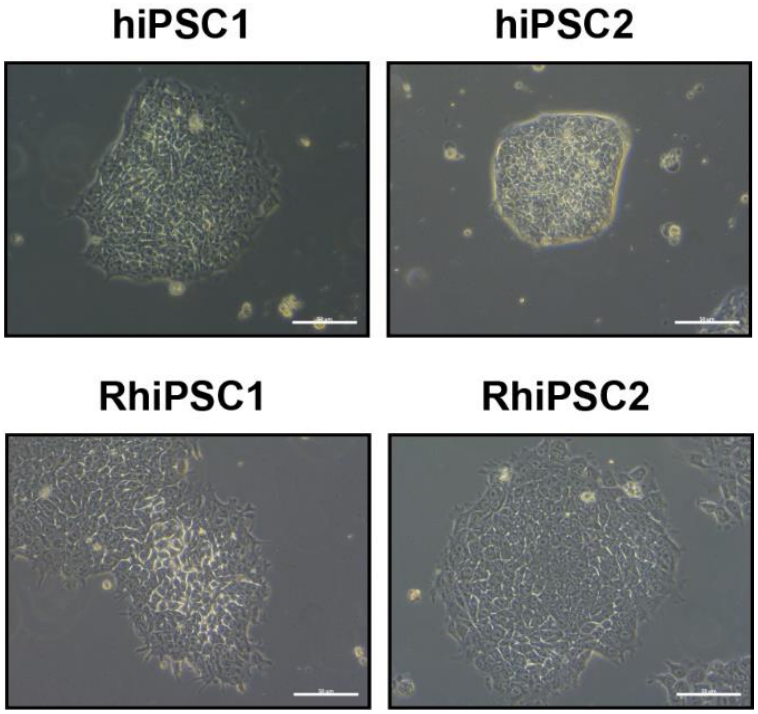

Figure 13. Morphology of human (hiPSC1 and hiPSC2) and rhesus (RhiPSC1 and RhiPSC2) induced pluripotent stem cell colonies. Scale bars: 50 µm.

Before the beginning of this project, all four iPSCs were characterized by the PDE, confirming the presence of key pluripotency marker expression and differentiation potential[115]. Karyotyping was performed to rule out possible chromosomal abnormalities. Figure 14 shows representative pictures of pluripotency markers for all four iPSC lines of the actually chosen passages from the working cell bank serving as a baseline for future cardiac differentiations.

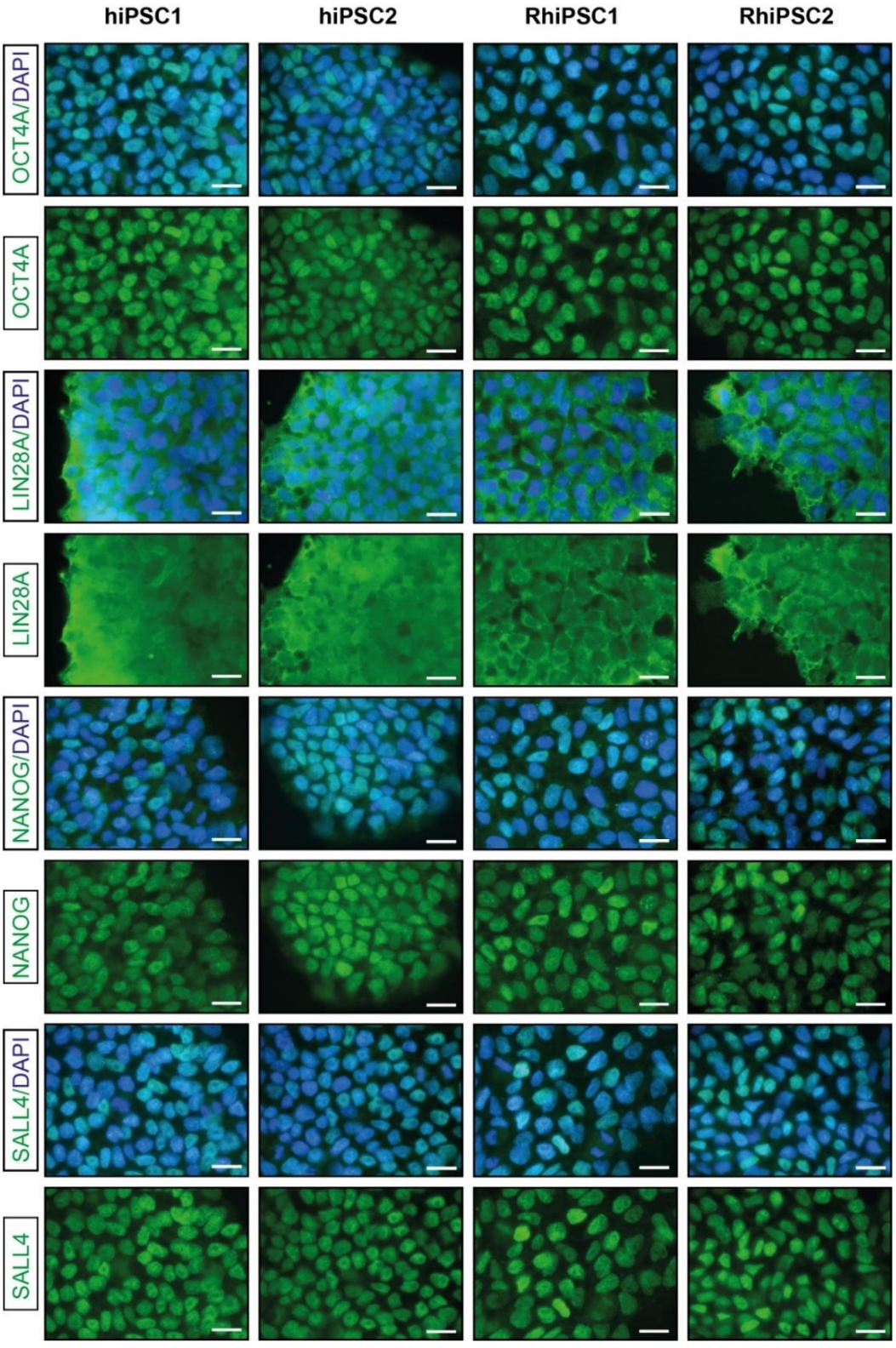

Figure 14. **Immunostaining of hiPSCs and RhiPSCs detecting pluripotency markers.** The majority of cells in the four cell lines exhibited positive immunoreactivity for the transcription factors NANOG, OCT4A, SALL4, and cytoplasmic marker LIN28A. The cell nuclei were stained with DAPI. Scale bars: 20 μm.

A plethora of cardiac differentiation protocols have been published in recent years, primarily tailored for human cell lines.[126]. However, the translatability of these approaches to cells of other primate species is not assured. Previously, in our lab, Stauske et al. specifically adapted and optimized a protocol for cardiac differentiation of non-human primate iPSCs, that was also applicable to human iPSCs [115]. Adhering to the protocol involves the beginning of cardiac differentiation when iPS cell confluence reaches 80-90%. Early attempts to achieve cardiac differentiation of multiple cell lines revealed substantial variability in the yield of cardiac cells across batches of experiments[127]. This was evident through the observation of the number of beating clusters during the protocol progression and the percentage of cardiac Troponin T (cTNT) at day 12 after initiating differentiation. In contrast to human cells, which had higher success rates, rhesus macaque cells are less prone to produce at least 50% of cardiomyocytes while following the defined protocol. Moreover, adherence to confluence guidelines for rhesus cells often led to the generation of little or no beating clusters. To reduce the influence of heterogeneity, a working bank was created, ensuring consistent passage numbers for cells taken to differentiate into cardiomyocytes.

Given the importance of maintaining a standardized protocol applicable to translational medicine, no modifications were introduced to the composition of media or the protocol itself. A close but more precise parameter to confluence is the cell seeding number. The protocol states that 80-90% confluence is needed to start differentiation. We decided to explore not confluence but a range of specific cell seeding numbers. Following a series of preliminary experiments (data not shown), five or six different cell seeding densities were chosen for each cell line to obtain the highest percentage of cardiomyocytes (Fig. 15A). The upper limit of cell seeding represents 100% cell confluence at the beginning of cardiac differentiation. A step of 20,000 cells/well was chosen between various seedings in rhesus iPS cells. Due to the high proliferation rate of hiPSC1, 50,000 cells/well step was employed. On the other side, only 10,000 cells/well step was used for hiPSC2 due to differences in colony expansion differences compared with other cell lines. hiPSC1 in smaller than 150,000 cells/well density was not able to properly attach to the plates. However, hiPSC2 cells can attach in smaller numbers so they were expanded for three days before the beginning of differentiation instead of two for other cell lines. This also allows the reduction of costs for iPSC maintenance during differentiation.

Ultimately, the seeding of 300,000 cells/well of hiPSC1 and 70,000 cells/well of hiPSC2 yielded the highest proportions of cardiomyocytes generated, 76.19 ± 4.13% and 76.52 ± 1.99% respectively (Fig. 15A). It is essential to emphasize that several cell seeding numbers resulted in more than 70% cardiomyocytes, which considered as a standard threshold for further culture applications. In contrast to human cells, only one seeding condition of each

RhiPSC1 and RhiPSC2 yielded the highest percentage of 57.95 ± 5.1% and 64.82 ± 1.98%, respectively.

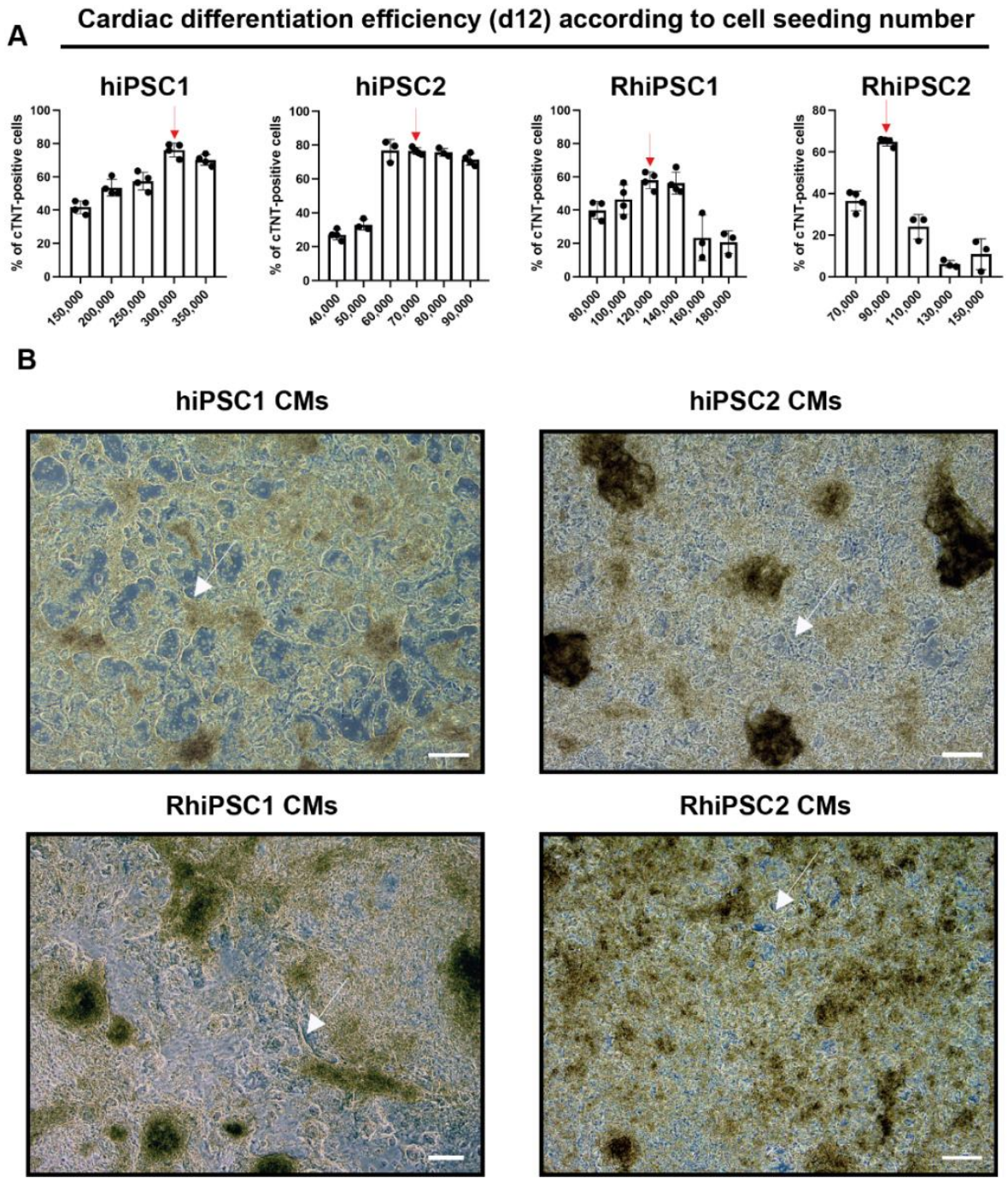

Figure 15. Directed cardiac differentiation of hiPSCs and RhiPSCs. (A) Flow cytometric measurement of cTNT signal at day 12 in four cell lines seeded with different cell numbers. The red arrow indicates the highest percentage of cTNT-positive cells for each of the four cell lines. This number of cells indicates the cell seeding used further for experiments. **(B)** Morphology of human and rhesus iPSC-CMs upon optimization of the seeding number at day 12 since the beginning of differentiation. A white arrow indicates cardiac beating tissues that resemble a spider net. Scale bar: 100 µm.

As depicted in Fig. 15A, the seeding difference of ± 20,000 rhesus cells resulted in a clear reduction in the number of generated cardiomyocytes in rhesus cells, particularly in RhiPSC2. Moreover, adherence to the recommended 80-90% confluence guidelines[115] did not correlate with the observed outcomes. Specifically, the two highest cell seeding numbers reflecting the recommended confluence range resulted in less than 30% rhesus cardiomyocytes in both cell lines. In contrast, human cell lines have shown consistency in generating more than 70% cardiomyocytes in the higher cell seeding numbers.

Figure 15B depicts bright field images illustrating typical cardiac tissue morphology from directed differentiation of iPSCs. The development of net-like structures is a common feature of early cardiac cultures before the selection process. Remarkably, the beating of this network started on days 7-8 indicating successful generation of cardiomyocytes.

Based on these results, the first splitting of cardiomyocytes was done. To perform the selection process, lactate was used since only muscle cells can use it as a substitute for glucose[128]. The use of lactate for metabolic selection led to a reduction in the non-cardiac cell population resulting in 97.47 ± 0.37%, 72.26 ± 2.32%, 87.2 ± 5.35%, and 95.68 ± 0.46% cardiomyocytes in hiPSC1, hiPSC2, RhiPSC1 and RHiPSC2, respectively (Fig. 16).

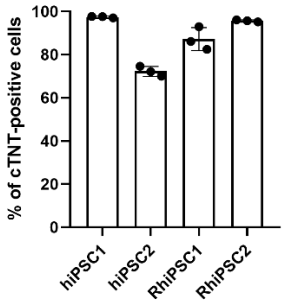

Figure 16. Flow cytometry analysis of cardiac differentiation efficiency of hiPSCs and RhiPSC seven days after metabolic selection with lactate.

Following the second splitting of cardiomyocytes after selection, cells were examined for the presence of cardiac markers as illustrated in Figure 17. Each of the four cell lines exhibited different morphologies, including round, spindle-shaped, and multiangular. Immunostaining revealed the expression of cardiac markers such as myosin light chain 2 ventricular (MLC2v), myosin light chain 2 atrial (MLC2a), α-actinin, and cardiac troponin T (cTNT). Moreover, these proteins formed organized striations with visible sarcomere structures, indicative of the successful generation of cardiomyocytes. Furthermore, cell-cell contacts with functional relevance for electric coupling were demonstrated with connexin 43 (Cx43) staining. This protein is essential for proper electrical signal propagation and

synchronous beating, crucial for the further development of contraction features[129]. Interestingly, MLC2v is mainly expressed in RhiPSCs, while both, MLC2v and MLC2a, were present in hiPSCs. This knowledge points to nuanced differences in cardiac marker expression across the distinct cell lines.

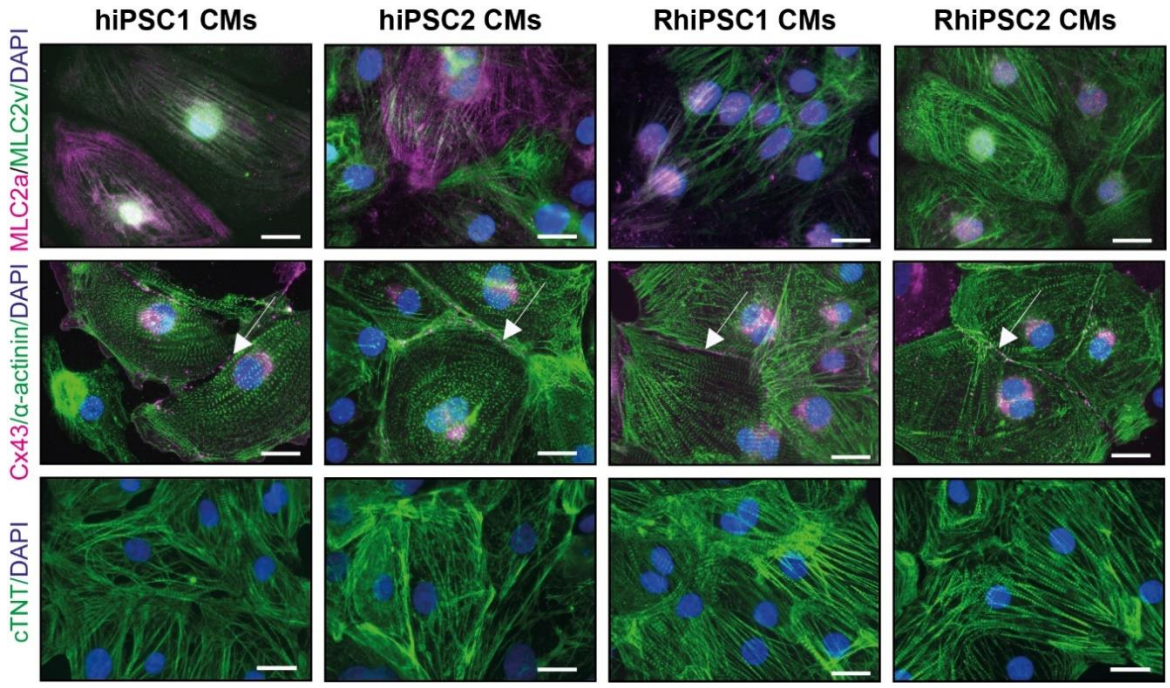

Figure 17. Immunostaining in hiPSC and RhiPSC-derived cardiomyocytes of cardiac-specific markers such as myosin light chain 2 ventricular (MLC2v), myosin light chain 2 atrial (MLC2a), α-actinin, cardiac troponin T (cTNT) and connexin 43 (Cx43). Fluorescence images show the typical structure and morphology of iPSC-CMs forming striated patterns of sarcomeres. The cell nuclei were stained with DAPI. Scale bars: 20 µm.

5.2 Androgen receptor in rhesus macaque male and female hearts

To establish an in vivo context for this project, we utilized heart tissue sections from the DPZ archive, obtained from four healthy male and five female subjects. The primary goal was to investigate the presence and localization of androgen receptor in primate cardiomyocytes in vivo / in situ. Immunohistochemistry analysis revealed positive brown staining in several cardiomyocyte nuclei of male hearts, while no signal in female hearts was detected (Fig. 18A).

Additionally, in collaboration with the Endocrinology Laboratory of the DPZ and the Pathology Unit of the DPZ, we determined T and E2 ranges in the blood serum of those monkeys, whose tissues underwent immunohistochemical staining. The results demonstrated a significantly higher T concentration in male serum compared with female

serum (Fig. 18B). T serum levels were 10.18 ±1.89 ng/mL in male macaques compared with 0.67 ±0.3 ng/mL in female macaques.

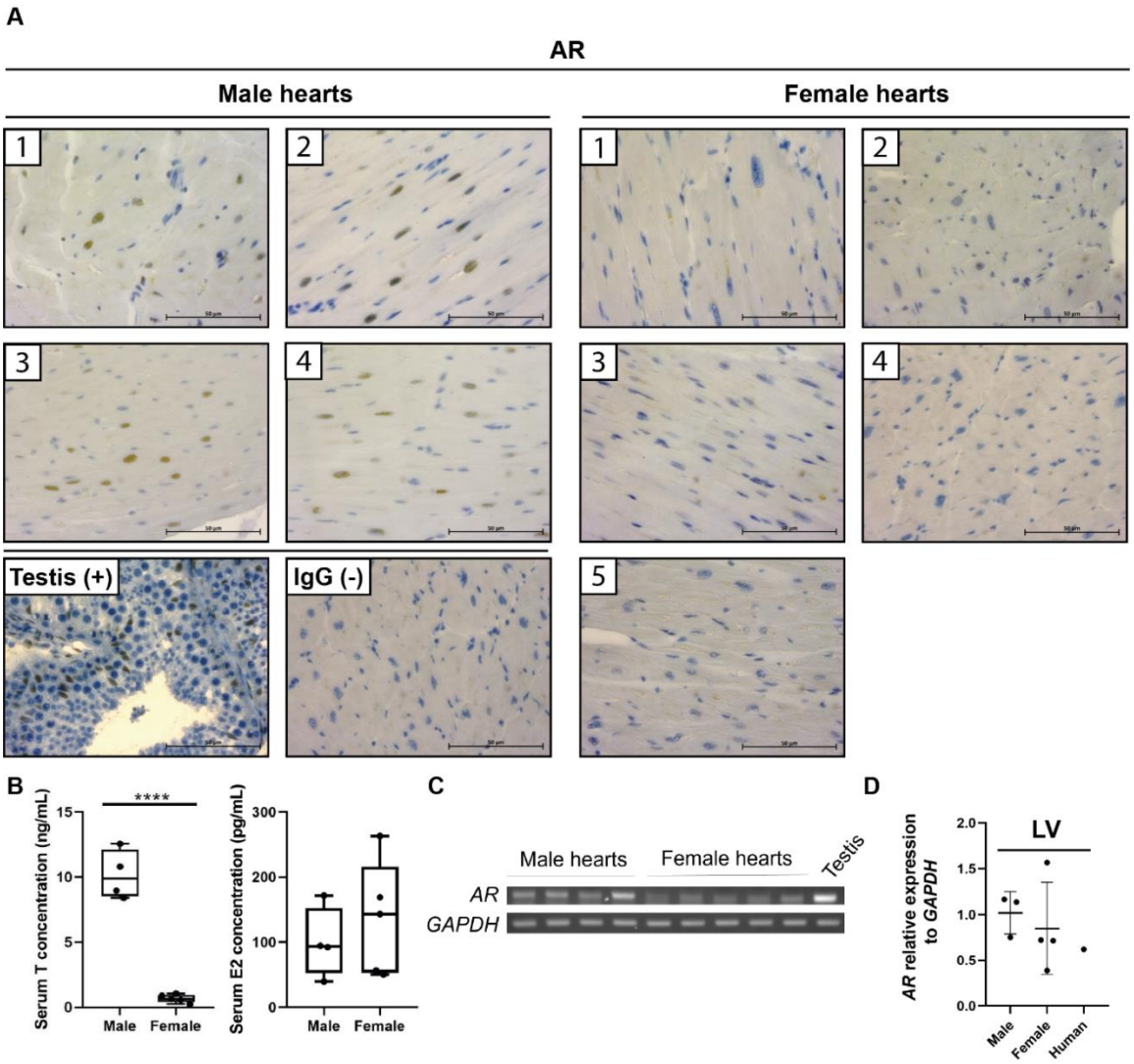

Figure 18. (A) Immunohistochemistry analysis showed AR brown staining in several nuclei of all male, but not female hearts. Testis and heart tissues stained with IgG antibodies were used as positive and negative controls respectively. Scale bars: 50 µm. **(B)** Serum T and E2 concentration were used as a control to verify normal hormone concentration in male and female subjects of each group. **(C)** PCR analysis of *AR* mRNA presence in both male and female hearts. **(D)** RT-qPCR analysis of *AR* mRNA expression in male and female rhesus and human left ventricles relative to *GAPDH*.

Despite the absence of AR signal in female hearts, Polymerase Chain Reaction (PCR) analysis unveiled the presence of *AR* messenger RNA (mRNA) in both male and female hearts (Fig. 18C). We further focused on the samples for left ventricles from different rhesus macaque monkeys to investigate the difference in *AR* mRNA expression. Quantitative Reverse Transcription-PCR (RT-qPCR) analysis indicated no difference in *AR* expression

between male and female left ventricles. This result may be attributed to high *AR* mRNA levels in one of the female heart samples (Fig. 18D). In general, the rhesus monkey *AR* mRNA expression levels are in the same range as one human control sample, that was included as a reference.

Figure 19 presents additional evidence of AR presence, displaying a mosaic pattern in cardiomyocytes across all four chambers of the heart of the male rhesus macaque. Strong signals in big and small nuclei can be detected in left and right ventricles and atria indicating its action in cardiomyocytes. Currently, it is still unknown why some heart cells possess AR while others do not. Additional studies are needed to further interrogate these findings.

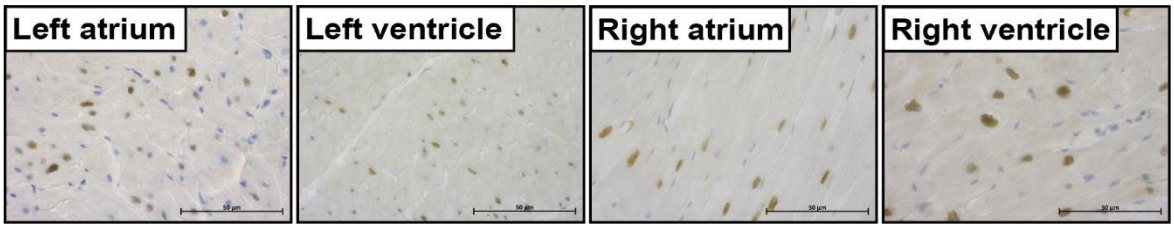

Figure 19. Immunohistochemistry analysis showed AR presence in all four chambers (left atrium, left ventricle, right atrium, right ventricle) **of rhesus macaque male heart**. Scale bars: 50 µm.

5.3 Androgen receptor in human and rhesus iPSCs.

Due to the limited information available in the existing literature, we further extended our investigation of AR to primate iPS cells (Fig. 20). According to the classical theory, upon entry to the cell, T binds to the cytosolic AR, which triggers AR translocation into the nucleus[130]. In iPSCs, however, confocal imaging showed AR presence in both cytoplasm and, unexpectedly, also nuclear compartments even with no added T (Fig. 20A). It is noteworthy that not all nuclei displayed AR, but a portion of the nuclei still showed the protein in both, male and female cell lines. Interestingly, AR was not detected in the region of nucleoli. These findings may suggest a role of the AR in the nuclear compartment of iPS cells, even when its ligand is not present.

Western blot analysis validated the existence of AR in the two human and two rhesus macaque iPSCs used in this study (Fig. 20B). While a predominant upper band was evident in all samples, a lower band, exhibiting a weaker signal was detected in male human hiPSC1 and rhesus macaque RhiPSC1 cells (Fig. 20B, asterisk). The identity of this band still needs to be elucidated, and additional experiments are needed to characterize its biological relevance.

Subsequently, comprehensive RT-qPCR analyses were conducted to assess *AR* mRNA expression levels in all four iPSCs treated and non-treated with 100 nM T for 72 hours in culture. The media was changed daily. Ultimately, no significant difference in *AR* expression was observed between the treated and non-treated cells.

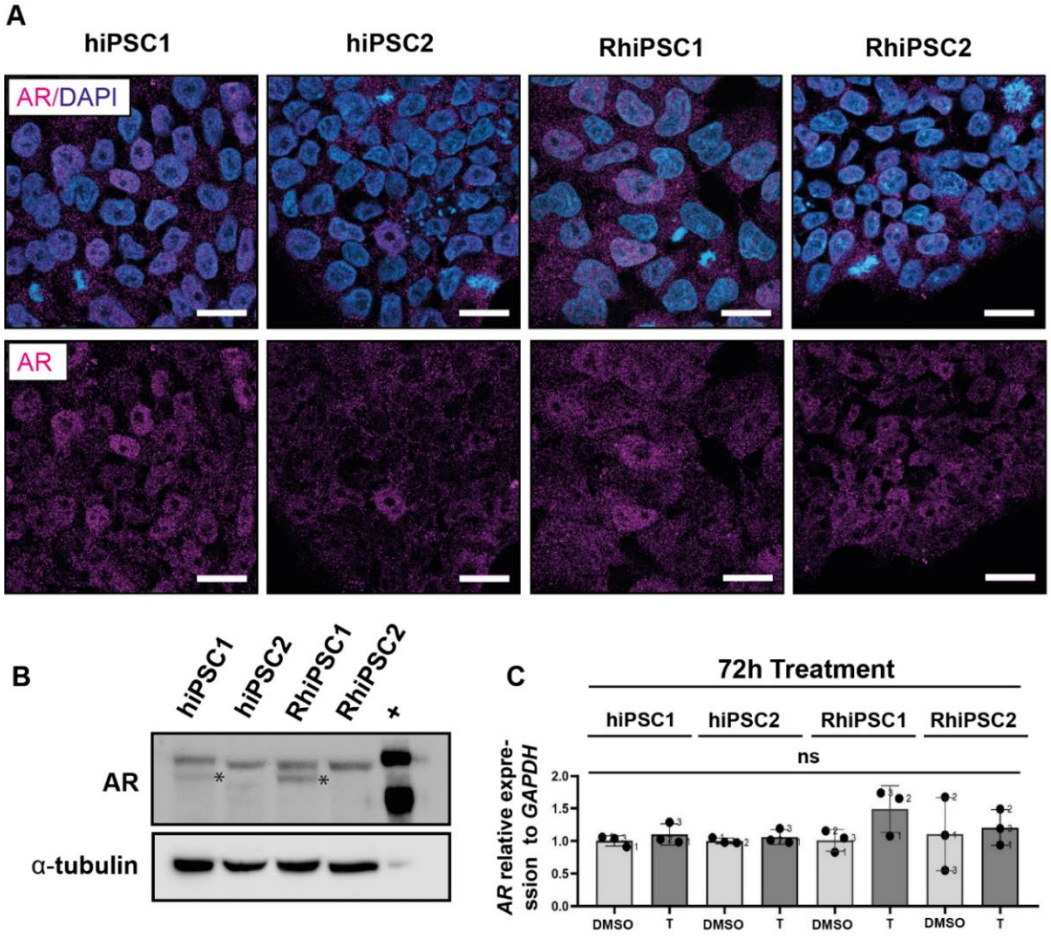

Figure 20. AR detection in iPSCs in the absence of T stimulation. (A) Immunofluorescence staining in hiPSCs and RhiPSCs shows both nuclear and cytoplasmic localization of AR (magenta). The cell nuclei were stained with DAPI. Scale bars: 20 µm. **(B)** Western blot analysis of hiPSCs and RhiPSCs detecting AR in all cell lines. The asterisk highlights a second band with a lower mass of unknown origin. 22RV1 lysate is used as a positive control. **(C)** RT-PCR analysis of *AR* mRNA expression in DMSO and 100 nM T treated iPSCs for 72 hours revealed no significant changes.

Despite no difference in mRNA levels in treated and non-treated iPS cells, we decided to investigate AR expression in male iPS cell lines using Western blot analysis and confocal imaging (Fig. 21 and 22). Protein was detected in the same manner as in rhesus hearts; however, with higher signal intensity towards the edges of the colonies in both hiPSC1 and RhiPSC1. Notably, the cytoplasmic signal remains in all three treatments and AR cannot be detected in the nucleoli.

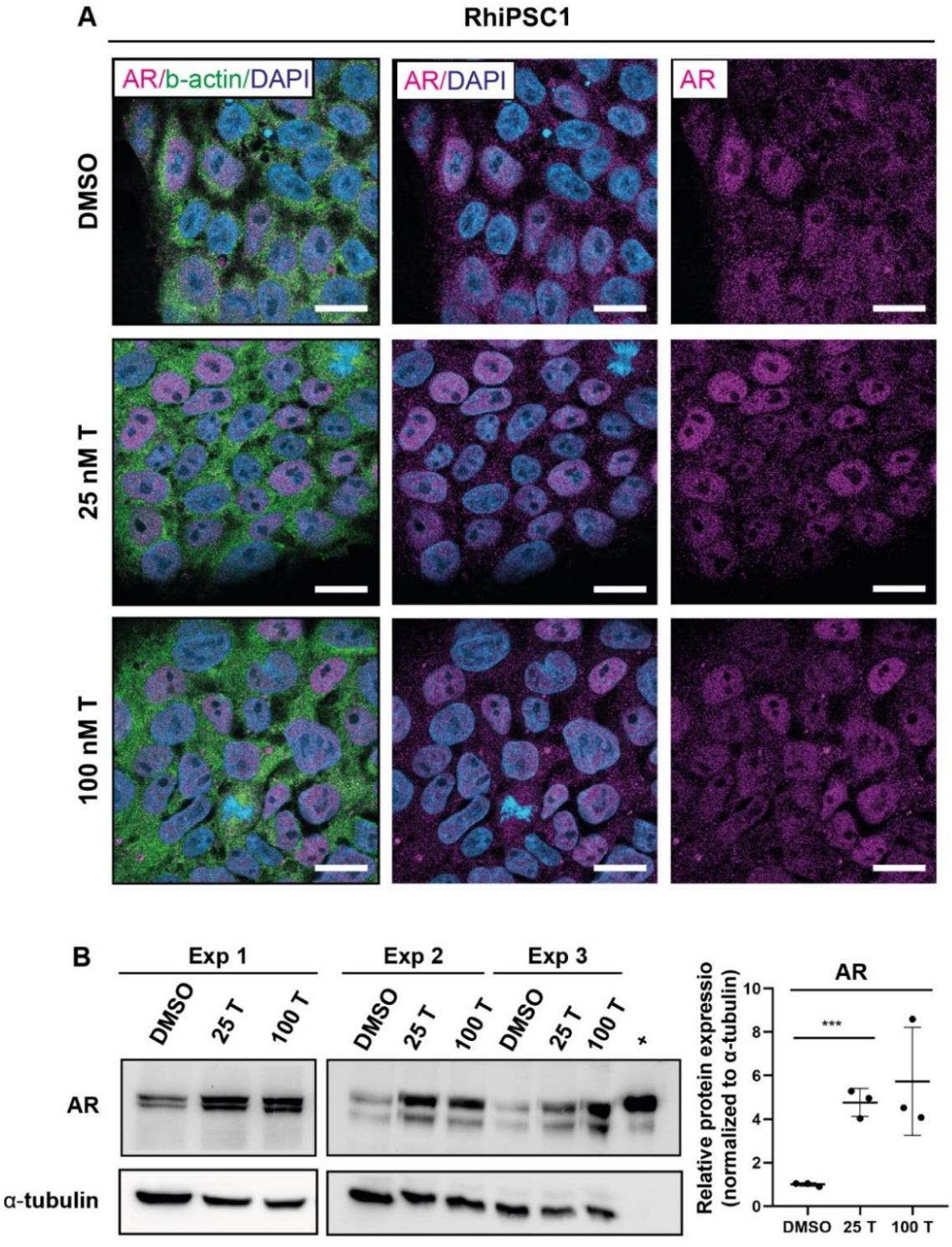

Figure 21. AR detection in Rhesus iPSCs upon T stimulation. **(A)** Immunofluorescence staining in RhiPSCs1 treated with T show a stronger AR signal in the nuclei compared to weaker staining in non-treated cells. The cell nuclei were stained with DAPI. Scale bars: 20 µm. **(B)** Western blot analysis shows an AR increase in 25 nM and 100 nM T-treated cells compared to the weaker signal in non-treated cells. 22RV1 lysate serves used as a positive control. The results of three induction experiments are shown. **(C)** Densitometry revealed a significant increase in relative AR protein expression in 25 nM T but not in 100 nM T treated cells compared to non-treated cells.

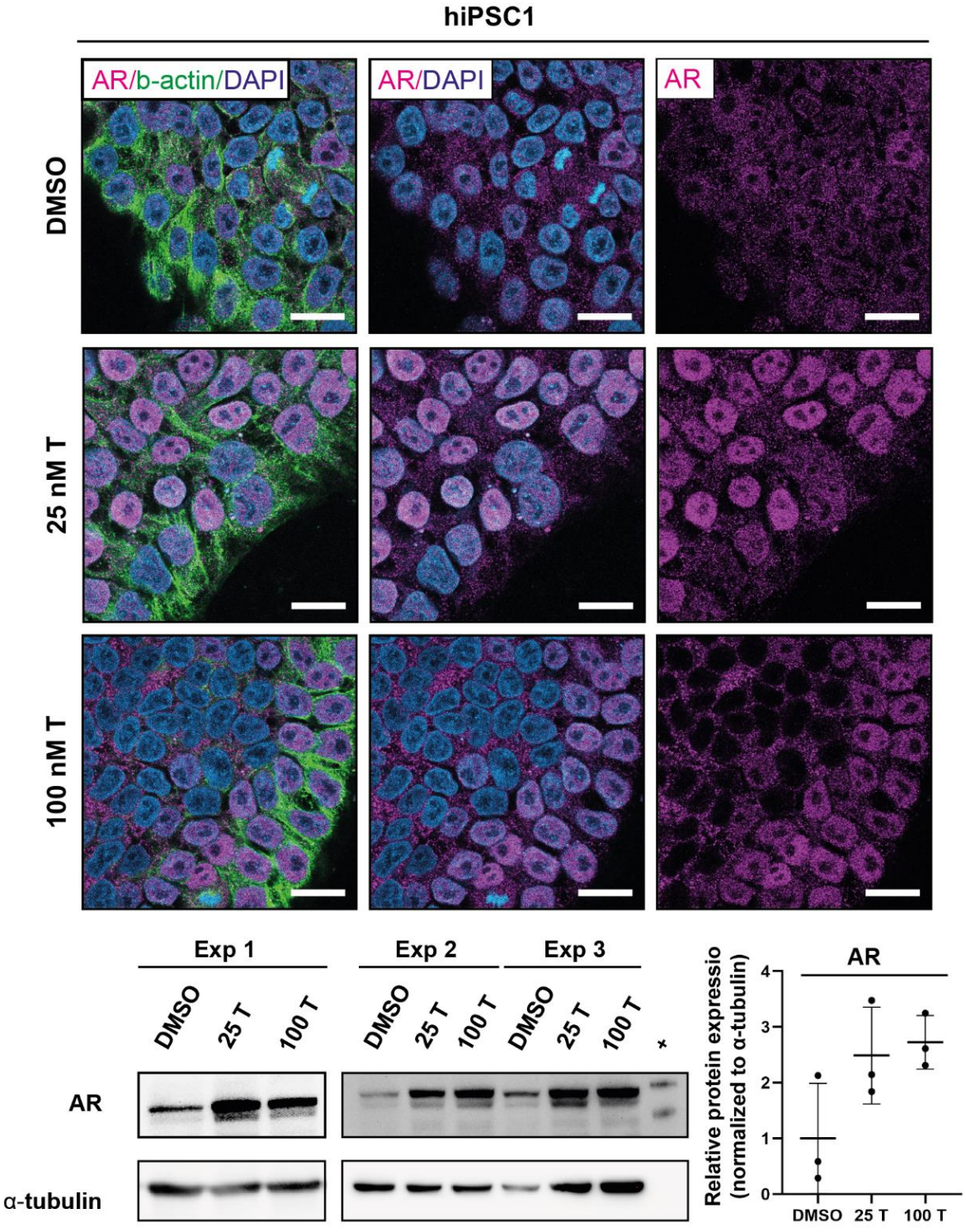

Figure 22. AR detection in human iPSCs upon T stimulation. (A) Immunofluorescence staining in hiPSCs1 treated with T shows a strong AR signal in the nuclei on the edge of the colonies compared to a rather diffuse and weaker signal in non-treated cells. The cell nuclei were stained with DAPI. Scale bars: 20 µm. **(B)** Western blot analysis shows an AR increase in 25 nM and 100 nM T-treated cells compared to a weaker signal in non-treated cells. 22RV1 lysate serves as a positive control. The results of three induction experiments are shown. **(C)** Densitometry revealed no significant differences in relative AR protein expression between all three groups.

The Induction of AR was achieved through the application of supraphysiological (100 nM) and physiological (25 nM) T treatments. Since the latter represents ~normal T levels in male serum, we focussed our investigation on male cells. Fig. 21A and 22A show an increase in AR signal in the nuclei of T-treated iPS cells compared with the non-treated cells.

Western blot analysis showed the presence of two bands of AR in all three separate induction experiments in both human and rhesus iPS cells treated and non-treated with T (Fig. 21B and 22B). These two bands were also detected in the positive control, the human prostate carcinoma epithelial cell line 22RV1. However, to our knowledge, detailed information about the difference between these two bands is still missing. Moreover, the intensity of the signal is higher in two T-treated groups compared with non-treated groups in both hiPSC1 and RhiPSC1 cells. Densitometry showed a 4.76-fold increase in AR signal intensity in 25 nM T-treated RhiPSC1 cells compared to the controls. (Fig. 21C). No significant change was detected between the groups of 100 nM T-treated and non-treated RhiPSC1 and the two T-treated and non-treated hiPSC1 cells. Additional biological replicas with more cell lines are needed to investigate in detail the trends observed in the AR expression after the treatment with T.

5.4 Androgen receptor in human and rhesus iPSC-derived cardiomyocytes

Next, an examination of AR expression in iPSC-CMs across all four cell lines was performed, as illustrated in Figure 23. Following differentiation and selection (Fig. 8), the iPSC-CMs underwent splitting and were subjected to a 7-day treatment with or without T. Confocal imaging demonstrated mostly cytoplasmic localization of AR in non-treated hiPSC1, RhiPSC1, and RhiPSC2 cells. Weak nuclear signals were detected only a few cells (Fig. 23A). Only very weak signals were detected in hiPSC2-CMs.

Validation through Western blot analysis further confirmed the presence of AR in iPSC-CMs, displaying prominent bands in RhiPSC cells and comparatively weaker bands in hiPSC1s (Fig. 23B). Minimal traces of AR signal were visible in hiPSC2 lysate.

In addition to the main signal, a band of a lower size was detected in non-treated hiPSC1-CMs (Fig. 23B, asterisk). Further experiments showed the same band in T-treated hiPSC1, but not in RhiPSC1 cells (Fig. 24 and 25).

The lower band was aligned with another band in positive control, 22RV1 cells. This cell line is known to express several AR isoforms, particularly AR-V7 isoform of that approximate size[131]. Hence, we decided to check its presence in hiPSC1-CMs using PCR (Fig. 24C). The bands of the same size as AR-V7 in 22RV1 cells were detected on the gel, although emitting a weak signal. Western blot analysis showed the presence of the same band in

100 nM T-treated hiPSC1 cardiomyocytes indicating the presence of the AR-V7 isoform. Moreover, the respective band was also detected in human left ventricle tissue (Fig.24C). To our knowledge, this is the first report of the presence of the AR-V7 isoform in human cardiomyocytes.

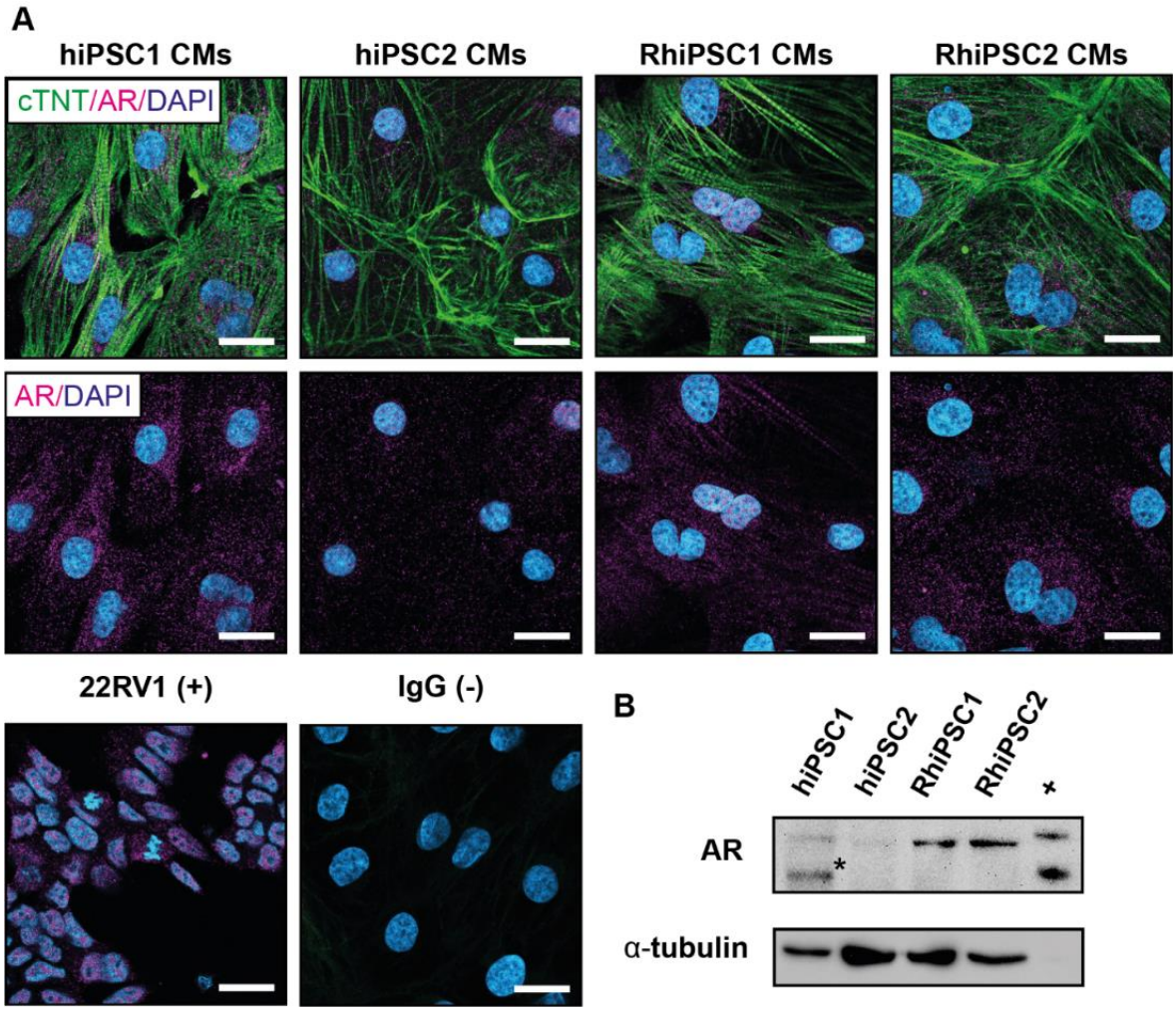

Figure 23. AR detection in iPSC-derived cardiomyocytes without T stimulation. (A) Immunofluorescence staining in hiPSC- and RhiPSC-derived cardiomyocytes (CMs) show mostly cytoplasmic localization of AR (magenta). The cell nuclei were stained with DAPI. 22RV1 cells and cardiomyocytes stained with non-specific IgG antibodies serve as positive and negative controls, respectively. Scale bars: 20 µm. **(B)** Western blot analysis showed AR presence in hiPSC1- and rhesus iPSC-derived CMs, but not in hiPSC2-CMs. The asterisk highlights an additional band of lower molecular weight in hiPSC-CMs of apparently the same size as the lower band in 22RV1 lysate. Due to the high dilution of 22RV1 cell lysate, no α-tubulin band was detected.

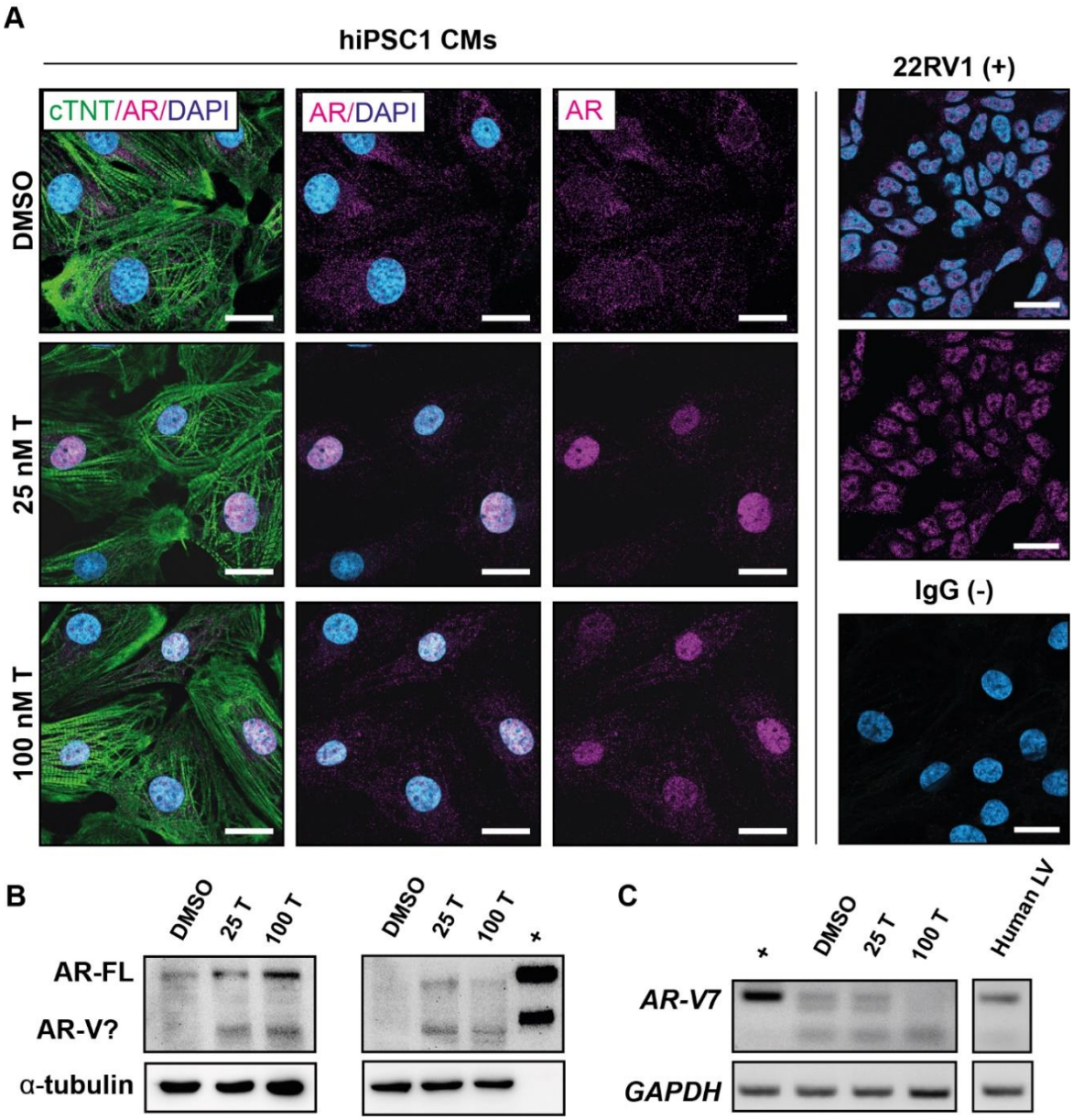

Figure 24. AR detection in human iPSC-derived cardiomyocytes upon T stimulation. **(A)** Immunofluorescence staining showed an AR signal (magenta) increase in nuclei of hiPSC1-CMs treated with 25 nM and 100 nM T compared to the DMSO control. The cell nuclei were stained with DAPI. 22RV1 cells and cardiomyocytes stained with IgG antibodies serve as positive and negative controls, respectively. Scale bars: 20 µm. **(B)** Western blot analysis revealed two bands present in two (left and right) separate experiments with hiPSC-CMs with similar size as the two bands of the positive control (22RV1 cells). The upper band indicates a canonical full-length AR and the lower band represents the V7 isoform in 22RV1 prostate cancer cells. **(C)** PCR analysis showed AR-V7 mRNA presence in 22RV1 cells (+), faint bands in treated and non-treated hiPSC-CMs, and human left ventricles.

The following analysis targeted AR presence in RhiPSC1-CMs treated and non-treated with T (Fig. 25A). Similar nuclear signal with a mosaic pattern was observed in both hiPSC1 (Fig. 24A) and RhiPSC1-CMs treated 25 nM and 100 nM T. Furthermore, there was notable variability in signal intensity among the nuclei. Western blot and densitometry analysis showed induction of AR In RhiPSC1-CMs, resulting in more than fivefold increase in 25 nM and 100 nM T-treated cells RhiPSC1-CMs in three separate experiments (Fig. 25B).

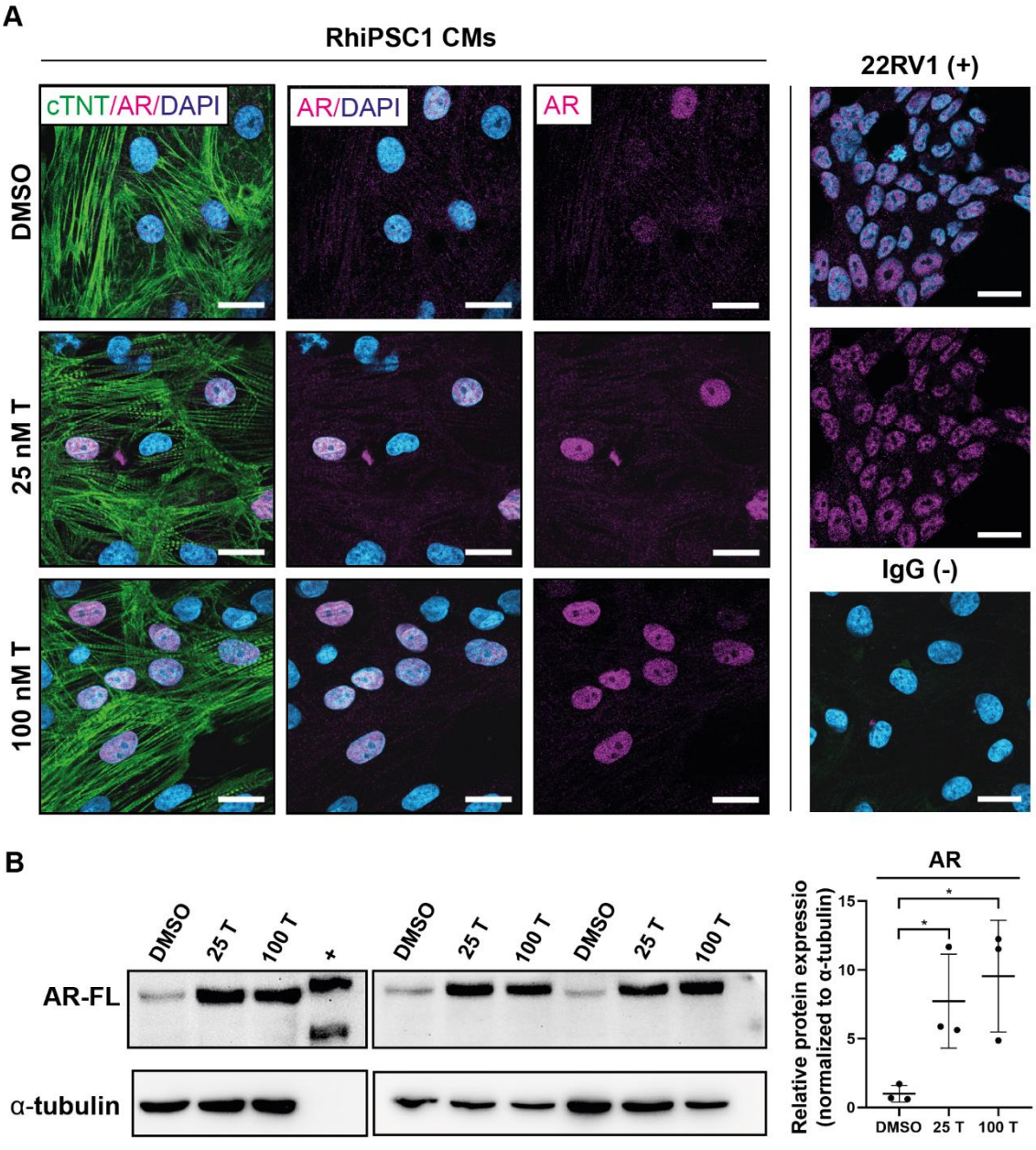

Figure 25. AR detection in rhesus iPSC-derived cardiomyocytes upon T stimulation. **(A)** Immunofluorescence staining shows AR signal (magenta) increase in nuclei of RhiPSC1-CMs treated with 25 nM and 100 nM T. The cell nuclei were stained with DAPI. 22RV1 cells and cardiomyocytes stained with IgG antibodies serve as positive and negative controls, respectively. Scale bars: 20 µm. **(B)** Western blot analysis and subsequent

densitometry revealed a significant increase in AR signal in 25 nM and 100 nM T-treated RhiPSC-CMs compared with non-treated cells.

5.5 Testosterone effect on sarcomeric properties of RhiPSC1-derived cardiomyocytes

To investigate the effects of T on RhiPSC1-CMs we analyzed cytoskeletal properties (Fig. 26). Sarcomeres, the contractile units of muscle cells, are essential cell compartments that reflect the contraction properties of cardiomyocytes. SotaTool, free software with minimal user bias, was used to analyze sarcomeric properties[118].

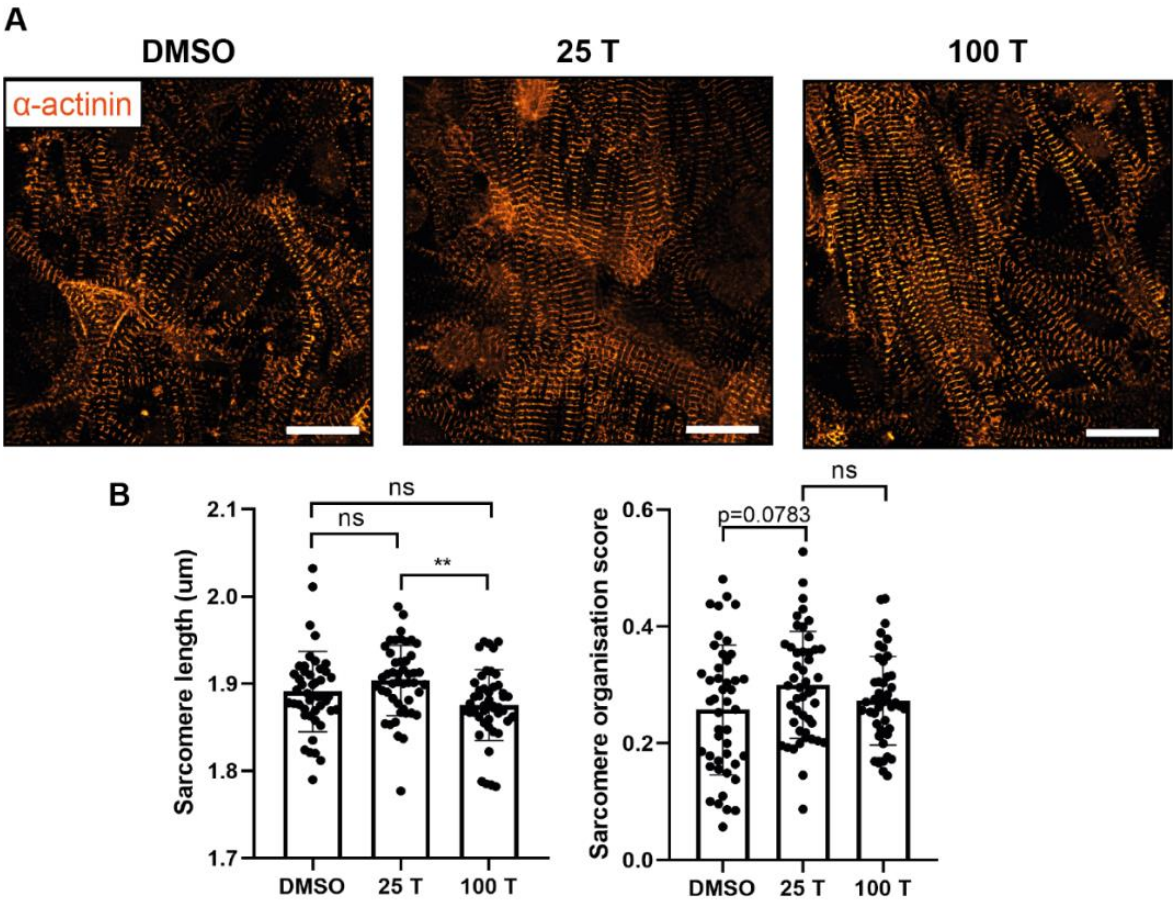

Figure 26. Sarcomere length and organization. (A) Immunofluorescence staining showed sarcomere protein α-actinin in RhiPSC-CMs treated and non-treated with T, which was used for sarcomere analysis. Scale bar: 20 µm. **(B)** Sarcomere analysis revealed significant changes in sarcomere length in 25 nM T-treated cells compared with 100 nM T-treated cells. A trend toward higher sarcomere organization score was detected in 25 nM T-treated cells compared with non-treated cells.

The results revealed no significant difference in sarcomere length of cells from the two T-treated groups compared with non-treated RhiPSC1-CMs. However, a significant reduction of sarcomere length was detected in 100 nM T-treated cells compared with 25 nM T-treated cells from 1.904 ± 0.04 to 1.875 ± 0.04 μm. This suggests different effects of physiological and supraphysiological concentrations of T on RhiPSC1-CMs. Another parameter reflecting the organization of sarcomeres, sarcomere organization score (SOS)[118], was explored in RhiPSC1-derived cells. Only a trend (p=0.0783) was detected in 25 nm T-treated RhiPSC1 cells compared with the non-treated group with 0.257 ± 0.11 in non-treated cells and 0.3 ± 0.09 in 25 nM T-treated cells. No significant changes in SOS were detected between other groups.

5.6 Generation of AR KO hiPSC1 cell line

To further investigate the effects of T, which can affect cardiomyocytes through both AR-dependent and independent pathways, we created an androgen receptor knockout (KO) cell line (Fig. 27).

We employed the piggyBac transposon system in conjunction with CRISPR/Cas9 to introduce mutations into the Androgen Receptor (AR) situated on the X chromosome, as described previously[124]. Cas9, fused with GFP, facilitated the visualization of transfected cells through fluorescence microscopy 48 hours after the lipofection delivery of plasmids (Fig. 27A). Next, the cells underwent a single passage and were sorted at one GFP-positive cell/well followed by further culture propagation (Fig. 27B). Upon genomic DNA extraction and AR fragment amplification, Sanger sequencing was conducted to identify mutated clones. One of the monoclonal cell lines exhibited 5-nt insertion disrupting the AR open reading frame (Fig. 27C).

Single-cell sorting of stem cells may lead to spontaneous differentiation to other cell types. Immunofluorescence imaging of pluripotency markers was used to evaluate that possibility (Fig. 28). No evident changes were detected in the expression and localization of SALL4, NANOG, LIIN28A, and OCT4A between hiPSC1 WT and KO cells.

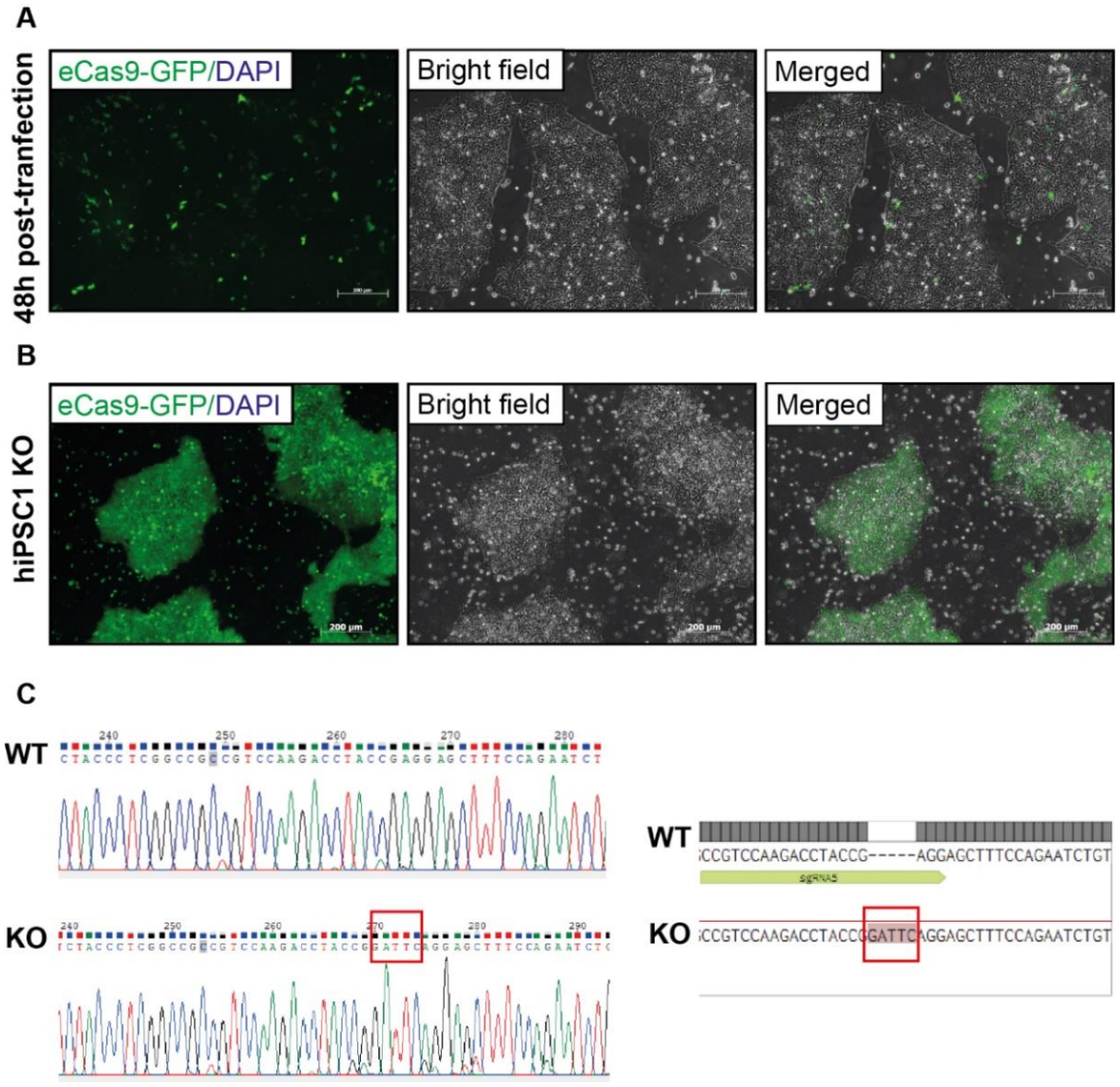

Figure 27. Generation of *AR* KO hiPSC1 cell lines. (A) Immunofluorescence microscopy of hiPSC1 48h after transfection with pTT-PB_eCas9_GFP_sgRNA5 to mutate *AR* showed a positive signal from eCas9-GFP in transfected cells. Scale bars: 200 µm. **(B)** Fluorescence microscopy of hiPSC1_AR_KO_cl9 after sorting and clonal cell line expansion displayed a strong endogenous eCas9-GFP signal in all cells of the colonies. Scale bars: 200 µm. **(C)** Mutation analysis of monoclonal cell lines by PCR amplification of the *AR* locus coding for the N-terminal portion of the AR and Sanger sequencing. The left figure shows the sequencing of Wild-type (WT) and knock-out (KO) monoclonal cell lines used further in the study. The red box highlights a 5-nt insertion in the mutated clone. The right figure shows a schematic representation of WT and KO sequences obtained from chromatograms and aligned one to another with the binding site of the sgRNA5 sequence highlighted in green.

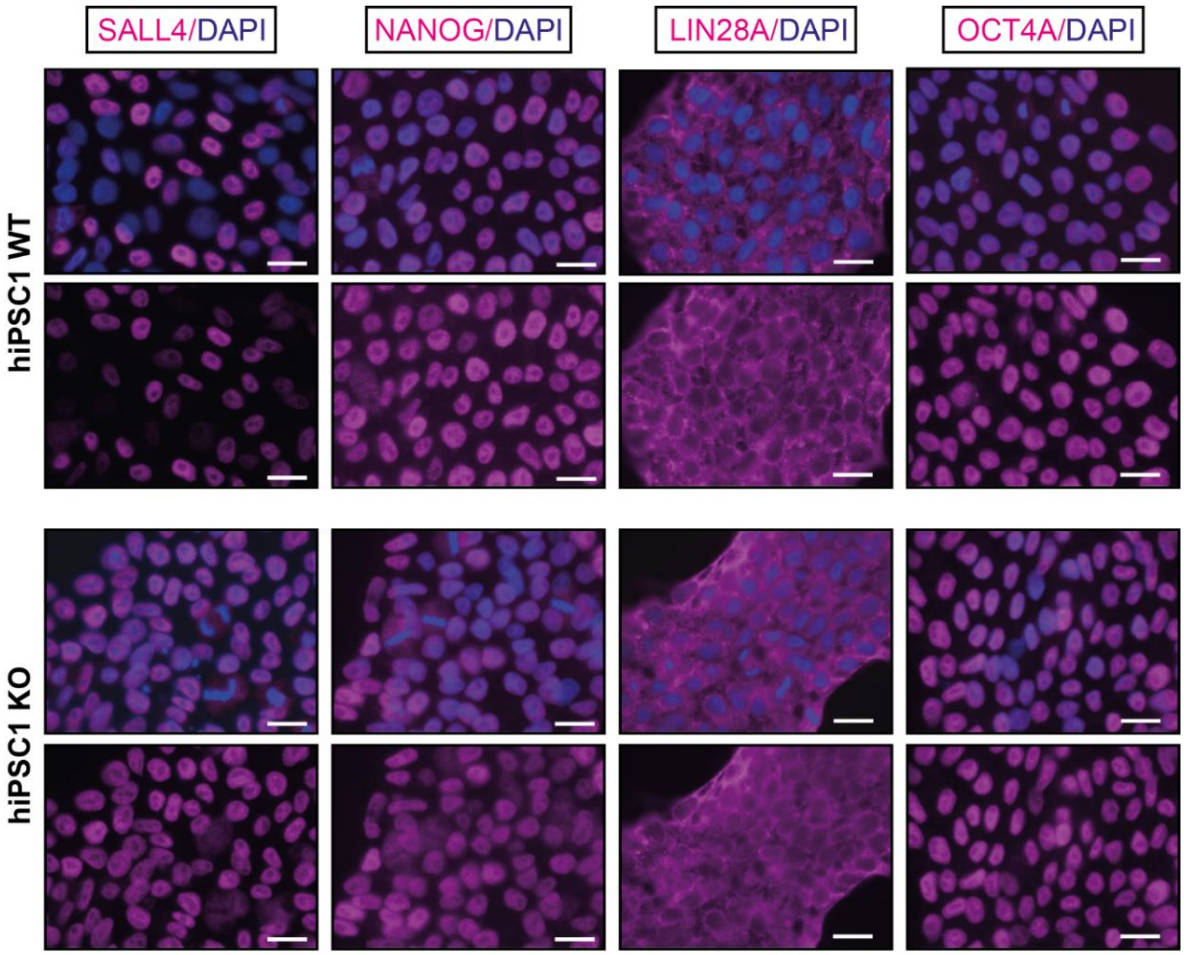

Figure 28. Characterization of the AR KO iPSC line. Immunofluorescence staining of hiPSC1 WT and *AR* KO cell lines detected the pluripotency transcription factor markers NANOG, OCT4A, SALL4, and cytoplasmic marker LIN28A. The cell nuclei were stained with DAPI. Scale bars: 20 μm.

Subsequently, WT and KO cells were exposed to T to verify the absence of AR in hiPSC1 KO cell line (Fig. 29). Immunofluorescence imaging revealed no AR signal in the colonies of both treated and non-treated hiPSC1 KO cells (Fig. 29A). The absence of AR was further confirmed through Western Blot analysis in hiPSC1 KO cell lines in comparison with hiPSC1 WT cells (Fig. 29B). Additionally, all four pluripotency markers were present in T-treated and non-treated hiPSC1 WT and KO cell lines (Fig. 29C).

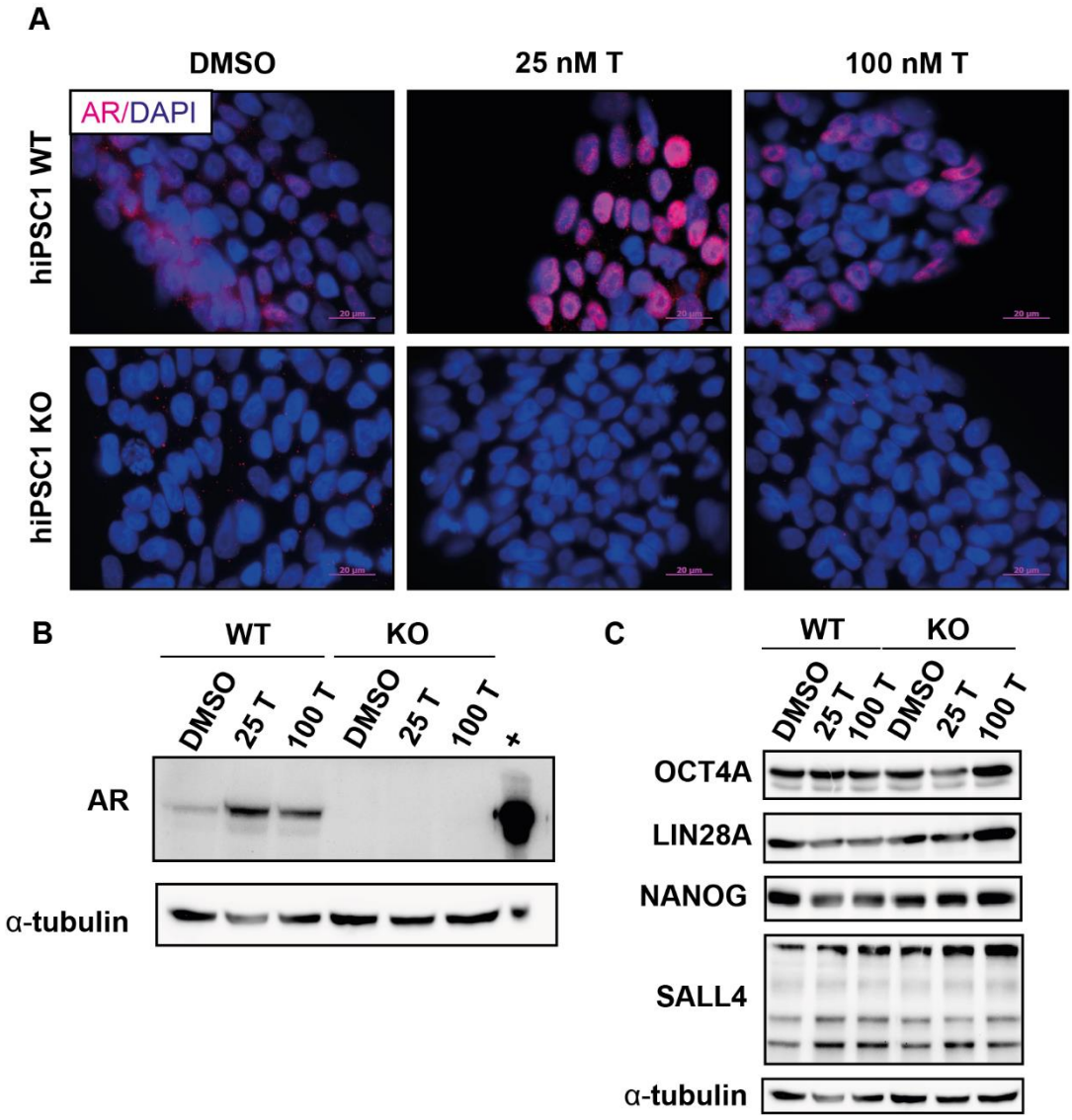

Figure 29. T treatment of hiPSC1 WT and hiPSC1 KO cell lines. Immunofluorescence staining **(A)** and Western blot analysis **(B)** revealed AR presence (magenta in A) in all three treatment groups of hiPSC1 WT cells and no signal in hiPSC1 KO cell lines. **(A)** The cell nuclei were stained with DAPI. Scale bars: 20 µm. **(B)** 22RV1 lysate was used as a positive control. **(C)** Western blot analysis demonstrated the presence of four pluripotency markers in T-treated and non-treated hiPSC1 WT and hiPSC1 KO cell lines.

5.7 Cardiac differentiation of hiPSC1 AR KO cells

Following the characterization and confirmation of AR absence in the KO cell line, the subsequent step involved the differentiation of the respective iPSC lines to cardiomyocytes. Given the inherent high heterogeneity of cardiac differentiation, we conducted the experiment with the same range of cell seeding numbers for hiPSC1 KO cells as was done previously in hiPSC1 WT cells (Fig. 30A).

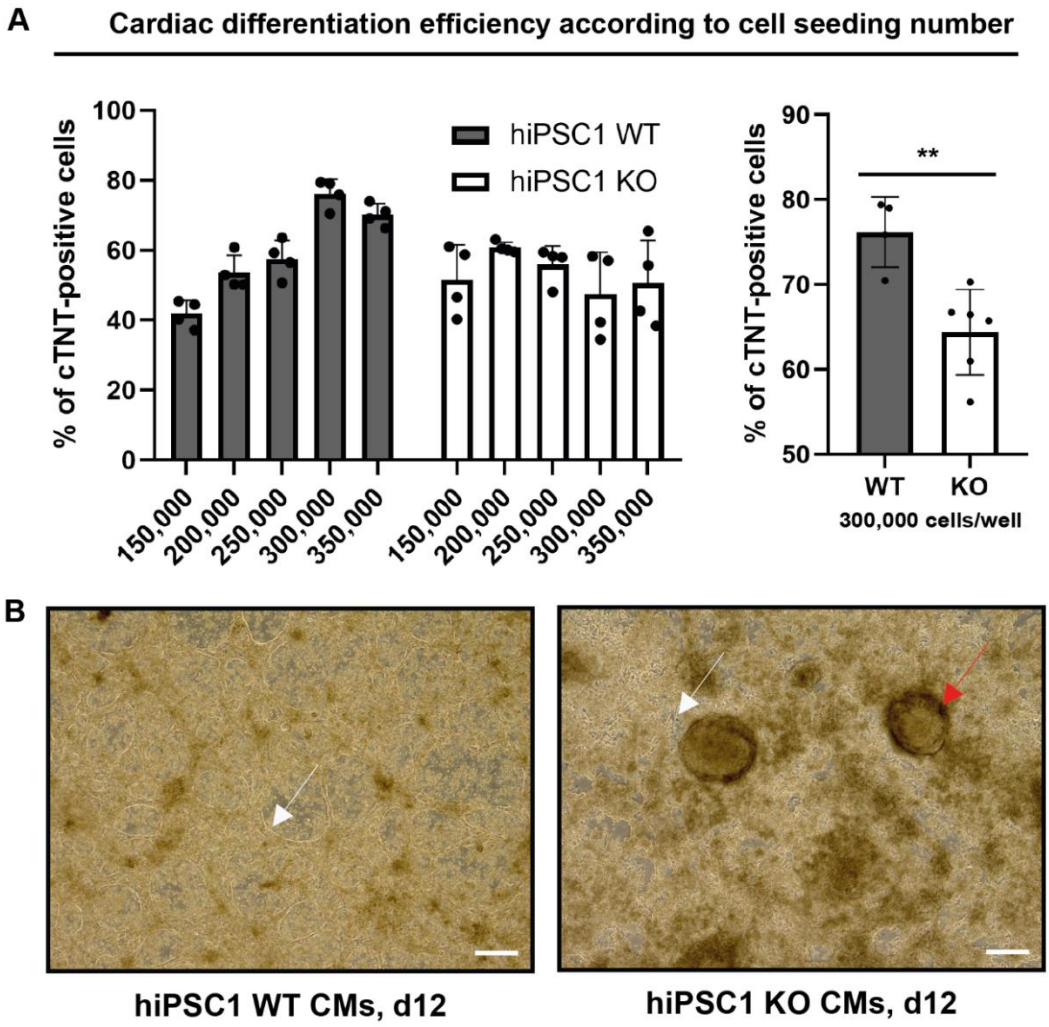

Figure 30. Cardiac differentiation of hiPSC1 WT and hiPSC1 KO cell lines. (A) hiPSC1 KO cells were seeded in the same numbers as in previous experiments in hiPSC1 WT cell lines. The right graph shows repeated experiments with 300,000 cells/well seeding of hiPSC1 KO. **(B)** Representative pictures of cardiomyocytes on day 12 since the beginning of differentiation generated from hiPSC1 WT and KO cell lines seeded at 300,000 cells/well. hiPSC1 WT CMs exhibited characteristic net-like structures, whereas KO cells generated additional non-beating roundish structures of unknown composition. Scale bars: 100 µm.

In contrast to hiPSC1 WT cells, none of the cell seeding numbers yielded more than 70% of cardiomyocytes. Repeated measurement of 300,000 cells/well (the condition that resulted in the maximum number of cardiomyocytes in WT) resulted only in 64.38 ± 5.02% cTNT-positive hiPSC1 KO cells. This signifies an almost 10% reduction in generated cardiomyocytes and hence a smaller volume of cardiac cells for further analysis.

Subsequently, the cells were selected, split, and further examined for cardiac markers (Fig. 31). Upon closer inspection, hiPSC1 KO compared with WT cells revealed a less organized cytoskeletal structure, although with preserved sarcomeres. Key cardiac markers like

MLC2a, MLC2v, α-actinin, and cardiac troponin T (cTNT) were all present in hiPSC1 KO. Additionally, the Cx43 signal was detected in the cell-cell contacts of cardiomyocytes.

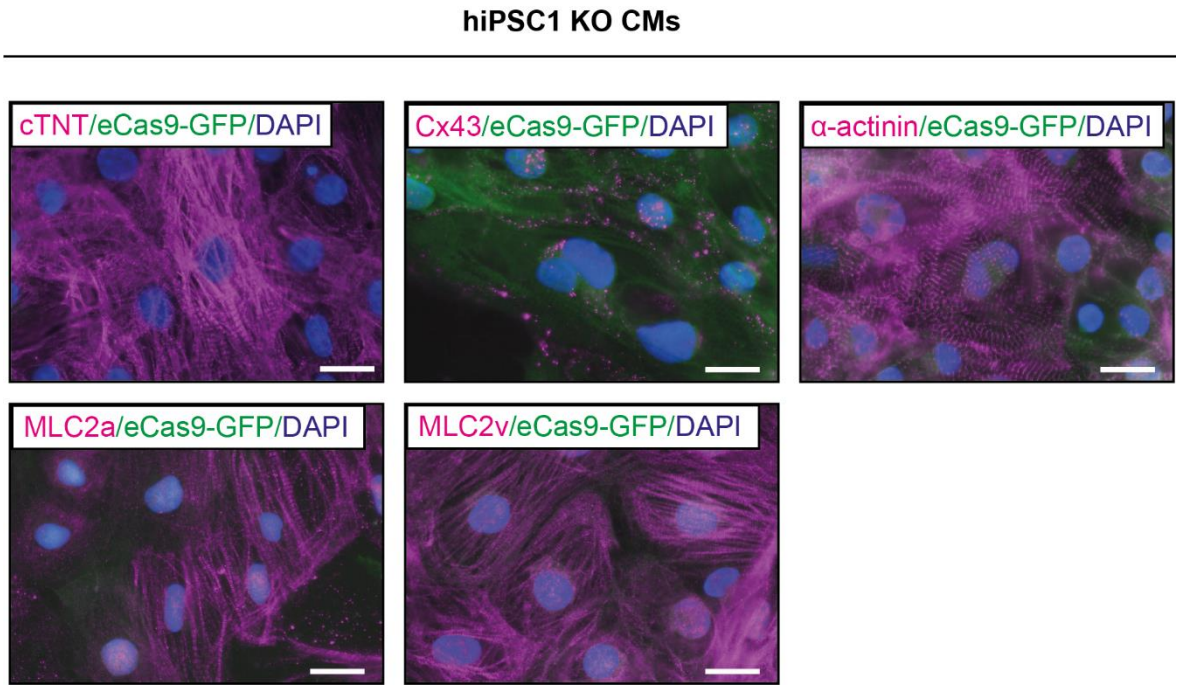

Figure 31. Immunofluorescence staining in hiPSC1 KO CMs of cardiac-specific markers such as myosin light chain 2 ventricular (MLC2v), myosin light chain 2 atrial (MLC2a), α-actinin, cardiac troponin T (cTNT) and connexin 43 (Cx43). Fluorescence pictures show typical structure and morphology of iPSC-CMs forming striated patterns of sarcomeres. eCas9-GFP signal is observable in green. The cell nuclei were stained with DAPI. Scale bars: 20 µm.

5.8 Effect of testosterone on cellular properties of hiPSC1 WT and KO derived cardiomyocytes.

To assess the effects of T in human cardiomyocytes, we conducted a series of further experiments. Based on previous culture observations, higher numbers (densities) of cardiomyocytes in culture lead to more disorganized cardiomyocyte cell-cell connections and sarcomeres. To test if proliferation levels are affected, EdU treatment was administered for 48 hours according to both treated and non-treated hIPSC1 WT and KO cardiomyocytes (Fig. 32).

We did not observe a difference between the T-treated and non-treated groups, both in hiPSC1 WT and KO cells. Thus, T did not affect the proliferation rates of the cell lines in this experiment. Notably, however, the proliferation rate of hiPSC1 KO cells was significantly higher in all three groups compared to all three groups of WT cells. In the non-treated group

of the hiPSC1 KO line, 76.82 ± 5.14% of cells were EdU positive, while in the non-treated group of hiPSC1 WT, only 62.37 ± 4.63% of cells were EdU positive cells.

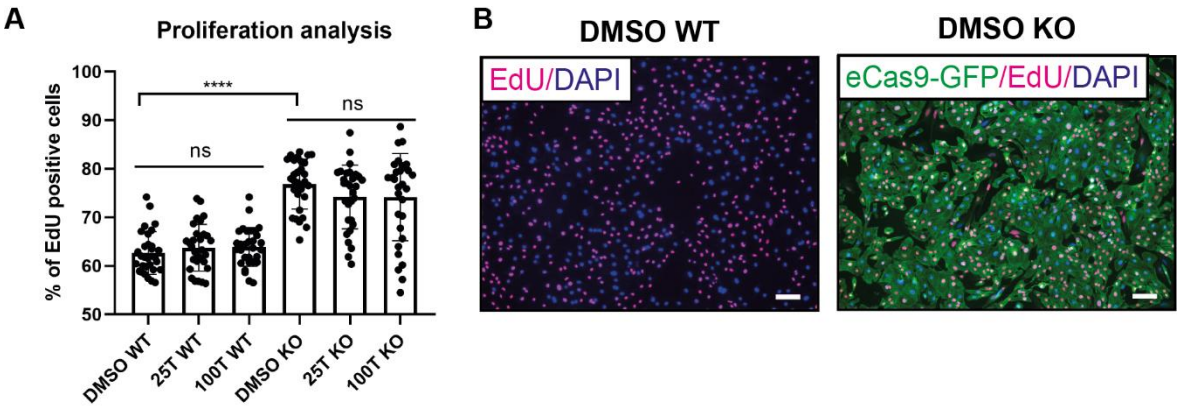

Figure 32. Proliferation analysis of hiPSC1 WT and KO CMs using EdU incorporation in cells in the presence and absence of T. (A) We observed a significant difference between the proliferation rates of hiPSC1 WT and KO cell lines irrespective of the presence or absence of T (n=3 separate differentiation experiments). Scale bars: 100 µm.

Based on the aberrantly organized cytoskeletal structure shown in Figure 31, we further analyzed sarcomere parameters of hiPSC1 WT and KO cell lines in the presence and absence of T (Fig. 33). Only 25 nM T exposure resulted in a significant increase in sarcomere length of hiPSC1 WT cardiomyocytes compared with non-treated cells. While non-treated cells displayed 1.915 ± 0.05 µm long sarcomeres, 25 nM T-treated cells reached lengths of 1.945 ± 0.06 µm. The same trend was spotted in 100 nM T-treated hiPSC1 WT cells with the p=0.0739. More experiments need to be done to explore the effect of a supraphysiological T concentration. Notably, no significant differences were detected in the sarcomere length of T-treated or non-treated hiPSC1 KO cells.

While the sarcomeres of hiPSC1 KO cells were significantly longer than those of hiPSC1 WT cells, the SOS exhibited a significant decrease in KO cells. The SOS of non-treated hiPSC1 WT cells reached 0.2975 ± 0.088, whereas in non-treated hiPSC1 KO cells, the SOS was only 0.1686 ± 0.077. Consequently, the SOS parameter experienced an almost two-fold decrease in hiPSC1 KO cells, reflecting the more disorganized sarcomeres visualized using immunofluorescence staining (Fig. 33A). In summary, the sarcomeres in KO cells are longer, but less organized. Notably, none of the treatments led to a significant increase of SOS in hiPSC1 WT cells. Only 100 nM T treatment resulted in a significant increase of SOS in the KO cells compared with 25 nM T-treated group, and the same trend was detected in comparison with non-treated groups. The SOS in 100 nM T hiPSC1 KO cells reached 0.2034 ± 0.079. However, it still did not match the SOS of any of the groups

in hiPSC1 WT cells. This experiment highlights that AR KO cells exhibited inferior sarcomere organization.

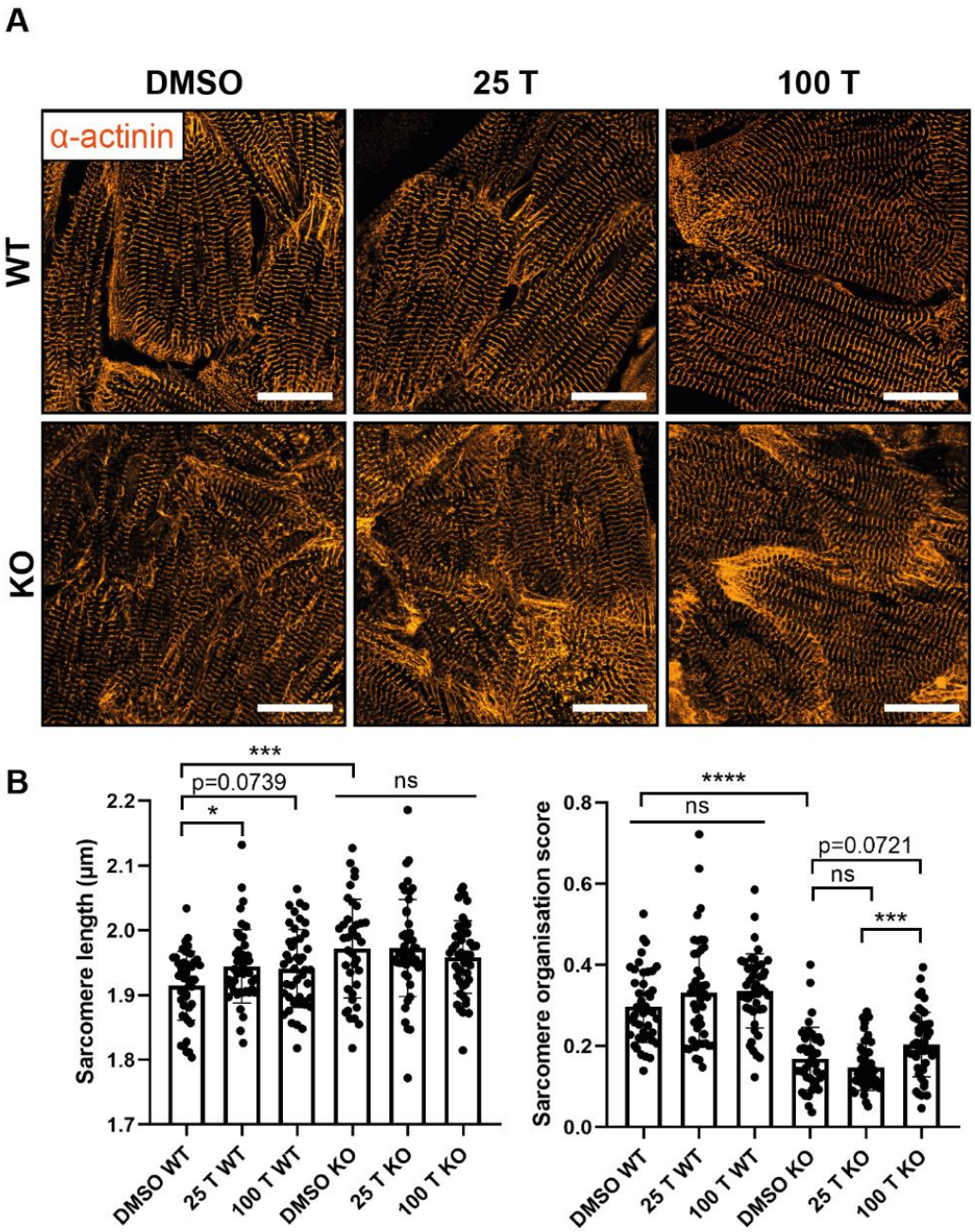

Figure 33. Sarcomere analysis in hiPSC1 WT and KO CMs. (A) Representative fluorescence staining of sarcomere protein α-actinin in cardiomyocytes in the presence and absence of T. Scale bars: 20 µm. **(B)** Sarcomere analysis revealed a significant increase in sarcomere length in 25 nM T, and a corresponding trend in 100 nM T-treated hiPSC1 WT cardiomyocytes compared with non-treated cells (n=3). The sarcomere organization score (SOS) in hiPSC1 KO non-treated CMs was significantly smaller than in non-treated hiPSC WT cells (n=3 separate differentiation experiments). 100 nM T treatment significantly increased SOS in hiPSC1 KO compared 25 nM T group, and the same trend was detected in comparison with the non-treated group.

Given the observed impact of T on sarcomere properties, we proceeded to examine the characteristics of Ca^{2+}. This ion plays a crucial role in muscle contraction, and its current density was assessed (collaboration with Rohan Kapoor and Prof. Tobias Moser, MPI-NAT). Patch-clamp analysis revealed a significant decrease in Ca^{2+} current density in 100 nm T treated hiPSC1 WT cells compared with non-treated and 25 nM T treated cells for 24 h (Fig. 34). However, a 48-hour treatment did not result in any significant changes between all three groups. Future experiments are needed to further investigate Ca^{2+} current densities in hiPSC1 KO cell lines under the effect of T.

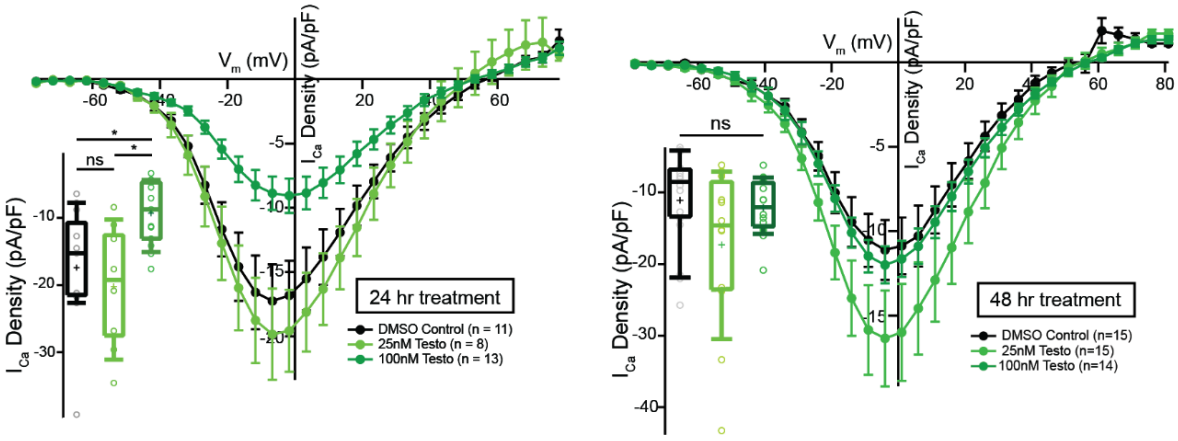

Figure 34. Electrophysiological characterization. Cardiac whole-cell L-type Ca^{2+} current densities in WT hiPSC1-CMs treated and non-treated with T for 24 h (left graph) and 48 h (right graph). 100 nM T decreased the Ca^{2+} current density in hiPSC1 WT CMs treated for 24 h compared with non-treated and 25 nM T-treated cells. 48h treatment revealed no significant changes between all three groups of hiPSC1-CMs.

5.9 Gene expression profiles of hiPSC1 WT and KO-derived cardiomyocytes

Based on the differences found in proliferation and sarcomere parameters of WT and KO DMSO cells, we conducted total RNA sequencing. Two independent experiments were used for each experimental group. Subsequent volcano plots and heat maps for 50 upregulated and 50 downregulated genes were created (Fig. 35 and 36).

The analysis showed several groups of genes affected between the two groups. A negative change in KO cells was detected in expression levels of Sarcoglycan alpha (*SGCG*), Myosin heavy chain 6 (*MYH6*), Glucose transporter type 4 (*GLUT4*), Insulin-like growth factor 2 (*IGF2*), and Calcium/calmodulin-dependent protein kinase II beta (*CAMK2B*) – genes important for sarcomere development and cardiac hypertrophy. This is also strengthened by less expression of potassium channel subunits and interacting proteins represented by Potassium voltage-gated channel interacting protein (*KCNIP*), Potassium voltage-gated

channel subfamily C member 3 (KCNC3), and Hyperpolarization-activated cyclic nucleotide-gated potassium channel 2 (*HCN2*).

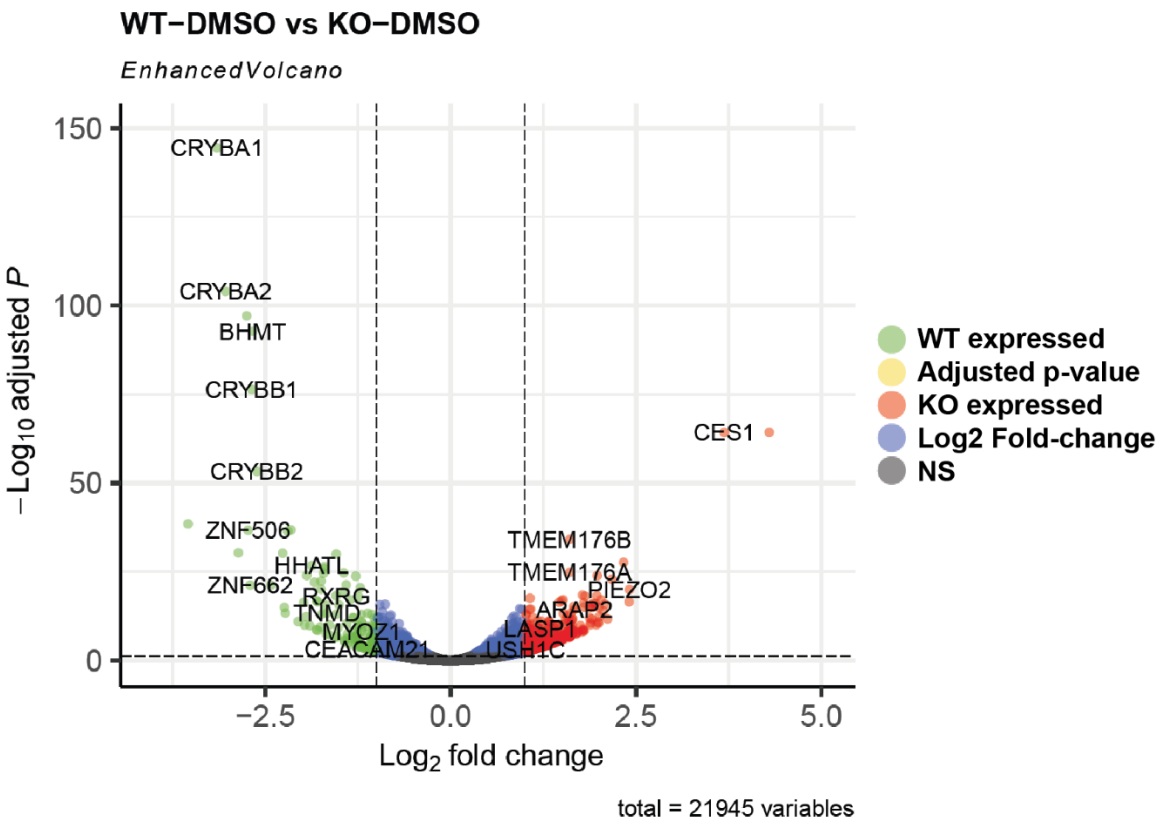

Figure 35. Volcano plot of 21945 genes identified by total RNA-sequencing of WT iPSC-CMs and AR KO iPSC-CMs. The volcano plot shows the fold change (x-axis) versus the significance (y-axis) of the identified values. The significance (non-adjusted p-value) and the fold-change are converted to −Log10(p-value) and Log2(fold-change), respectively. The vertical and horizontal dotted lines show the cut-off of fold-change = ± 1 and of p-value = 0.05, respectively. 337 genes increased by ≥ 1-fold and 133 genes decreased by ≤-1-fold with p-values <0.05.

Other families like crystallin proteins (Crystallin beta B1 (*CRYBB1*), Crystallin beta A4 (*CRYBA4*), Crystallin beta A1 (*CRYBA1*), Crystallin beta B2 (*CRYBB2*), Crystallin alpha A (*CRYAA*), Crystallin beta B3 (*CRYBB3*), Crystallin beta A2 (*CRYBA2*), Crystallin gamma S (*CRYGS*), Crystallin gamma C (*CRYGC*), Crystallin gamma D (*CRYGD*) and proteins involved in the retinoid pathway (Retinoid X receptor gamma (*RXRG*), Stimulated by retinoic acid 6 (*STRA6*) were also decreased in KO cells. Additionally, multiple DNA-binding transcription factors represented by Zinc finger protein 506 (*ZNF506*), Zinc finger protein 662 (*ZNF662*), Zinc finger protein 558 (*ZNF558*), Zinc finger protein 69 (ZNF69), and others were downregulated in KO cells.

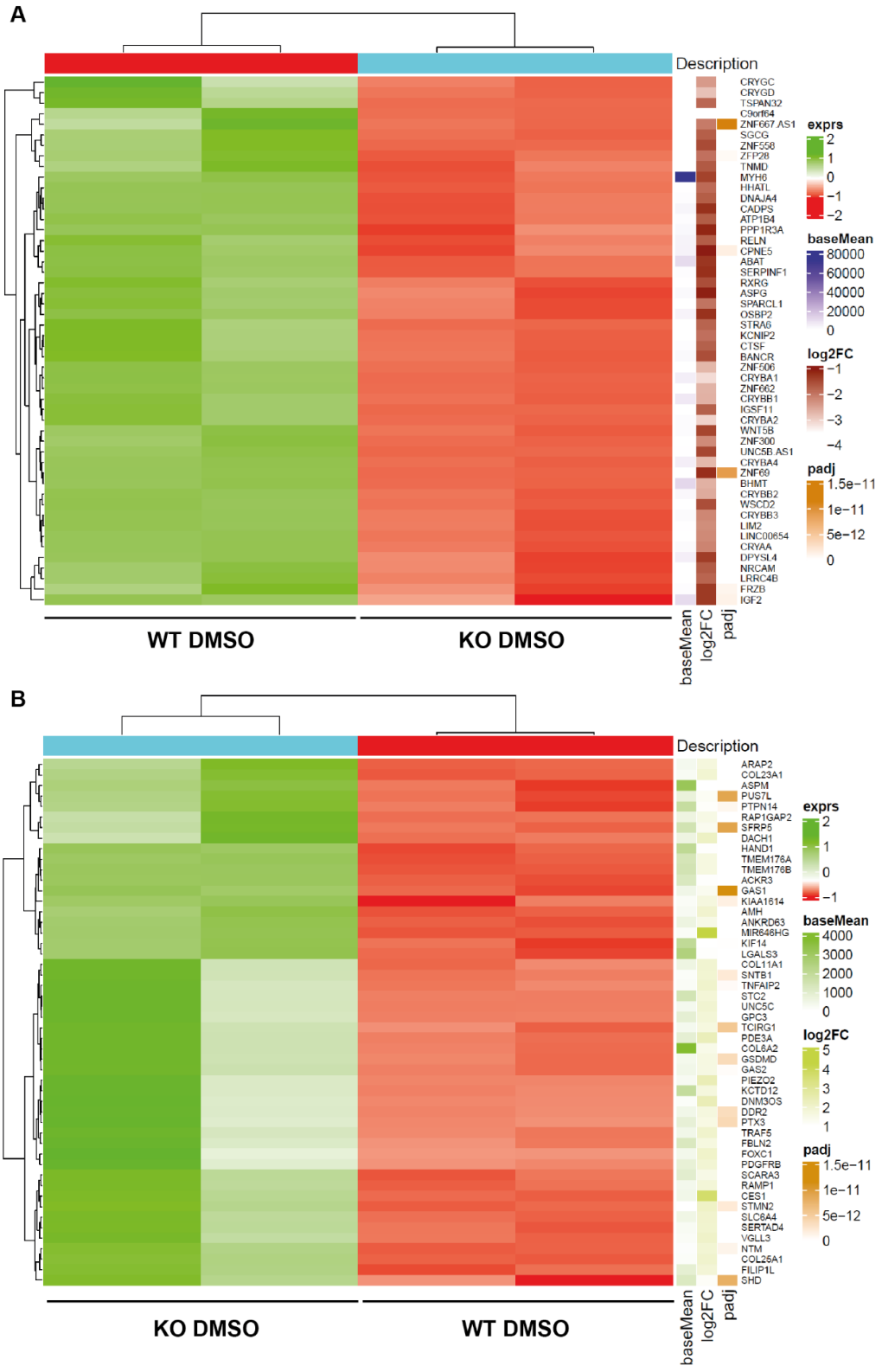

Figure 36. Heat-map of top 50 downregulated (A) and upregulated (B) genes in AR KO CMs compared with WT CMs from two independent experiments each. The main heatmap shows normalized read counts per sample, and three heatmaps on the right show average gene expression across all samples (baseMean), log2 fold-changes, and adjusted p-values (padj). Genes and samples were clustered based on euclidean distance.

Other gene groups involved in blood vessel development and early cardiovascular development were upregulated in KO cells compared to WT cells. Vasculature factors Angiopoietin-1 (*ANGPT1*), Myosin-11 (*MYH11*), Mitogen-activated protein kinase 11 (*MAPK11*), and GATA-binding protein 2 (*GATA2*) levels increased in KO cells. Moreover, KO cells contained increased expression of Heart- and neural crest derivatives-expressed protein 1 (*HAND1*), a regulator of early cardiac development. The inductor of proliferation in cardiomyocytes, Carboxylesterase 1 (*CES1*), levels were upregulated. Notably, multiple collagen chains Collagen alpha-XI chain 1 (*COL11A1*), Collagen alpha-IX chain 3 (*COL9A3*), Collagen alpha-I chain 1 (*COL1A1*), Collagen alpha-XII chain 1 (*COL12A1*), Collagen alpha-VI chain 2 (*COL6A2*), Collagen alpha-VI chain 3 (*COL6A3*), and Collagen alpha-I chain 2 (*COL1A2*) as well as Fibrillin-1 (*FBN1*) levels also increased. Various factors involved in extracellular matrix, cell adhesion, neuronal development, and others were also affected (Supplementary data).

5.10 Androgen-converting enzymes in primate cardiomyocytes

A global analysis of the conducted experiments showed that often no clear dose-dependent effect of T was found. Thereby we hypothesised that T may undergo metabolic conversion by cardiomyocytes. To investigate this possibility, we examined the gene expression profiles of two main T-converting enzymes: aromatase and 5α-reductase (Fig. 37).

Shortly, aromatase catalyzes the conversion of T to estradiol, whereas 5α-reductase transforms T to its more potent derivative, DHT. Aromatase, encoded by the gene *CYP19A1*, is expressed in one protein isoform. In contrast, three 5α-reductase isozymes, named type 1, 2, and 3 (SRD5A1, SRD5A2, and SRD5A3) are present in the human. PCR analysis was conducted to detect the mRNA expression of these proteins in both rhesus macaque hearts and iPSC-CMs used in this study (Fig. 37A).

Messenger RNAs of 5α-reductase type 2 and type 3 were identified in rhesus macaque hearts with only minimal traces of type 1 and aromatase present in two female heart samples. PCR analysis revealed the presence of mRNA of all four genes in hiPSC-CMs. However, no *CYP19A1* expression was detected in RhiPSC1-CMs.

Further immunofluorescence imaging and Western blot analysis revealed the presence of SRD5A2 in iPSC-CMs (Fig, 37B and C). The protein was localized in the cytoplasm, close to the nuclear area of hiPSC1 and RhiPSC1 cells. Notably, no indication of SRD5A3 and aromatase enzymes were present in hiPSC1 and RhiPSC1- CMs. This observation dismisses the possibility of estradiol production. SRD5A1 enzyme needs to be studied in iPSC-CMs in the future.

The subsequent step involved the visualization of the enzymes in rhesus macaque healthy adult heart tissues (Fig. 38). Immunohistochemistry analysis revealed SRD5A2 presence in the endothelial zone of capillaries and larger blood vessels of both male and female hearts. Consistent with the data from iPSC-CMs, no strong staining of SRD5A3 was observed in rhesus macaque heart tissue.

Since SRD5A2 was detected in blood vessels, we decided to explore its presence in rhesus macaque cardiomyocytes using immunofluorescence staining to enhance signal detection (Fig. 39). This allowed the visualization of 5α-reductase type 2 in the nuclei of male, but not female cardiomyocytes. The signal was also positive in blood vessels (data not shown). In female samples, mostly non-cardiac cells were positive. Furthermore, both cytoplasmic and nuclear localization were confirmed by confocal imaging of SRD5A2 in hIPSC1 and RhiPSC1 cardiomyocytes. This finding provides the possibility of T conversion to DHT within the cardiomyocytes.

To explore the presence of androgen metabolites, we conducted pilot LC-MS/MS and experiments in collaboration with Dr. Annekathrin Keiler from the Institute of Doping Analysis and Sports Biochemistry, Dresden. The results of this study are depicted in Figure 40. In the T graph, the last column represents the 100 nM T media without exposure to cells, serving as an internal control for this investigation. No androgen metabolites were detected in non-treated hiPSC1, RhiPSC1-derived cardiomyocytes, and media with no T (not shown).

Interestingly, minimal T levels remained in the media of hiPSC1- CMs 48 hours after media addition to the cells. In contrast, androstenedione appeared in both media samples of 25 nM T and 100 nM T-treated hiPSC1 cells, but only traces were detected in RhiPSC1 media samples. Androstenedione can bind to AR with substantially lower affinity than DHT[132]. As illustrated in Figure 40, T levels in rhesus samples did not change drastically between 24 and 48-hour time points. One of the three metabolites DHT, androstenediol, or androsterone is present in media. Notably, its levels remain mostly the same after 24 and 48 hours of T treatment. However, the signal reaches only around 3000 arbitrary units compared with 10,000-70,000 units in androstenedione.

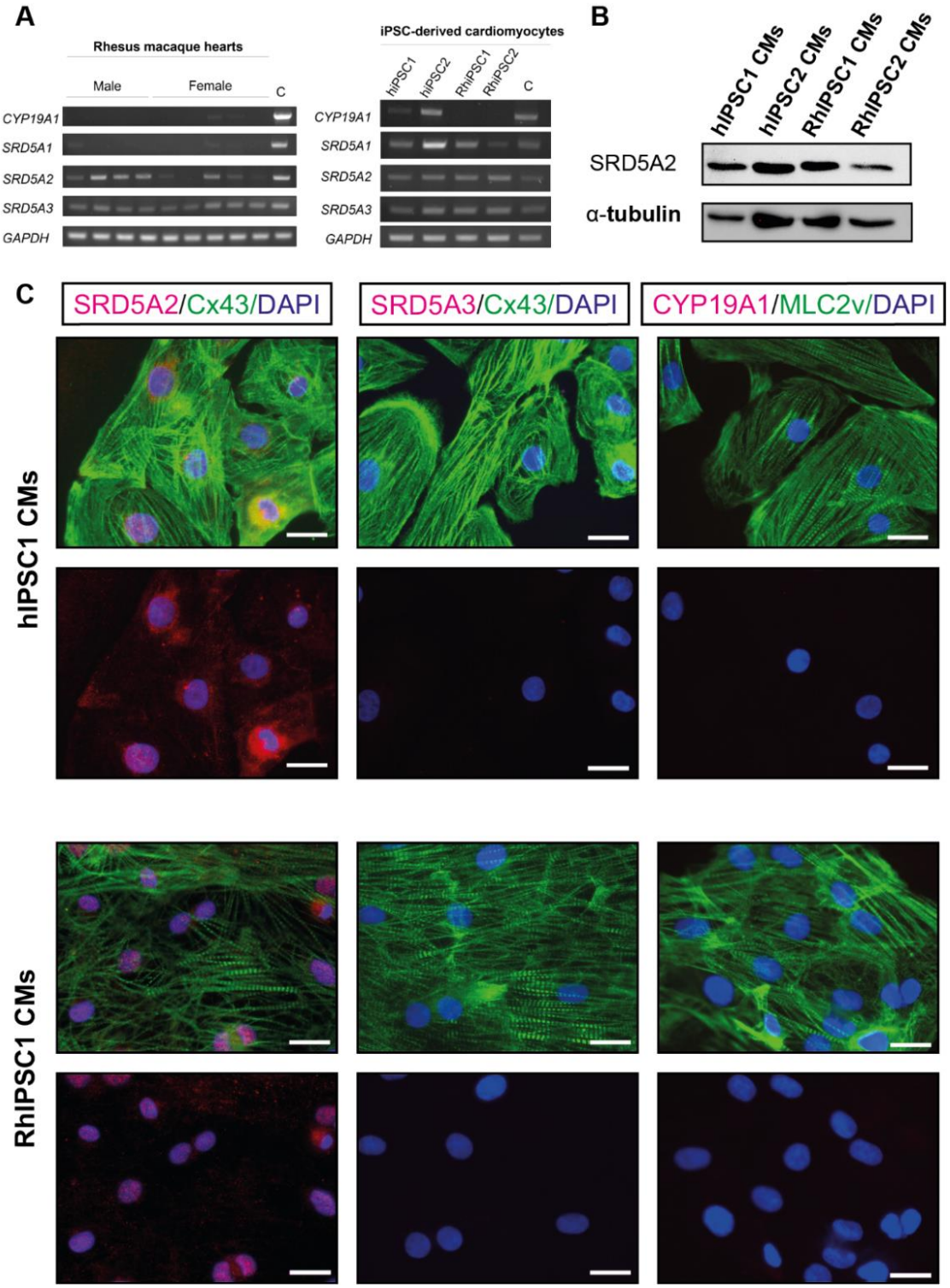

Figure 37. Testosterone-converting enzymes in primate cardiomyocytes. (A) PCR analysis revealed the presence of 5 alpha-reductase types 2 and 3 in rhesus macaque hearts and weak or no signal of type 1 and aromatase (*CYP19A1*) mRNA. Both enzymes and their isozymes mRNA were found in hiPSC1-CMs, but no aromatase mRNA was detected in RhiPSC1-CMs. **(B)** Western Blot revealed the presence of 5 alpha-reductase type 2 in all four iPSC-derived cardiomyocytes. **(C)** Immunofluorescence staining demonstrated the presence of 5 alpha-reductase type 2, but not type 3 and aromatase in hiPSC1 and RhiPSC1 CMs. Scale bars: 20 μm.

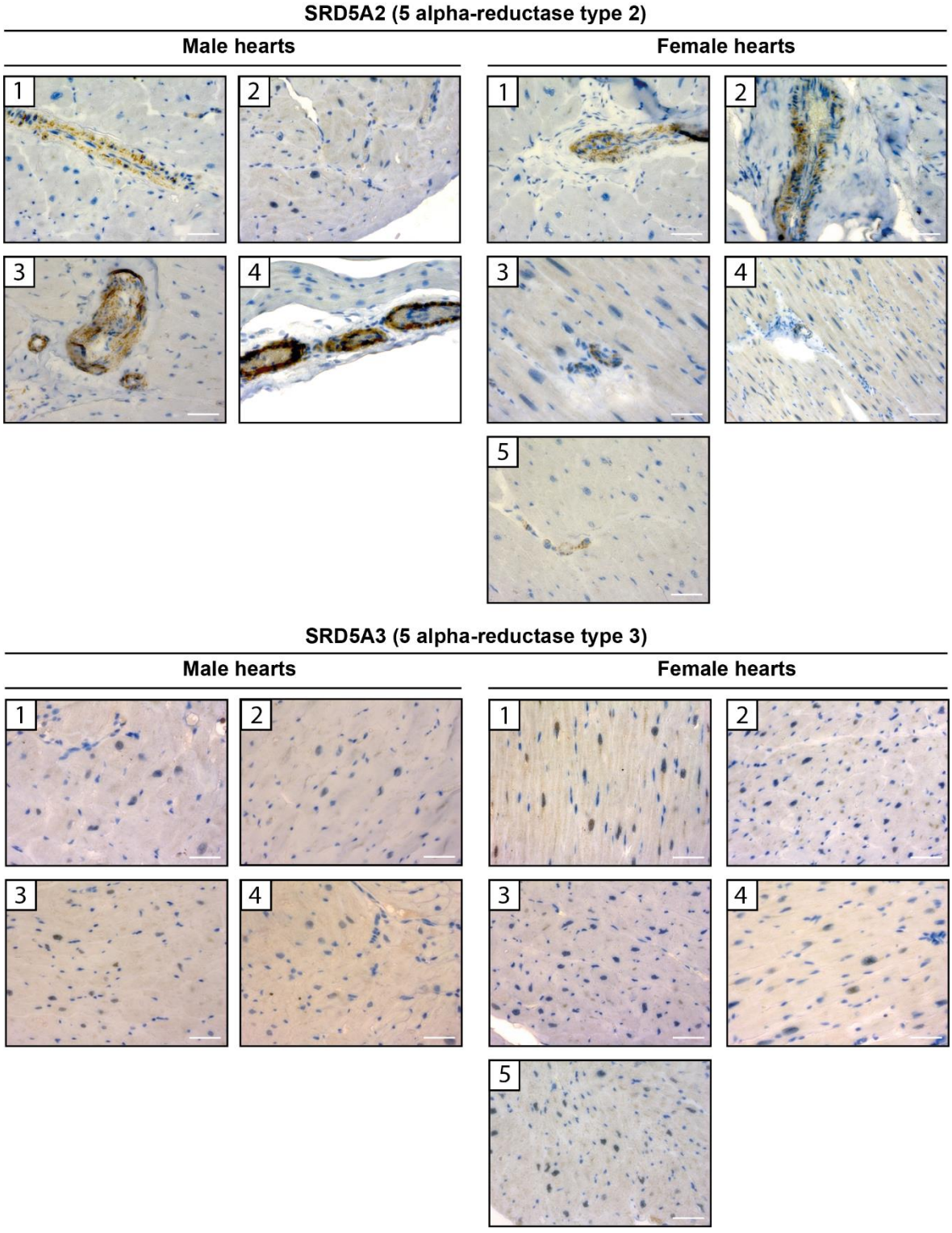

Figure 38. Immunohistochemistry analysis demonstrated the presence of 5 alpha-reductase type 2, but no clear signal of type 3 reductase. SRD5A2 is localized mainly to the *Tunica muscularis* of arteries. Additional weak staining was detected in the cytoplasm of cardiomyocytes.

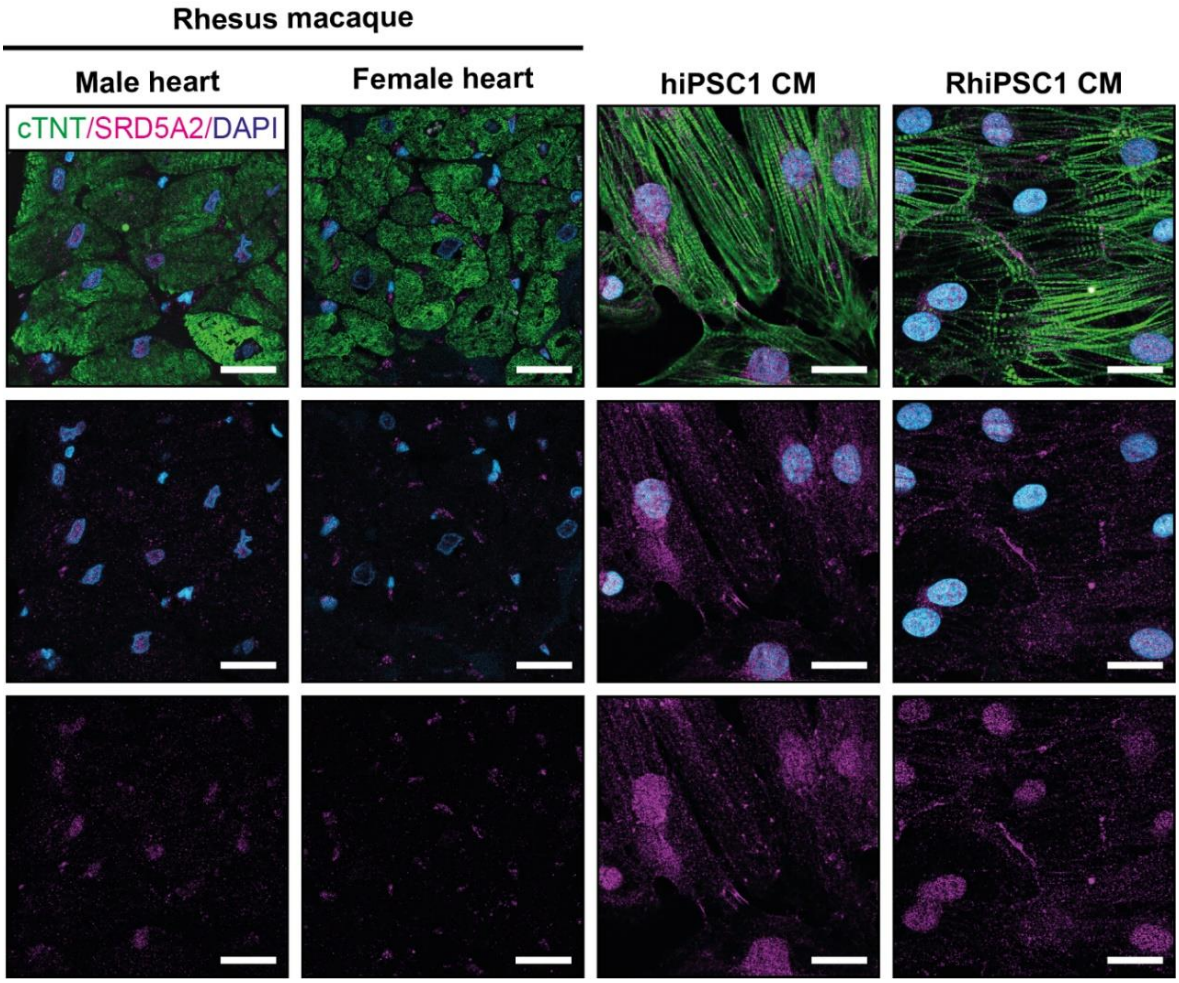

Figure 39. Immunofluorescence staining of SRD5A2 enzyme in male and female rhesus macaque hearts as well as in hiPSC1 and RhiPSC1-CMs. The enzyme was found in the nuclei of macaque hearts and the cytoplasm and nuclei of iPSC-CMs. In female hearts, the signal is localized mostly to non-muscle cells. Scale bars: 20 μm.

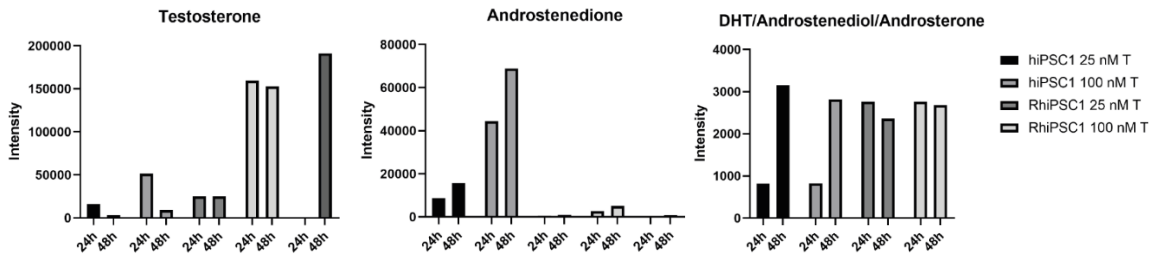

Figure 40. LC/MS analysis of androgen metabolites in media 24 and 48 hours after addition to the cells revealed the presence of T, androstenedione, and one of the other three possible metabolites with the same mass – DHT, androstenediol, and androsterone.

6 Discussion

Testosterone, the primary steroid sex hormone, essentially contributes to the development of various systems in the body[2]. Its influence is greatly studied in the reproductive tissues, but the knowledge about its impact on other organs is limited. Most of the studies address the action of androgens in prostate cancer cells and the reproductive organs, while in some healthy tissues, the presence and function of the AR were not investigated.

The cardiovascular system comprises a strictly regulated and coordinated network of organs and tissues. Various biological molecules, including hormones, have the potential to change the anatomy and physiology of the heart. Estradiol[133], triiodothyronine[105], and Dexamethasone[106] differentially impact cardiomyocytes' molecular and cellular parameters. To date, only minimal information is known about T and its action in the human heart.

This thesis aimed to investigate the effect of physiological and supraphysiological concentrations of T in primate cardiomyocytes. Cardiac differentiation of the iPSCs was optimized to produce a high number of male and female CMs of human and rhesus macaque origin. Moreover, we detected the receptor of T - the AR, which is the tissue-specific mediator of androgen action - in male rhesus macaque hearts, male and female iPSCs, and iPSC-CMs. After differentiating cells to CMs, we detected AR in the absence of T in the cytoplasm of primate iPSC-CMs. Physiological (25 nM) and supraphysiological (100 nM) T treatment triggered an AR induction in rhesus male iPSCs and iPSC-CMs. Additionally, immunostaining showed AR localized to the nuclei in T-treated cells, whereas a weak cytoplasmic signal was detected in non-treated cells. Notably, an AR isoform, AR-V7, was detected in addition to the full-length AR isoform (AR-FL) in human but not rhesus CMs. The AR-V7 isoform does not have the T-binding properties of the canonical protein. Moreover, AR-V7 mRNA was found in the human left ventricle tissue. Patch-clamp analysis showed a negative effect of 100 nM T on Ca^{2+} current density in human male iPSC-CMs treated for 24 hours, but no effect of two T treatments after 48 hours.

A human male AR knock-out iPSC line was generated to investigate the AR role in cardiac development and T effects independent of the AR receptor. The mutation in the N-terminal domain resulted in a 5-nt insertion that disrupts the open reading frame and produces a non-functional protein. The presence of the pluripotency factors LIN28A, NANOG, OCT4A, and SALL4 as well as the typical morphology of the colonies of pluripotent stem cells in culture reflect the pluripotent state of the AR KO cell line. AR absence was confirmed by Western blot analysis and immunofluorescence staining. Next, cardiac differentiation of AR KO cells was achievable, however, yielded a smaller number of CMs compared with control WT cells. Heart muscle cell markers were detected in AR KO cardiomyocytes. Cx43 presence indicated the possible formation of gap junction cell-cell contacts essential for

synchronous contraction. AR KO cardiomyocytes proliferated faster and formed a more disorganized sarcomere network compared with WT cells.

Next, we tested the presence of androgen-converting enzymes in heart muscle cells. Rhesus macaque hearts and human and rhesus male iPSC-CMs contained 5α-reductase type 2, but not type 3 in the heart. Furthermore, no evidence of aromatase presence was obtained in the abovementioned cells. This provides a possibility of T conversion into the more potent T-derivative DHT. Notably, pilot LC-MS/MS analysis showed low levels of T in the media 48 hours after the addition of T to cultures of human cardiomyocytes. On the contrary, T levels in rhesus cells were stable in both 24 and 48-hour media. Surprisingly, androstenedione, a weaker androgen, has been detected in the media of human iPSC-CMs, and only its traces in rhesus cells.

6.1 Improving cardiac differentiation of human and rhesus male iPS cells

In the present study, a directed cardiac differentiation approach was used for human and rhesus macaque iPS cells. The protocol developed earlier states that 80-90% confluence is needed to begin cardiac differentiation[115]. Previous attempts based on this parameter have resulted in drastic inconsistencies and differences in cardiomyocyte numbers generated from rhesus iPS cells. Eventually, differentiations resulted in a small number of cardiomyocytes generated and low to no presence of beating clusters. Upscaling functional beating CM culture is essential for further analyses of cellular and molecular processes.

In this thesis, instead of confluence, we used a specific cell number as a main parameter to start of cardiac differentiation hoping to increase the cardiomyocyte yield. Five to six different seeding densities were tested to produce the most cardiomyocytes (Fig. 15). Eventually, one of the cell densities (indicated by the red arrow in the graphs), resulting in more than 70% cardiomyocytes for human cells and approximately 60% for rhesus cells before metabolic selection, was chosen for all subsequent differentiation experiments. Metabolic selection was then used for the generation of high-purity cardiomyocyte cultures of more than 87% of three cell lines (Fig. 16). The generation of an almost pure culture is essential for the accuracy and reproduction of experimental results. However, around 70% of cardiomyocytes formed from hiPSC2 cells. This can be explained by the possible higher proliferation rates of non-cardiac cells of hiPSC2 origin than in other cells. Moreover, a selection of more than 7 days may be needed to generate a highly CM-enriched culture from this cell line.

Generated cardiomyocytes of all four cell lines expressed sarcomere and gap junction proteins essential for cardiac function (Fig. 17). A level of heterogeneity was present based

on observed differences in morphologies. Small and big cells of round, triangular, multiangular, and spindle-like shapes were detected in all four cell lines. Immunofluorescence staining showed cardiac-specific protein expression represented by MLC2a, MLC2v, cTNT, and α-actinin. The staining also revealed different degrees of organization in a sarcomere cross-striation pattern in each cell line. Connexin 43 was detected at cell-cell contacts between cardiomyocytes indicating the formation of gap junctions. These findings align with previous studies that have demonstrated the differentiation of iPSCs into cardiomyocytes[134].

Altogether, the fine-tuning of cardiac differentiation enabled the production of large quantities of cardiomyocytes used for further analyses in this project. Notably, rhesus cells generated fewer cardiomyocytes (reduced percentage of CM compared to all cells in the culture) compared with human cells. Why such differences occur should be investigated in the future. Potential reasons may include species-specific differences and DNA methylation differences between the cell lines.

6.2 Androgen receptor in non-human primate hearts

Testosterone exhibits its main action by binding to the AR. The presence and localization of AR have been investigated so far mainly in rodents[69,73]. While only Western blot analysis was used to detect AR in rat cardiomyocytes, another study has also visualized it in male and female mice using immunohistochemistry analysis and *in vivo* imaging of androgen-mediated luciferase activity[69]. This analysis revealed strong *AR* expression in certain tissues of male and female mice. Low activity was detected around the atrial region and vascular bundle in the heart. Immunostaining showed AR presence in the cytoplasm and nuclei of murine cardiomyocytes. Another study has also detected AR in the heart lysates of adult baboons and fetal rhesus monkeys[135,136]. Biochemical analyses detected AR in the nuclei of atrial and ventricular baboon cardiomyocytes. These findings align with the data from rodent models. This study[135] included not only baboons but also adult female rhesus macaques. Ovaries and adrenal glands were removed from monkeys and 1 µg [^{3}H] DHT was injected per 1 kg of body weight. Autoradiography showed [^{3}H] DHT incorporation in cardiomyocyte nuclei, but no data about [^{3}H] DHT levels in the serum and AR presence in rhesus macaque subjects were available. Additionally, the use of 1 µg of DHT may surpass its physiological range. Notably, no male subjects were used in the described non-human primate studies.

This project investigated AR presence in male and female rhesus macaque cardiomyocytes. Human and rhesus iPSCs were used to differentiate them into functional CMs. AR was not

previously detected in human hearts and no access to human tissues was available in this study. To tackle this limitation, we chose rhesus macaques - the closest-to-human NHP model available for this study. Our findings indicate the presence of AR in some, but not all CMs in male rhesus macaque hearts (Fig. 18). This heterogenous distribution of the AR signal corresponds to data available from mice[69]. Moreover, AR was found in both atria and ventricles of rhesus macaque male hearts (Fig. 19). Although we detected *AR* mRNA in both sexes, no signal was detected in the immunohistochemistry staining of female hearts (Fig. 18C). High variability in *AR* mRNA relative expression in female left ventricles may explain the absence of a significant difference compared with male hearts, although three out of four female samples had lower expression than the male samples (Fig. 18D). Larger sample sizes are needed to test for significant differences.

The hormone measurement conducted in this study showed lower T levels in female macaques compared with male subjects (Fig. 18B). This analysis does not discriminate between T and DHT. So, the values reflect the presence of both T and DHT. In this project, the serum samples were provided from adult monkeys that represented a healthy and non-treated control group from the previously conducted study in DPZ. Hence, no additional hormonal injections were done compared with the study that used [^{3}H] DHT incorporation[135].

This work demonstrates the first data about AR presence and localization in adult healthy rhesus macaque male and female hearts. While we observed this protein in some nuclei of male cardiomyocytes, no signal was found in female hearts. Additional mass-spectrometry analysis should be used to confirm the absence of AR in female tissue. Further investigation involving also human samples is needed for a broader understanding and *in situ* reference for studies done in this project using human iPSC-CMs. It will further strengthen or challenge the translatability of the data generated in this study.

6.3 Androgen receptor in primate iPSCs and iPSC-derived cardiomyocytes

Previous studies have shown the impact of androgens on cardiomyocyte size and excitability in murine and rat cells (in)dependent on receptor presence[75,76,137]. During the early postnatal period, a shift from cell division to cell enlargement is needed for further development of the heart[102]. The placenta serves as a barrier, regulating the transfer of multiple molecules. However, current hypothesis states that due to lipophilic nature androgens freely diffuse through membranes to the embryo[138]. Moreover, AR was detected in the inner cell mass of murine preimplantation embryos and murine cardiomyocytes of atria and ventricles as early as 12.5 dpc[71]. During this time chambers of the heart are forming, suggesting T / AR engagement in embryo and cardiac development.

Induced PSCs enable the *in vitro* modeling of various developmental processes and their comparison to human embryos. Given the data from mice, we proceeded to detect AR in male and female iPSCs of human and rhesus macaque origin. Immunofluorescence staining showed AR presence in both the cytoplasm and some nuclei of all iPSC lines (Fig. 20). These data are in agreement with a study showing diffuse AR staining in cytoplasm and nuclei of murine ESCs[139]. Such knowledge challenges the classical theory of AR presence in the cytoplasm when the ligand is absent and its translocation to the nucleus only upon hormone binding. However, some studies show AR binding, even in the absence of T, to chromatin in loci similar to antagonist-occupied AR in prostate cancer cells[140]. The data from this study provide additional evidence of AR action in the nucleus independent of its ligand. More analyses using ChiP-sequencing in the future will help in understanding this process in various cell types.

Western blot analysis detecting AR further revealed two bands in male iPSCs and only one in female cells (Fig. 20B). To date, no study reported the presence of two closely migrating western blot bands in any of the cells. The unknown origins of these two bands can be further investigated via MS/MS analysis. While the upper band aligns well with the positive control, the lower band can potentially represent AR-FL with post-translational modifications or another AR isoform.

Induced PSCs were further treated with 100 nM T for 72 hours, but no *AR* increase was detected in all four cell lines (Fig. 20C). Although no changes were detected in mRNA levels, physiological and supraphysiological T treatment for 48 hours led to a stronger AR signal in nuclei of male iPSCs compared to DMSO control (Fig. 21 and 22). Moreover, this increase in nuclei was mostly detected in the periphery of the colonies. Despite that, AR was still detected in the cytoplasm of all three treatment groups. Notably, the nucleoli were devoid of AR. AR protein expression was induced relative to alpha-tubulin by the treatment of rhesus male iPSCs with physiological T concentrations. No changes in *AR* expression suggest post-transcriptional mechanisms of AR induction. More replicas are needed to test the statistical significance due to highly variable results in 100 nM T-treated rhesus cells and results obtained from T treatment in human iPSCs.

Immunofluorescence and Western blot analysis were used to further investigate AR in human and rhesus macaque iPSC-CMs (Fig. 23). Diffuse cytoplasmic staining was detected in all non-treated cells except human female CMs (hiPSC2). Western blot further showed minimal traces of canonical full-length AR (AR-FL) in these cells (Fig. 23B). A strong signal was detected in female and male rhesus iPSC-CMs. This contradicts the immunohistochemistry staining of rhesus female hearts with no AR signal. However, rhesus iPSC-CMs still exhibit immature properties and cannot fully recapitulate adult

cardiomyocytes[134]. Further maturation of this cell line and more biological iPSC replicas are needed to investigate such discrepancy[126].

Notably, two bands were detected in human male iPSC-CMs (Fig. 23B). The upper band represents the AR-FL. The lower band aligns with another band in the positive control, i.e. the 22RV1 prostate carcinoma cell line. Additionally, cell lysates from T-treated hiPSC1-CMs also showed the presence of this band (Fig. 24B). Several AR isoforms were detected in prostate carcinoma cells, including the AR-V7 isoform. This variant is abundantly present and investigated in the 22RV1 cell model[141]. Containing no ligand-binding domain, its action is independent of T presence. AR-V7-specific primers were developed to investigate its presence in hiPSC1-cardiomyocytes. PCR analysis showed the detection of the band of interest in 22RV1 cells as well as in non-treated and T-treated human male cardiomyocytes (Fig. 24C). Moreover, the same band was detected in cDNA from a human left ventricle sample.

Various studies addressed the similarities and differences between the action of AR-FL and AR-V7[38,142–144]. The V7 variant can activate the transcription of AR-regulated genes but also impact other targets independent of AR-FL[143]. Additionally, AR-V7 and AR-FL can form homodimers and heterodimers containing one FL and one V7 subunit[39]. Little is known about whether these pairs act differentially or synergistically. Even less is known about their action in healthy cells. AR-V7 was detected in reproductive organs like the prostate[145], but no information is available about its presence in the cardiovascular system. AR-V7-specific antibodies need to be used to confirm the presence of the variant on the protein level. Higher protein load and quantitative approaches are needed to investigate the AR induction in hiPSC- CMs. Additionally, ChIP-seq and single-cell approaches may unravel similarities and differences in the action of canonical and V7 isoforms.

Western blot analysis showed a 5-10-fold AR induction in rhesus iPS-CMs treated with physiological and supraphysiological concentrations (Fig. 25B). Notably, no difference was detected between the two treatments. The gels showed the presence of only AR-FL and no other isoforms. This represents a difference between human and rhesus macaque male cell lines. A strong nuclear signal based on immunostaining suggests AR transcriptional activity in some RhiPSC1 CMs, but some cardiomyocyte nuclei did not show any staining (Fig. 25A). This finding stands in line with the scattered AR pattern detected in male rhesus macaque hearts. Single-cell RNA sequencing can be further used to identify the differences between AR-positive and negative cells.

The cardiomyocytes were treated with T also for seven days to investigate its impact on sarcomere development. Notably, a reduction in sarcomere length was found in 100 nM T-

treated CMs compared with 25 nM T group (Fig. 26). However, no significant changes were detected when comparing this parameter to non-treated cells. Additionally, a trend (p=0.0783) toward higher sarcomere organization scores (SOS) was found in the 25 nM T-treated group compared to the DMSO control. No significant changes were detected in 100 nM T-treated cells in both sarcomere length and SOS compared to non-treated cells. Taken together, AR induction did not differ between the conditions, but sarcomere length was significantly higher in the 25 nM T condition. This finding proposes the different impacts of supraphysiological and physiological T levels independent of changes in AR quantity. Densitometry, however, has its limitations, so mass spectrometry and proximity ligation assays can be used for further investigation of protein quantities and protein-protein interactions. Additionally, more analyses detecting electrophysiological, morphological, and genetic parameters need to be used for further investigation of T impact on rhesus cardiomyocytes.

6.4 Successful generation of AR KO cell line

In this study, the piggyBac transposon/transposase system harboring a CRISPR/Cas9 cassette was used to generate AR knock-out cells as described before[124]. The transposase recognizes piggyBac-specific inverted terminal repeat sequences (ITRs) located on both sides of the transposon cassette. Further excision of the CRISPR/Cas9 region leads to its integration into the TT/AA chromosomal site in the genome of iPSCs. The CRISPR/Cas9 cassette was previously integrated into the piggyBac backbone carrying all necessary elements for further genetic modification[124]. Kindly provided by the colleagues from the lab, Ptt-PB-eCas9-GFP-gRNA and pBase-tdTomato vectors were used for transfection. sgRNA 5 was designed and inserted into the vector to target the N-terminal domain, encoded by exon 1, to mutate the AR. After co-transfection with the two above-mentioned vectors, cells were sorted using a GFP reporter, expanded, and analyzed. One clone showed a 5-nt insertion in exon 1 of the AR locus on the X chromosome and further analyses confirmed the absence of protein (Fig. 27, 29). The main limitation is the integration of the piggyBac containing CRISPR/Cas9 cassette into the genome. However, its integration is reversible, so that it can be removed from the modified cells[124] in the future by re-expression of pBase-tdTomato, which will excise the fragment from the genome.

Characterization by colony morphology, pluripotency markers, and their ability to differentiate into CMs confirmed the pluripotent state of the cells[146] (Fig. 27 and 28). Other analyses such as transcriptome analysis, karyotyping, whole-genome sequencing, and embryoid body formation are needed to fully characterize the cells.

T treatment of WT cells showed clear signals in AR immunofluorescence staining and western blot analysis (Fig. 28). In contrast, no signals were obtained in both assays with the AR KO cells. However, the pluripotency markers LIN28A, NANOG, SALL4, and OCT4A were all present in the WT as well as in the AR KO cells and showed comparable signal intensities (Fig. 28). As a limitation, it must be noted that in the present work, only one AR KO line was available. Additional independent cell lines need to be analyzed. However, the data available so far suggest that the AR is not required for pluripotency of stem cells.

This is the first AR KO human iPS cell line generated to date. Its further characterization and use will allow us to study the AR-independent effects of T on iPSCs and the cell types differentiated from them. As mentioned, additional biological replicas of human and rhesus AR KO cell lines should be generated to study substantiate the biological effects seen in the present study.

6.5 AR KO cardiomyocytes represent a more immature state than WT cells

Previous investigations of T influence on CMs mostly used androgen antagonists that bind to the ligand-binding domain of the AR. Since human iPSC-CMs express besides the AR-FL isoform also the AR-V7 isoform that lacks the ligand-binding domain (and thus cannot be activated or blocked by T antagonists or agonists, respectively), we chose the AR knock-out approach. The generated cell line was further used for cardiac differentiation. The analysis revealed a lower number of CMs generated from all tested cell seeding densities compared with WT cells (Fig, 30). After 7 days of metabolic selection, recovery, and splitting, cardiac markers MLC2v, MLC2a, cTNT, α-actinin, and gap junction protein Cx43 were detected in both WT and KO CMs (Fig. 31). KO CMs exhibited higher proliferation than WT CMs, but no effect of T was detected in both cell lines (Fig. 32). This suggests that T does not affect the cell division rate, but the AR may have an influence on it in an androgen-independent manner. Another analysis involved the investigation of sarcomere structure and positioning, which can be affected by various molecules[47,105,147]. Although sarcomere length was higher in KO cells, the organization of sarcomeres calculated using the SOS parameter showed an almost two-fold decrease in KO cells compared with WT (Fig. 33B). Notably, sarcomeres of hiPSC1 CMs were around 1.9-2.0 µm long similar to most of the published 2D and 3D iPSC models[148–150] and the adult CMs *in vivo* (*in situ*) of 2.0-2.2 µm distance between sarcomeres. Immunofluorescence staining also showed a more disorganized sarcomere structure in KO cells compared with WT (Fig. 33A). 100 nM T treatment had a significantly higher SOS than 25 nM T and a similar trend was detected in comparison to non-treated cells (Fig. 33B). It must be noted, however, that the AR KO cells express GFP from the genomically inserted piggyBac transposon (Ptt-PB-eCas9-*GFP*-

gRNA), while the WT do not. In future studies, the effect of the integrated cassette needs to be excluded. However, none of the T treatments significantly impacted sarcomere organization in WT cells. Not much information is known about how exactly sarcomeres form and only the role of some proteins has been investigated while the full machinery and its development are yet to be described[147,151].

We further performed patch-clamp analysis to investigate the T effect on Ca^{2+} homeostasis (Fig. 34). T led to a decrease in Ca^{2+} current density in 100 nM T-treated WT cells compared with 25 nM T-treated and non-treated cells. This suggests T action on Ca^{2+} handling and further contractile function at least in supraphysiological doses. Previous studies have shown the opposite effect of 100 nM T treatment in human and rat cells[85,86]. However, the range of whole-cell $I_{Ca,L}$ current density in the study using isolated human CMs reached only -2 to -3 pAp/pF, while in the present study, the range of values was -10 to -15 pA/pF. This indicates a higher amount of calcium ions passing through the ion channels, hence, greater excitability, in iPSC-CMs compared with isolated cells from the hearts used in the abovementioned study. This finding suggests that additional studies using multiple biological replicas in the future to elaborate T impact on changes in Ca^{2+} levels.

The shift from hyperplasia to hypertrophy is essential for cardiac maturation[102]. This process has been partially achieved using the iPSC model[134]. Based on the proliferation and sarcomere analysis data from AR KO cells, they exhibited a more immature than WT cells phenotype possibly representing an earlier developmental stage. Furthermore, total RNA-sequencing analysis of two independent differentiation experiments of the AR KO cells into CMs showed the decreased expression of several genes involved in cardiac hypertrophy and development including Glucose transporter 4 *(GLUT4),* Insulin-like growth factor 2 *(IGF2),* and Calcium/calmodulin-dependent protein kinase II beta *(CAMK2B)* in KO cells (Fig. 35 and 36). GLUT4 inhibitor abolished glucose uptake needed for inducing cardiac hypertrophy by T in murine cells[76]. IGF2 treatment promotes hypertrophy but not proliferation in cultured neonatal CMs[152]. *CAMK2B* is an important member of Ca^{2+}-calmodulin signaling that was shown to be the main leverage of T-induced hypertrophy via myocyte enhancer factor 2 (*MEF2)* activation in rat CMs[73]. Altogether, this suggests that KO cells have lower expression of genes that regulate or are at least involved in the increase in size of CMs and are needed for the proper maturation and functioning of cells.

Gamma sarcoglycan (*SGCG)* expression is also decreased in the KO cells compared to WT. SGCG belongs to the family of sarcoglycan proteins that anchor dystrophin, and all together create a link between the cytoskeleton and extracellular matrix[153]. The aberrations of dystrophin and sarcoglycan complex interaction led to impairment in muscle contraction[154]. Additionally, patients with mutations in *SGCG* also have a high incidence of

cardiomyopathy, while rats with mutated *SGCG* exhibited a significant decline in contractile function[155]. AR KO cells also show downregulated expression of Potassium voltage-gated channel subfamily C member 3 *(KCNC3),* Hyperpolarization-activated cyclic nucleotide-gated channel 2 *(HCN2),* and Potassium voltage-gated channel interacting protein 2 *(KCNIP2)* compared to WT cells. These genes are involved in sodium and potassium uptake, and their deregulation hints at additional mechanisms of cardiac dysfunction of AR KO cells. HCN2 protein has been found in pacemaking and conduction systems in the heart[156]. Not much is known about *KCNC3* function, although its RNA was found in human CMs[157]. KChIP2 (*KCNIP2*) is a main transcriptional regulator of cardiac excitability, its mRNA levels are also reduced in multiple cardiac pathologies[158].

Notably, multiple vasculature factors were upregulated in KO cells compared with WT cells. The formation of blood vessels and cardiac tissue are processes closely connected during early development[159]. The initial intraembryonic vasculogenesis occurs in the cardiogenic mesoderm. Angiopoietin-1 (*ANGPT1*) plays an essential role in angiogenesis. Moreover, its cardioprotective action through integrins was investigated in serum-starved neonatal rat CMs[160]. *ANGPT1* and integrin subunit alpha 4 (*ITGA4*) expression was elevated in KO cells compared with WT hinting at possible cardiac stress. Moreover, endothelial GATA-binding factor 2 (*GATA2)* modulates stress response in CMs using two lncRNAs[161]. These are secreted by endothelial cells and act as paracrine factors affecting CMs. *GATA2* levels and smooth muscle-specific myosin heavy chain 11 *MYH11* may reflect the increase in several smooth muscle cells and together with *ANGPT1* a deficient development of CMs. Additional flow cytometry analysis of cTNT-positive cells in WT and KO cells after an extensive culture period may show the percentage of non-cardiac cells and provide deeper insights.

The hypothesis of the impaired development of KO cells into CMs can be further supported by the elevated expression levels in multiple collagen chains. Collagen IX and XII contribute to fetal development with collagen Type IX Alpha 3 Chain (*COL9A3*) expression decreasing throughout the progression[162,163]. However, other collagens, namely collagen I, II, and VI contribute to cardiac dysfunction and malignant fibrosis[164–166]. Fibrillin-1 makes up a large portion of microfibrils in extracellular matrix components, which are also found in the heart[167]. Mutations in *FBN1* lead to the development of the Marfan syndrome, a rare systemic disorder of the connective tissue[168]. Moreover, Fibrillin-1 action is proposed to compensate for collagen fiber stiffness present in cardiac fibrosis[169]. Such a process may also happen in our model since these genes display increased expression in KO cells compared with WT. However, only two independent experiments with one cell line were used for the analysis and more replicas, which could not be performed due to time constraints, are needed for testing statistical significance.

In this study, the generation of AR KO human iPSCs and their differentiation into CMs were achieved to investigate the impact of T and AR. The analyses revealed a lower number of generated CMs, higher proliferation rates, and sarcomere disorganization in KO cells compared with WT cells. Changes in multiple analyses were found comparing non-treated KO and WT cells, whereas T treatment showed so far no clear impact. Furthermore, two independent experiments showed decreased expression of several genes involved in physiological cardiac hypertrophy and increased expression in other genes suggesting more immature phenotype and possibly cardiac stress with increased fibrosis in the AR KO cells. These findings suggest a complex interplay between AR action and cardiac development. However, further research in this field is required in order to further substantiate these findings.

6.6 The ability of primate cardiomyocytes to metabolize testosterone

Androgen-converting enzymes expressed locally in various tissues allow further leverage of androgen action[170]. This study included T treatment of iPSC-CMs. Since some analyses in this Ph.D. project showed no or only little effect of T on iPSCs and CMs compared with non-treated cells, this observation gave rise to the idea of androgen conversion into other steroid metabolites. Two main enzymes, 5 alpha-reductase, and aromatase, can convert T to DHT and estradiol, respectively. The mRNAs of three 5 alpha-reductase isozymes types 1,2 and 3 were detected in murine CMs and their increased expression was found in patients with hypertrophic hearts[171]. Immunohistochemistry staining of type 3 (Human Protein Atlas) showed expression in human hearts[172], but type 1 was not detected[173]. The data for type 2 are currently not available[174]. Additionally, aromatase was detected in male, but not female hearts[175]. Altogether, this provides the possibility of T conversion in iPSC-CMs.

Due to the availability of rhesus tissue and the use of human and rhesus macaque iPSCs, we decided to investigate the presence of androgen-converting enzymes in this NHP model. PCR analysis showed the presence of 5 alpha-reductase type 2 (*SRD5A2*) and 3 (*SRD5A3*), while only traces of type 1 (*SRD5A1*) and aromatase (*CYP19A1*) were visible in two female samples and undetectable in the remaining samples (Fig. 37A). Notably, mRNA of all three isozymes was detected in human and rhesus iPSC-CMs. Although *CYP19A1* was present in the human sample, it was not expressed in rhesus cells. Immunofluorescence staining and Western blot analysis showed the presence of 5 alpha-reductase type 2, but not type 3 and aromatase in both human and rhesus iPSC-CMs (Fig. 37). Immunostainings revealed 5 alpha-reductase type 2 and not type 3 in the rhesus hearts of both sexes, prevalently in blood vessels, and weaker staining in the cytoplasm of CMs

(Fig. 38). The protein was detectable in both the cytoplasm and nuclei of male CMs, while its signal was detected only in non-muscle cells in female samples (Fig. 39). These data prove the presence of the enzyme and suggest the synthesis of DHT in primate hearts. The strong staining in blood vessel walls indicates the conversion of T and further diffusion of its highly potent metabolite DHT to various cell types of the heart. The [^{3}H] DHT was shown to be incorporated in many CMs in the abovementioned study[135]. Furthermore, male CMs may convert T on their own. This combinatory effect provides a possibility of highly regulated DHT synthesis in the CM nuclei of primate hearts and in endothelial cells.

The androgen metabolite analyses in the cell culture media of iPSC-CMs was performed in collaboration with Dr. Keiler (Institut für Dopinganalytik und Sportbiochemie, Dresden-Kreischa). The LC-MS/MS analysis revealed very little T left in the media of human CMs compared with rhesus samples (Fig. 40). Moreover, a high signal intensity of androstenedione was found in human cells compared to in rhesus cells, which produce only little androstenedione. While androstenedione initially had a range of approximately 9,000-70,000 arbitrary units, only around 3,000 units of DHT/androstenediol/androsterone were present. The potency of androstenedione is significantly lower than that of T and DHT.

This analysis confirmed T conversion into other androgen metabolites in iPSC-CMs and may explain its limited impact on CMs. Although more information is needed about what kind of metabolite was present in the DHT/androstenediol/androsterone group (due to their identical mass they cannot be discriminated in LC-MS/MS analysis), a higher prevalence of androstenedione was found in human samples. This suggests the difference in androgen conversion between rhesus and human iPSC-CMs used in this study.

This study investigated the potential conversion of T to other androgen metabolites in iPSC-CMs. The presence of 5α reductase, but not aromatase, was detected in rhesus macaque hearts. Additionally, its isozyme, type 2 was detected in rhesus heart tissue and iPSC-CMs of human and macaque origin. LC-MS/MS analysis revealed the presence of other than T androgen metabolites including androstenedione. This androgen is still able to bind to AR, although exhibits weaker effects on the AR. No data is available about the qualitative differences in actions between various androgens bound to AR, which provides a possibility for further research. Moreover, the presence of 5 alpha-reductase type 1 and 17β-hydroxysteroid dehydrogenase should be investigated in human and rhesus CMs. Characterizing the specific androgen metabolites present in the DHT/androstenediol/androsterone group and exploring the differences in androgen conversion between different primate species would provide valuable contributions to the knowledge about endocrine regulation of the heart by sex steroids in both sexes.

6.7 Conclusion, limitations, and future perspectives

This study provides novel knowledge about AR localization and T effects in primate CMs. It revealed differences between human and rhesus macaque iPSC-CMs. While human cells additionally expressed the AR-V7 isoform, rhesus cells contained only the canonical AR isoform. Moreover, we were able to show AR in the absence of T in the nuclei of male and female primate iPSCs. This suggests a possible influence of androgens on pluripotency and directed tissue differentiations. Utilizing a newly generated human AR KO cell line, we were able to investigate the importance of the AR and T action in cardiac differentiation and function modeled using iPSCs. It was evident that AR absence causes changes in proliferation, sarcomere organization, and gene expression. Further analysis of androgen conversion revealed that CMs can metabolize T and regulate hormone levels and metabolites on their own. In this context, human and rhesus cells behaved again differently.

While presenting the first more in-depth analysis in this field, the study had at the same time several limitations. The Rhesus macaque model was chosen since no access to human tissues and the ability to perform protein analysis in them was available. Only one human male left ventricular RNA sample was available. Eventually, the rhesus macaque model was substantially different from human cells based on various parameters. This needs to be taken with caution concerning further use of this model for androgen studies. It must further be considered that the rhesus male line (RhiPSC1) still has at least a portion of a reprogramming vector stably integrated into its genome. The iPSC lines are tools that provide the possibility of studying various cellular and molecular processes in CMs not accessible in the living heart *in situ*. However, the generated CMs of this and other studies still do not exhibit all the properties of adult CMs. Multiple approaches including a 3D model can be used in the future to enhance the culture characteristics. Additionally, the KO cell line may be further affected by the integration of the piggyBac transposon and possible GFP side effects. The data from this study must be interpreted as T action in developing CMs rather than the adult cells. Moreover, more biological replicas are needed to confirm the physiological relevance of the data obtained from the present study. Only male cell lines were exposed to male physiological, and supraphysiological T concentrations as female mammals show significantly reduced T concentrations and higher estrogen levels may overshadow the action of androgens in the heart. However, the study of T effects on female cells is an interesting topic for future research. Methodologically, some analyses like densitometry have their limitations, so a more precise and quantitative approach should be used in future investigations.

To conclude, both T and AR have an impact on primate CM structure and functionality as shown for the first time in this study. Their detailed effects should be further investigated in

the organismic context in NHP and also in human cell models, including not only cardiac development but also embryogenesis. T transport across the membrane using diffusion or SHBG should be further investigated in CMs. The role of AR in the nuclei with no androgens present is yet to be unravelled. Moreover, this study included ventricular CMs, so T action in atrial cells should be studied separately in the future. When AR-V7 protein presence is confirmed in healthy human tissues, separate KO cell lines of AR-FL and AR-V7 must be generated to investigate differences in their action. Moreover, the development of AR-V7 inhibitors[176] used for cancer treatments must be re-evaluated due to the possible presence of this isoform and potential side effects in the hearts of the patients. Hormones are the molecules of a myriad of actions and research in T together with other androgens and their role dependent on or independent of the AR will potentially deliver unexpected results from various tissues of both sexes.

7 Acknowledgments

I would like to express my deepest gratitude to all the people who supported me during these years of doctoral studies.

Firstly, I would like to thank my thesis advisory committee members Prof. Dr. Rüdiger Behr, Prof. Dr. Stefan Jakobs, Dr. Ufuk Günesdogan, and Prof. Dr. Katrin Streckfuß-Bömeke for their support, kind honesty and scientific discussions that helped me to shape this project in a way how it turned out. A special thank you goes to Dr. Ignacio Rodriguez Polo who supervised me during my lab rotation, master's thesis, and 1st year of doctoral studies and taught me the joys of seeking scientific knowledge. I also want to recognize an insane amount of support from the principal investigator of our department, Prof. Dr. Rüdiger Behr. Your kind words and encouragement have guided me so carefully. Additionally, I would like to thank Prof. Dr. Katrin Streckfuß-Bömeke for her expertise in cardiology and handling iPSC-CMs which has been essential for the success of this project.

I want to express my gratitude to Dr. Kerstin Mätz-Rensing and Pathology Unit in DPZ for your generosity in providing priceless healthy rhesus macaque heart tissue of both sexes. For the invaluable experience and help with hormone measurements, I am very grateful to Dr. Michael Heistermann, Andrea Heistermann, and Verena Behringer from Hormone Laboratory, DPZ. Tons of sequencing data have been analyzed by the NGS team from GZMB, Göttingen. I want to thank Dr. Gabriela Salinas-Riester, Jacqueline Fink, Susanne Luthin, and Dr. Maren Sitte for their efficiency and understanding of the time constraints. Moreover, I want to thank Prof. Dr. Tobias Moser and my dear friend. Rohan Kapoor (PhD student of the research group Synaptic Nanophysiology, MPI-NAT) has done patch-clamp analysis for me so many times. I am grateful for Dr. Annekathrin Keiler has also done such a complex analysis for identifying androgens in my media samples. I also want to thank Nico Westphal from Primate Genetics Laboratory, DPZ, and Carmela Cruz from the Department of Developmental Biology, GZMB for allowing me to use the equipment for NA and protein analyses. I cannot thank enough all the abovementioned people!

I want to acknowledge another huge supporter, my MSc/Ph.D. program IMPRS "Molecular Biology". You have done so much for all of the students and me included. It has been a great time overall and one year of being a Ph.D. student representative and I want to thank you for a rare opportunity to discuss many issues with Molbio program committee members. Additionally, I want to thank you for the financial support throughout these years.

I have so much gratitude for everyone in my department who cheered for me all the time. I feel very lucky to be surrounded by so many helpful people of various backgrounds. This island of kind diversity has been like a microcosm for me to cherish and nourish. Special

shoutout to my dearest Nesil, Lidiia, Shabnam, Angelina, Nicole, and Stoyan for giving amazing advice, helping with analyses, and sharing a cup of tea in the seminar room. I also want to thank Dr. Michael Heide for his multiple pieces of advice on nuanced scientific issues.

I want to thank my family, my friends, and especially my partner Eduardo. I still have my sanity and happiness mostly due to your constant love, support, and effort. I am looking forward to the day when you also defend and can continue the exciting scientific path. My parents, my sister, and my grandparents all have lifted my moods in so many difficult times, and I appreciate every moment of it. I also express gratitude to my friends who always reminded me that science and lab are only a part of my life and not all of it.

And lastly, I also want to thank myself. I pursued PhD from 2020 to 2024 – the first two years had COVID and the second two years my home country was invaded. These years have given me so many challenges and blessings. I know for sure that the pursuit of truthful knowledge whether you like it or not had a direct impact on how I view things for now. I am thankful but also slightly scared of what comes next. One of the life chapters comes to an end, and who knows what life brings in the future?

8 Bibliography

1. O'Donnell, L., Stanton, P., and Kretser, D.M. de (2017). Endocrinology of the Male Reproductive System and Spermatogenesis. Endotext.

2. Handelsman, D.J. (2020). Androgen Physiology, Pharmacology, Use and Misuse. Endocrinology: Adult and Pediatric *2–2*, 2368-2393.e16. 10.1016/B978-0-323-18907-1.00138-4.

3. Miller, W.L., and Auchus, R.J. (2011). The Molecular Biology, Biochemistry, and Physiology of Human Steroidogenesis and Its Disorders. Endocr Rev *32*, 81. 10.1210/ER.2010-0013.

4. Wright, A.S., Thomas, L.N., Douglas, R.C., Lazier, C.B., and Rittmaster, R.S. (1996). Relative potency of testosterone and dihydrotestosterone in preventing atrophy and apoptosis in the prostate of the castrated rat. Journal of Clinical Investigation *98*, 2558. 10.1172/JCI119074.

5. Sherbet, D.P., and Auchus, R.J. (2007). Peripheral Testosterone Metabolism. The Leydig Cell in Health and Disease, 181–188. 10.1007/978-1-59745-453-7_12.

6. Vítků, J., and Hampl, R. (2023). Steroid Conjugates and Their Physiological Role. Physiol Res *72*, S317–S322. 10.33549/PHYSIOLRES.935080.

7. Srinivasan, B., and Premkumar, S. (2012). Assessment of serum dehydroepiandrosterone sulphate in subjects during the pre-pubertal, pubertal, and adult stages of skeletal maturation. Eur J Orthod *34*, 447–451. 10.1093/EJO/CJR041.

8. Lasley, B.L., Chen, J., Stanczyk, F.Z., El Khoudary, S.R., Gee, N.A., Crawford, S., and McConnell, D.S. (2012). Androstenediol complements estrogenic bioactivity during the menopausal transition. Menopause *19*, 650–657. 10.1097/GME.0B013E31823DF577.

9. Mauvais-Jarvis, F. (2011). Estrogen and androgen receptors: Regulators of fuel homeostasis and emerging targets for diabetes and obesity. Trends Endocrinol Metab *22*, 24. 10.1016/J.TEM.2010.10.002.

10. Goldman, A.L., Bhasin, S., Wu, F.C.W., Krishna, M., Matsumoto, A.M., and Jasuja, R. (2017). A Reappraisal of Testosterone's Binding in Circulation: Physiological and Clinical Implications. Endocr Rev *38*, 302. 10.1210/ER.2017-00025.

11. Dunn, J.F., Nisula, B.C., and Rodbard, D. (1981). Transport of steroid hormones: binding of 21 endogenous steroids to both testosterone-binding globulin and corticosteroid-binding globulin in human plasma. J Clin Endocrinol Metab *53*, 58–68. 10.1210/JCEM-53-1-58.

12. Hammes, A., Andreassen, T.K., Spoelgen, R., Raila, J., Hubner, N., Schulz, H., Metzger, J., Schweigert, F.J., Luppa, P.B., Nykjaer, A., et al. (2005). Role of endocytosis in cellular uptake of sex steroids. Cell *122*, 751–762. 10.1016/J.CELL.2005.06.032.

13. Nakhla, A.M., Ding, V.D., Khan, M.S., Romas, N.A., Rhodes, L., Smith, R.G., and Rosner, W. (1995). 5 alpha-Androstan-3 alpha,17 beta-diol is a hormone: stimulation of cAMP accumulation in human and dog prostate. J Clin Endocrinol Metab *80*, 2259–2262. 10.1210/JCEM.80.7.7541803.

14. Troncoso, M.F., Pavez, M., Wilson, C., Lagos, D., Duran, J., Ramos, S., Barrientos, G., Silva, P., Llanos, P., Basualto-Alarcón, C., et al. (2021). Testosterone activates glucose metabolism through AMPK and androgen signaling in cardiomyocyte hypertrophy. Biol Res *54*, 3. 10.1186/S40659-021-00328-4.

15. Hammond, G.L., and Selva, D.M. (2009). Peroxisome-proliferator receptor gamma represses hepatic sex hormone-binding globulin expression. Endocrinology *150*, 2183–2189. 10.1210/EN.2008-1289.

16. Lucas-Herald, A.K., Alves-Lopes, R., Montezano, A.C., Ahmed, S.F., and Touyz, R.M. (2017). Genomic and non-genomic effects of androgens in the cardiovascular system: clinical implications. Clin Sci (Lond) *131*, 1405. 10.1042/CS20170090.

17. Chen, F., Knecht, K., Birzin, E., Fisher, J., Wilkinson, H., Mojena, M., Moreno, C.T., Schmidt, A., Harada, S.I., Freedman, L.P., et al. (2005). Direct agonist/antagonist functions of dehydroepiandrosterone. Endocrinology *146*, 4568–4576. 10.1210/EN.2005-0368.

18. Jasuja, R., Ramaraj, P., Mac, R.P., Singh, A.B., Storer, T.W., Artaza, J., Miller, A., Singh, R., Taylor, W.E., Lee, M.L., et al. (2005). Δ-4-Androstene-3,17-Dione Binds Androgen Receptor, Promotes Myogenesis in Vitro, and Increases Serum Testosterone Levels, Fat-Free Mass, and Muscle Strength in Hypogonadal Men. J Clin Endocrinol Metab *90*, 855–863. 10.1210/JC.2004-1577.

19. Yamana, K., Fernand, L., Luu-The, V., and Luu-The, V. (2010). Human type 3 5α-reductase is expressed in peripheral tissues at higher levels than types 1 and 2 and its activity is potently inhibited by finasteride and dutasteride. Horm Mol Biol Clin Investig *2*, 293–299. 10.1515/HMBCI.2010.035.

20. The Human Protein Atlas https://www.proteinatlas.org/.

21. Oren, I., Fleishman, S.J., Kessel, A., and Ben-Tal, N. (2004). Free Diffusion of Steroid Hormones Across Biomembranes: A Simplex Search with Implicit Solvent Model Calculations. Biophys J *87*, 768. 10.1529/BIOPHYSJ.103.035527.

22. Steroid receptors and hormone action: physiological and synthetic androgens and progestins can mediate inappropriate biological effects - PubMed https://pubmed.ncbi.nlm.nih.gov/6382356/.

23. El Kharraz, S., Dubois, V., van Royen, M.E., Houtsmuller, A.B., Pavlova, E., Atanassova, N., Nguyen, T., Voet, A., Eerlings, R., Handle, F., et al. (2021). The androgen receptor depends on ligand-binding domain dimerization for transcriptional activation. EMBO Rep *22*. 10.15252/EMBR.202152764.

24. Wilson, S., Qi, J., and Filipp, F. V. (2016). Refinement of the androgen response element based on ChIP-Seq in androgen-insensitive and androgen-responsive prostate cancer cell lines. Sci Rep *6*. 10.1038/SREP32611.

25. Shaffer, P.L., Jivan, A., Dollins, D.E., Claessens, F., and Gewirth, D.T. (2004). Structural basis of androgen receptor binding to selective androgen response elements. Proc Natl Acad Sci U S A *101*, 4758–4763. 10.1073/PNAS.0401123101/SUPPL_FILE/01123FIG7.JPG.

26. Chaturvedi, A.P., and Dehm, S.M. (2019). Androgen Receptor Dependence. Adv Exp Med Biol *1210*, 333. 10.1007/978-3-030-32656-2_15.

27. Pihlajamaa, P., Sahu, B., and Jänne, O.A. (2015). Determinants of Receptor- and Tissue-Specific Actions in Androgen Signaling. Endocr Rev *36*, 357–384. 10.1210/ER.2015-1034.

28. Wang, Q., Li, W., Liu, X.S., Carroll, J.S., Jänne, O.A., Keeton, E.K., Chinnaiyan, A.M., Pienta, K.J., and Brown, M. (2007). A hierarchical network of transcription factors governs androgen receptor-dependent prostate cancer growth. Mol Cell *27*, 380–392. 10.1016/J.MOLCEL.2007.05.041.

29. Pihlajamaa, P., Sahu, B., Lyly, L., Aittomäki, V., Hautaniemi, S., and Jänne, O.A. (2014). Tissue-specific pioneer factors associate with androgen receptor cistromes and transcription programs. EMBO J *33*, 312–326. 10.1002/EMBJ.201385895.

30. Wang, Q., Carroll, J.S., and Brown, M. (2005). Spatial and temporal recruitment of androgen receptor and its coactivators involves chromosomal looping and polymerase tracking. Mol Cell *19*, 631–642. 10.1016/J.MOLCEL.2005.07.018.

31. Hu, S., Yao, G., Guan, X., Ni, Z., Ma, W., Wilson, E.M., French, F.S., Liu, Q., and Zhang, Y. (2010). Research Resource: Genome-Wide Mapping of in Vivo Androgen Receptor Binding Sites in Mouse Epididymis. Molecular Endocrinology *24*, 2392. 10.1210/ME.2010-0226.

32. Jia, L., Berman, B.P., Jariwala, U., Yan, X., Cogan, J.P., Walkers, A., Chen, T., Buchanan, G., Frenkel, B., and Coetzee, G.A. (2008). Genomic androgen receptor-occupied regions with different functions, defined by histone acetylation, coregulators and transcriptional capacity. PLoS One *3*. 10.1371/JOURNAL.PONE.0003645.

33. Kagey, M.H., Newman, J.J., Bilodeau, S., Zhan, Y., Orlando, D.A., Van Berkum, N.L., Ebmeier, C.C., Goossens, J., Rahl, P.B., Levine, S.S., et al. (2010). Mediator and cohesin connect gene expression and chromatin architecture. Nature *467*, 430–435. 10.1038/NATURE09380.

34. Massie, C.L.E., Adryan, B., Barbosa-Morais, N.L., Lynch, A.G., Tran, M.G., Neal, D.E., and Mills, I.G. (2007). New androgen receptor genomic targets show an interaction with the ETS1 transcription factor. EMBO Rep *8*, 871–878. 10.1038/SJ.EMBOR.7401046.

35. Wen, S., Niu, Y., and Huang, H. (2020). Posttranslational regulation of androgen dependent and independent androgen receptor activities in prostate cancer. Asian J Urol *7*, 203–218. 10.1016/J.AJUR.2019.11.001.

36. Kanayama, M., Lu, C., Luo, J., and Antonarakis, E.S. (2021). AR Splicing Variants and Resistance to AR Targeting Agents. Cancers (Basel) *13*. 10.3390/CANCERS13112563.

37. Katleba, K.D., Ghosh, P.M., and Mudryj, M. (2023). Beyond Prostate Cancer: An Androgen Receptor Splice Variant Expression in Multiple Malignancies, Non-Cancer Pathologies, and Development. Biomedicines 2023, Vol. 11, Page 2215 *11*, 2215. 10.3390/BIOMEDICINES11082215.

38. Kim, S., Au, C.C., Jamalruddin, M.A. Bin, Abou-Ghali, N.E., Mukhtar, E., Portella, L., Berger, A., Worroll, D., Vatsa, P., Rickman, D.S., et al. (2022). AR-V7 exhibits non-canonical mechanisms of nuclear import and chromatin engagement in castrate-resistant prostate cancer. Elife *11*, 1–49. 10.7554/ELIFE.73396.

39. Xu, D., Zhan, Y., Qi, Y., Cao, B., Bai, S., Xu, W., Gambhir, S.S., Lee, P., Sartor, O., Flemington, E.K., et al. (2015). Androgen receptor splice variants dimerize to transactivate target genes. Cancer Res *75*, 3663. 10.1158/0008-5472.CAN-15-0381.

40. Trifunović-Zamaklar, D., Jovanović, I., Vratonjić, J., Petrović, O., Paunović, I., Tešić, M., Boričić-Kostić, M., and Ivanović, B. (2022). The basic heart anatomy and physiology from the cardiologist's perspective: Toward a better understanding of left

ventricular mechanics, systolic, and diastolic function. J Clin Ultrasound *50*, 1026–1040. 10.1002/JCU.23316.

41. Sotiropoulos, F., Le, T.B., and Gilmanov, A. (2016). Fluid Mechanics of Heart Valves and Their Replacements. https://doi.org/10.1146/annurev-fluid-122414-034314 *48*, 259–283. 10.1146/ANNUREV-FLUID-122414-034314.

42. Doll, S., Dreßen, M., Geyer, P.E., Itzhak, D.N., Braun, C., Doppler, S.A., Meier, F., Deutsch, M.-A., Lahm, H., Lange, R., et al. (2017). Region and cell-type resolved quantitative proteomic map of the human heart. Nat Commun *8*, 1469. 10.1038/s41467-017-01747-2.

43. Reyaldeen, R., Chan, N., Lo Presti, S., Fava, A., Anthony, C., Rodriguez, E.R., Tan, C.D., Saliba, W., Cremer, P.C., and Klein, A.L. (2021). Pericardial Anatomy, Interventions and Therapeutics: A Contemporary Review. Structural Heart *5*, 556–569. 10.1080/24748706.2021.1989531.

44. Hall, C., Gehmlich, K., Denning, C., and Pavlovic, D. (2021). Complex Relationship Between Cardiac Fibroblasts and Cardiomyocytes in Health and Disease. Journal of the American Heart Association: Cardiovascular and Cerebrovascular Disease *10*, 1–15. 10.1161/JAHA.120.019338.

45. Kassem, M.W., Lake, S., Roberts, W., Salandy, S., and Loukas, M. (2021). Cardiac veins, an anatomical review. Translational Research in Anatomy *23*, 100096. 10.1016/J.TRIA.2020.100096.

46. Keepers, B., Liu, J., and Qian, L. (2020). What's in a cardiomyocyte – And how do we make one through reprogramming? Biochim Biophys Acta Mol Cell Res *1867*, 118464. 10.1016/J.BBAMCR.2019.03.011.

47. Wang, Z., Grange, M., Wagner, T., Kho, A.L., Gautel, M., and Raunser, S. (2021). The molecular basis for sarcomere organization in vertebrate skeletal muscle. Cell *184*, 2135-2150.e13. 10.1016/J.CELL.2021.02.047.

48. Squire, J.M. (2016). Muscle contraction: Sliding filament history, sarcomere dynamics and the two Huxleys. Glob Cardiol Sci Pract *2016*. 10.21542/gcsp.2016.11.

49. Kudryashova, N., Nizamieva, A., Tsvelaya, V., Panfilov, A. V., and Agladze, K.I. (2019). Self-organization of conducting pathways explains electrical wave propagation in cardiac tissues with high fraction of non-conducting cells. PLoS Comput Biol *15*. 10.1371/JOURNAL.PCBI.1006597.

50. Barrientos, G., Llanos, P., Basualto-Alarcón, C., and Estrada, M. (2020). Androgen-Regulated Cardiac Metabolism in Aging Men. Front Endocrinol (Lausanne) *11*, 316. 10.3389/FENDO.2020.00316.

51. Di Lodovico, E., Facondo, P., Delbarba, A., Pezzaioli, L.C., Maffezzoni, F., Cappelli, C., and Ferlin, A. (2022). Testosterone, Hypogonadism, and Heart Failure. Circ Heart Fail *15*, E008755. 10.1161/CIRCHEARTFAILURE.121.008755.

52. Corona, G., Rastrelli, G., Di Pasquale, G., Sforza, A., Mannucci, E., and Maggi, M. (2018). Endogenous Testosterone Levels and Cardiovascular Risk: Meta-Analysis of Observational Studies. J Sex Med *15*, 1260–1271. 10.1016/j.jsxm.2018.06.012.

53. Ren, J., Chen, L., Zhang, N., Chen, X., Zhao, Q., Chen, K., Li, X., Ruschitzka, F., Duru, F., and Song, J. (2020). Plasma testosterone and arrhythmic events in male patients with arrhythmogenic right ventricular cardiomyopathy. ESC Heart Fail *7*, 1547. 10.1002/EHF2.12704.

54. Studen, K.B., and Pfeifer, M. (2018). Cardiometabolic risk in polycystic ovary syndrome. Endocr Connect *7*, R238. 10.1530/EC-18-0129.

55. Vanberg, P., and Atar, D. (2010). Androgenic anabolic steroid abuse and the cardiovascular system. Handb Exp Pharmacol *195*, 411–457. 10.1007/978-3-540-79088-4_18.

56. Jankowska, E.A., Biel, B., Majda, J., Szklarska, A., Lopuszanska, M., Medras, M., Anker, S.D., Banasiak, W., Poole-Wilson, P.A., and Ponikowski, P. (2006). Anabolic deficiency in men with chronic heart failure: prevalence and detrimental impact on survival. Circulation *114*, 1829–1837. 10.1161/CIRCULATIONAHA.106.649426.

57. Wu, H.Y., Wang, X.F., Wang, J.H., and Li, J.Y. (2011). Testosterone level and mortality in elderly men with systolic chronic heart failure. Asian J Androl *13*, 759. 10.1038/AJA.2011.26.

58. dos Santos, M.R., Sayegh, A.L.C., Groehs, R.V.R., Fonseca, G., Trombetta, I.C., Barretto, A.C.P., Arap, M.A., Negrão, C.E., Middlekauff, H.R., and Alves, M.J. de N.N. (2015). Testosterone Deficiency Increases Hospital Readmission and Mortality Rates in Male Patients with Heart Failure. Arq Bras Cardiol *105*, 256. 10.5935/ABC.20150078.

59. Han, Y., Sun, W., Sun, G., Hou, X., Gong, Z., Xu, J., Bai, X., and Fu, L. (2017). A 3-year observation of testosterone deficiency in Chinese patients with chronic heart failure. Oncotarget *8*, 79835. 10.18632/ONCOTARGET.19816.

60. Güder, G., Frantz, S., Bauersachs, J., Allolio, B., Ertl, G., Angermann, C.E., and Störk, S. (2010). Low circulating androgens and mortality risk in heart failure. Heart *96*, 504–509. 10.1136/HRT.2009.181065.

61. Mirdamadi, A., Garakyaraghi, M., Pourmoghaddas, A., Bahmani, A., Mahmoudi, H., and Gharipour, M. (2014). Beneficial Effects of Testosterone Therapy on Functional Capacity, Cardiovascular Parameters, and Quality of Life in Patients with Congestive Heart Failure. Biomed Res Int *2014*. 10.1155/2014/392432.

62. Wang, W., Jiang, T., Li, C., Chen, J., Cao, K., Qi, L.W., Li, P., Zhu, W., Zhu, B., and Chen, Y. (2016). Will testosterone replacement therapy become a new treatment of chronic heart failure? A review based on 8 clinical trials. J Thorac Dis *8*, E269. 10.21037/JTD.2016.03.39.

63. Toma, M., McAlister, F.A., Coglianese, E.E., Vidi, V., Vasaiwala, S., Bakal, J.A., Armstrong, P.W., and Ezekowitz, J.A. (2012). Testosterone supplementation in heart failure: a meta-analysis. Circ Heart Fail *5*, 315–321. 10.1161/CIRCHEARTFAILURE.111.965632.

64. Tao, J., Liu, X., and Bai, W. (2020). Testosterone Supplementation in Patients With Chronic Heart Failure: A Meta-Analysis of Randomized Controlled Trials. Front Endocrinol (Lausanne) *11*, 110. 10.3389/FENDO.2020.00110.

65. Krahn, A.D., Wilde, A.A.M., Calkins, H., La Gerche, A., Cadrin-Tourigny, J., Roberts, J.D., and Han, H.C. (2022). Arrhythmogenic Right Ventricular Cardiomyopathy. JACC Clin Electrophysiol *8*, 533–553. 10.1016/J.JACEP.2021.12.002.

66. Bauce, B., Frigo, G., Marcus, F.I., Basso, C., Rampazzo, A., Maddalena, F., Corrado, D., Winnicki, M., Daliento, L., Rigato, I., et al. (2008). Comparison of clinical features of arrhythmogenic right ventricular cardiomyopathy in men versus women. Am J Cardiol *102*, 1252–1257. 10.1016/J.AMJCARD.2008.06.054.

67. Akdis, D., Saguner, A.M., Shah, K., Wei, C., Medeiros-Domingo, A., Von Eckardstein, A., Lüscher, T.F., Brunckhorst, C., Chen, H.S.V., and Duru, F. (2017).

Sex hormones affect outcome in arrhythmogenic right ventricular cardiomyopathy/dysplasia: from a stem cell derived cardiomyocyte-based model to clinical biomarkers of disease outcome. Eur Heart J *38*, 1498. 10.1093/EURHEARTJ/EHX011.

68. Diaconu, R., Donoiu, I., Mirea, O., and Bălşeanu, T. (2021). Testosterone, cardiomyopathies, and heart failure: a narrative review. Asian J Androl *23*, 348. 10.4103/AJA.AJA_80_20.

69. Dart, D.A., Waxman, J., Aboagye, E.O., and Bevan, C.L. (2013). Visualising Androgen Receptor Activity in Male and Female Mice. PLoS One *8*, e71694. 10.1371/JOURNAL.PONE.0071694.

70. Lin, A.L., McGill, H.C., and Shain, S.A. (1981). Hormone receptors of the baboon cardiovascular system. Biochemical characterization of myocardial cytoplasmic androgen receptors. Circ Res *49*, 1010–1016. 10.1161/01.RES.49.4.1010.

71. Pedernera, E., Gómora, M.J., Meneses, I., De Ita, M., and Méndez, C. (2017). Androgen receptor is expressed in mouse cardiomyocytes at prenatal and early postnatal developmental stages. BMC Physiol *17*. 10.1186/S12899-017-0033-8.

72. Krieg, M., Smith, K., and Bartsch, W. (1978). Demonstration of a Specific Androgen Receptor in Rat Heart Muscle: Relationship between Binding, Metabolism, and Tissue Levels of Androgens. Endocrinology *103*, 1686–1694. 10.1210/ENDO-103-5-1686.

73. Duran, J., Lagos, D., Pavez, M., Troncoso, M.F., Ramos, S., Barrientos, G., Ibarra, C., Lavandero, S., and Estrada, M. (2017). Ca2+/Calmodulin-Dependent Protein Kinase II and Androgen Signaling Pathways Modulate MEF2 Activity in Testosterone-Induced Cardiac Myocyte Hypertrophy. Front Pharmacol *8*. 10.3389/FPHAR.2017.00604.

74. Duran, J., Oyarce, C., Pavez, M., Valladares, D., Basualto-Alarcon, C., Lagos, D., Barrientos, G., Troncoso, M.F., Ibarra, C., and Estrada, M. (2016). GSK-3β/NFAT Signaling Is Involved in Testosterone-Induced Cardiac Myocyte Hypertrophy. PLoS One *11*. 10.1371/JOURNAL.PONE.0168255.

75. Troncoso, M.F., Pavez, M., Wilson, C., Lagos, D., Duran, J., Ramos, S., Barrientos, G., Silva, P., Llanos, P., Basualto-Alarcón, C., et al. (2021). Testosterone activates glucose metabolism through AMPK and androgen signaling in cardiomyocyte hypertrophy. Biol Res *54*. 10.1186/S40659-021-00328-4.

76. Wilson, C., Contreras-Ferrat, A., Venegas, N., Osorio-Fuentealba, C., Pávez, M., Montoya, K., Durán, J., Maass, R., Lavandero, S., and Estrada, M. (2013). Testosterone increases GLUT4-dependent glucose uptake in cardiomyocytes. J Cell Physiol *228*, 2399–2407. 10.1002/JCP.24413.

77. Altamirano, F., Oyarce, C., Silva, P., Toyos, M., Wilson, C., Lavandero, S., Uhlén, P., and Estrada, M. (2009). Testosterone induces cardiomyocyte hypertrophy through mammalian target of rapamycin complex 1 pathway. J Endocrinol *202*, 299–307. 10.1677/JOE-09-0044.

78. Vicencio, J.M., Ibarra, C., Estrada, M., Chiong, M., Soto, D., Parra, V., Diaz-Araya, G., Jaimovich, E., and Lavandero, S. (2006). Testosterone induces an intracellular calcium increase by a nongenomic mechanism in cultured rat cardiac myocytes. Endocrinology *147*, 1386–1395. 10.1210/EN.2005-1139.

79. Heinlein, C.A., and Chang, C. (2002). The roles of androgen receptors and androgen-binding proteins in nongenomic androgen actions. Mol Endocrinol *16*, 2181–2187. 10.1210/ME.2002-0070.

80. Marsh, J.D., Lehmann, M.H., Ritchie, R.H., Gwathmey, J.K., Green, G.E., and Schiebinger, R.J. (1998). Androgen receptors mediate hypertrophy in cardiac myocytes. Circulation *98*, 256–261. 10.1161/01.CIR.98.3.256.

81. Mattiazzi, A., and Kranias, E.G. (2014). The role of CaMKII regulation of phospholamban activity in heart disease. Front Pharmacol *5*. 10.3389/FPHAR.2014.00005.

82. Backs, J., Song, K., Bezprozvannaya, S., Chang, S., and Olson, E.N. (2006). CaM kinase II selectively signals to histone deacetylase 4 during cardiomyocyte hypertrophy. J Clin Invest *116*, 1853–1864. 10.1172/JCI27438.

83. Xu, L., and Brink, M. (2016). mTOR, cardiomyocytes and inflammation in cardiac hypertrophy. Biochimica et Biophysica Acta (BBA) - Molecular Cell Research *1863*, 1894–1903. 10.1016/J.BBAMCR.2016.01.003.

84. Tsai, W.C., Yang, L.Y., Chen, Y.C., Kao, Y.H., Lin, Y.K., Chen, S.A., Cheng, C.F., and Chen, Y.J. (2013). Ablation of the androgen receptor gene modulates atrial electrophysiology and arrhythmogenesis with calcium protein dysregulation. Endocrinology *154*, 2833–2842. 10.1210/EN.2012-2265.

85. Er, F., Michels, G., Brandt, M.C., Khan, I., Haase, H., Eicks, M., Lindner, M., and Hoppe, U.C. (2007). Impact of testosterone on cardiac L-type calcium channels and Ca2+ sparks: acute actions antagonize chronic effects. Cell Calcium *41*, 467–477. 10.1016/J.CECA.2006.09.003.

86. Er, F., Gassanov, N., Brandt, M.C., Madershahian, N., and Hoppe, U.C. (2009). Impact of dihydrotestosterone on L-type calcium channels in human ventricular cardiomyocytes. Endocr Res *34*, 59–67. 10.1080/07435800903136953.

87. Weber, B., Lackner, I., Haffner-Luntzer, M., Palmer, A., Pressmar, J., Scharffetter-Kochanek, K., Knöll, B., Schrezenemeier, H., Relja, B., and Kalbitz, M. (2019). Modeling trauma in rats: similarities to humans and potential pitfalls to consider. Journal of Translational Medicine 2019 17:1 *17*, 1–19. 10.1186/S12967-019-2052-7.

88. Seeley, R.J., and MacDougald, O.A. (2021). Mice as experimental models for human physiology: when a few degrees in housing temperature matter. Nat Metab *3*, 443. 10.1038/S42255-021-00372-0.

89. Cardoso-Moreira, M., Sarropoulos, I., Velten, B., Mort, M., Cooper, D.N., Huber, W., and Kaessmann, H. (2020). Developmental Gene Expression Differences between Humans and Mammalian Models. Cell Rep *33*. 10.1016/J.CELREP.2020.108308.

90. Yamanaka, S. (2020). Pluripotent Stem Cell-Based Cell Therapy-Promise and Challenges. Cell Stem Cell *27*, 523–531. 10.1016/J.STEM.2020.09.014.

91. Takahashi, K., and Yamanaka, S. (2006). Induction of Pluripotent Stem Cells from Mouse Embryonic and Adult Fibroblast Cultures by Defined Factors. Cell *126*, 663–676. 10.1016/J.CELL.2006.07.024.

92. Aboul-Soud, M.A.M., Alzahrani, A.J., and Mahmoud, A. (2021). Induced Pluripotent Stem Cells (iPSCs)-Roles in Regenerative Therapies, Disease Modelling and Drug Screening. Cells *10*. 10.3390/CELLS10092319.

93. Garbern, J.C., and Lee, R.T. (2022). Heart regeneration: 20 years of progress and renewed optimism. Dev Cell *57*, 424–439. 10.1016/J.DEVCEL.2022.01.012.

94. Cui, B., Zheng, Y., Sun, L., Shi, T., Shi, Z., Wang, L., Huang, G., and Sun, N. (2018). Heart Regeneration in Adult Mammals after Myocardial Damage. Acta Cardiol Sin *34*, 115. 10.6515/ACS.201803_34(2).20171206A.

95. Kong, P., Christia, P., and Frangogiannis, N.G. (2014). The Pathogenesis of Cardiac Fibrosis. Cell Mol Life Sci *71*, 549. 10.1007/S00018-013-1349-6.

96. Potena, L., Zuckermann, A., Barberini, F., and Aliabadi-Zuckermann, A. (2018). Complications of Cardiac Transplantation. Curr Cardiol Rep *20*. 10.1007/S11886-018-1018-3.

97. Murata, K., Ikegawa, M., Minatoya, K., and Masumoto, H. (2020). Strategies for immune regulation in iPS cell-based cardiac regenerative medicine. Inflamm Regen *40*. 10.1186/S41232-020-00145-4.

98. Okita, K., Matsumura, Y., Sato, Y., Okada, A., Morizane, A., Okamoto, S., Hong, H., Nakagawa, M., Tanabe, K., Tezuka, K.I., et al. (2011). A more efficient method to generate integration-free human iPS cells. Nature Methods 2011 8:5 *8*, 409–412. 10.1038/nmeth.1591.

99. Takahashi, F., Patel, P., Kitsuka, T., and Arai, K. (2023). The Exciting Realities and Possibilities of iPS-Derived Cardiomyocytes. Bioengineering *10*. 10.3390/BIOENGINEERING10020237.

100. Jiang, Y., Park, P., Hong, S.M., and Ban, K. (2018). Maturation of Cardiomyocytes Derived from Human Pluripotent Stem Cells: Current Strategies and Limitations. Mol Cells *41*, 613–621. 10.14348/MOLCELLS.2018.0143.

101. Setterberg, I.E., Le, C., Frisk, M., Li, J., and Louch, W.E. (2021). The Physiology and Pathophysiology of T-Tubules in the Heart. Front Physiol *12*, 718404. 10.3389/FPHYS.2021.718404/BIBTEX.

102. Li, F., Wang, X., Capasso, J.M., and Gerdes, A.M. (1996). Rapid transition of cardiac myocytes from hyperplasia to hypertrophy during postnatal development. J Mol Cell Cardiol *28*, 1737–1746. 10.1006/JMCC.1996.0163.

103. Grancharova, T., Gerbin, K.A., Rosenberg, A.B., Roco, C.M., Arakaki, J.E., DeLizo, C.M., Dinh, S.Q., Donovan-Maiye, R.M., Hirano, M., Nelson, A.M., et al. (2021). A comprehensive analysis of gene expression changes in a high replicate and open-source dataset of differentiating hiPSC-derived cardiomyocytes. Scientific Reports 2021 11:1 *11*, 1–21. 10.1038/s41598-021-94732-1.

104. Biendarra-Tiegs, S.M., Secreto, F.J., and Nelson, T.J. (2020). Addressing Variability and Heterogeneity of Induced Pluripotent Stem Cell-Derived Cardiomyocytes. Adv Exp Med Biol *1212*, 1–29. 10.1007/5584_2019_350.

105. Yang, X., Rodriguez, M., Pabon, L., Fischer, K.A., Reinecke, H., Regnier, M., Sniadecki, N.J., Ruohola-baker, H., and Murry, C.E. (2014). Tri-iodo- L -thyronine promotes the maturation of human cardiomyocytes-derived from induced pluripotent stem cells. J Mol Cell Cardiol *72*, 296–304. 10.1016/j.yjmcc.2014.04.005.

106. Gay, M.S., Dasgupta, C., Li, Y., Kanna, A., and Zhang, L. (2016). Dexamethasone Induces Cardiomyocyte Terminal Differentiation via Epigenetic Repression of Cyclin D2 Gene. J Pharmacol Exp Ther *358*, 190–198.

107. Cong, X., Zhang, S.M., Ellis, M.W., and Luo, J. (2019). Large Animal Models for the Clinical Application of Human Induced Pluripotent Stem Cells. Stem Cells Dev *28*, 1288–1298. 10.1089/scd.2019.0136.

108. Cox, L.A., Olivier, M., Spradling-Reeves, K., Karere, G.M., Comuzzie, A.G., and VandeBerg, J.L. (2017). Nonhuman Primates and Translational Research—Cardiovascular Disease. ILAR J *58*, 235. 10.1093/ILAR/ILX025.

109. Estes, J.D., Wong, S.W., and Brenchley, J.M. (2018). Nonhuman primate models of human viral infections. Nature Reviews Immunology 2018 18:6 *18*, 390–404. 10.1038/s41577-018-0005-7.

110. Fowden, A.L., Giussani, D.A., and Forhead, A.J. (2006). Intrauterine programming of physiological systems: Causes and consequences. Physiology *21*, 29–37. 10.1152/physiol.00050.2005.

111. David, A., and Pierre, L. (2009). Hippocampal Neuroanatomy 10.1093/acprof:oso/9780195100273.003.0003.

112. Vesselinovitch, D., Getz, G.S., Hughes, R.H., and Wissler, R.W. (1974). Atherosclerosis in the rhesus monkey fed three food fats. Atherosclerosis *20*, 303–321. 10.1016/0021-9150(74)90015-X.

113. Rodríguez-Polo, I., and Behr, R. (2022). Non-human primate pluripotent stem cells for the preclinical testing of regenerative therapies. Neural Regen Res *17*, 1867. 10.4103/1673-5374.335689.

114. Lo, B., and Parham, L. (2009). Ethical Issues in Stem Cell Research. Endocr Rev *30*, 204. 10.1210/ER.2008-0031.

115. Stauske, M., Rodriguez Polo, I., Haas, W., Knorr, D.Y., Borchert, T., Streckfuss-Bömeke, K., Dressel, R., Bartels, I., Tiburcy, M., Zimmermann, W.-H., et al. (2020). Non-Human Primate iPSC Generation, Cultivation, and Cardiac Differentiation under Chemically Defined Conditions. Cells *9*, 1349. 10.3390/cells9061349.

116. Rivas, A.M., Mulkey, Z., Lado-Abeal, J., and Yarbrough, S. (2014). Diagnosing and managing low serum testosterone. Proc (Bayl Univ Med Cent) *27*, 321. 10.1080/08998280.2014.11929145.

117. PLANT, T.M., ZUMPE, D., SAULS, M., and MICHAEL, R.P. (1974). An annual rhythm in the plasma testosterone of adult male rhesus monkeys maintained in the laboratory. Journal of Endocrinology *62*, 403–404. 10.1677/joe.0.0620403.

118. Stein, J.M., Arslan, U., Franken, M., de Greef, J.C., E. Harding, S., Mohammadi, N., Orlova, V. V., Bellin, M., Mummery, C.L., and van Meer, B.J. (2022). Software Tool for Automatic Quantification of Sarcomere Length and Organization in Fixed and Live 2D and 3D Muscle Cell Cultures *In Vitro*. Curr Protoc *2*. 10.1002/cpz1.462.

119. Babraham Bioinformatics - FastQC A Quality Control tool for High Throughput Sequence Data https://www.bioinformatics.babraham.ac.uk/projects/fastqc/.

120. Dobin, A., Davis, C.A., Schlesinger, F., Drenkow, J., Zaleski, C., Jha, S., Batut, P., Chaisson, M., and Gingeras, T.R. (2013). STAR: ultrafast universal RNA-seq aligner. Bioinformatics *29*, 15–21. 10.1093/BIOINFORMATICS/BTS635.

121. Liao, Y., Smyth, G.K., and Shi, W. (2014). featureCounts: an efficient general purpose program for assigning sequence reads to genomic features. Bioinformatics *30*, 923–930. 10.1093/BIOINFORMATICS/BTT656.

122. Love, M.I., Huber, W., and Anders, S. (2014). Moderated estimation of fold change and dispersion for RNA-seq data with DESeq2. Genome Biol *15*, 1–21. 10.1186/S13059-014-0550-8/FIGURES/9.

123. Zhang, B., Kirov, S., and Snoddy, J. (2005). WebGestalt: an integrated system for exploring gene sets in various biological contexts. Nucleic Acids Res *33*, W741–W748. 10.1093/NAR/GKI475.

124. Rodriguez-Polo, I., Mißbach, S., Petkov, S., Mattern, F., Maierhofer, A., Grządzielewska, I., Tereshchenko, Y., Urrutia-Cabrera, D., Haaf, T., Dressel, R., et

al. (2021). A piggyBac-based platform for genome editing and clonal rhesus macaque iPSC line derivation. Sci Rep *11*, 15439. 10.1038/s41598-021-94419-7.

125. Rincon, A. V., Ostner, J., Heistermann, M., and Deschner, T. (2019). Measuring urinary cortisol and testosterone levels in male Barbary macaques: A comparison of EIA and LC–MS. Gen Comp Endocrinol *281*, 117–125. 10.1016/j.ygcen.2019.05.017.

126. Lyra-Leite, D.M., Gutiérrez-Gutiérrez, Ó., Wang, M., Zhou, Y., Cyganek, L., and Burridge, P.W. (2022). A review of protocols for human iPSC culture, cardiac differentiation, subtype-specification, maturation, and direct reprogramming. STAR Protoc *3*, 101560. 10.1016/j.xpro.2022.101560.

127. Tereshchenko, Y. Effect of hormonal treatments on the maturation of induced pluripotent stem cell-derived cardiomyocytes.

128. Tohyama, S., Hattori, F., Sano, M., Hishiki, T., Nagahata, Y., Matsuura, T., Hashimoto, H., Suzuki, T., Yamashita, H., Satoh, Y., et al. (2013). Distinct Metabolic Flow Enables Large-Scale Purification of Mouse and Human Pluripotent Stem Cell-Derived Cardiomyocytes. Cell Stem Cell *12*, 127–137. 10.1016/j.stem.2012.09.013.

129. Pettinato, A.M., Ladha, F.A., and Hinson, J.T. (2022). The Cardiac Sarcomere and Cell Cycle. Curr Cardiol Rep *24*, 623–630. 10.1007/s11886-022-01682-9.

130. Kaku, N., Matsuda, K., Tsujimura, A., and Kawata, M. (2008). Characterization of Nuclear Import of the Domain-Specific Androgen Receptor in Association with the Importin α/β and Ran-Guanosine 5′-Triphosphate Systems. Endocrinology *149*, 3960–3969. 10.1210/en.2008-0137.

131. Hille, C., Gorges, T.M., Riethdorf, S., Mazel, M., Steuber, T., von Amsberg, G., König, F., Peine, S., Alix-Panabières, C., and Pantel, K. (2019). Detection of Androgen Receptor Variant 7 (ARV7) mRNA Levels in EpCAM-Enriched CTC Fractions for Monitoring Response to Androgen Targeting Therapies in Prostate Cancer. Cells *8*. 10.3390/CELLS8091067.

132. Jasuja, R., Ramaraj, P., Mac, R.P., Singh, A.B., Storer, T.W., Artaza, J., Miller, A., Singh, R., Taylor, W.E., Lee, M.L., et al. (2005). Δ-4-Androstene-3,17-Dione Binds Androgen Receptor, Promotes Myogenesis *in Vitro* , and Increases Serum Testosterone Levels, Fat-Free Mass, and Muscle Strength in Hypogonadal Men. J Clin Endocrinol Metab *90*, 855–863. 10.1210/jc.2004-1577.

133. Iorga, A., Cunningham, C.M., Moazeni, S., Ruffenach, G., Umar, S., and Eghbali, M. (2017). The protective role of estrogen and estrogen receptors in cardiovascular disease and the controversial use of estrogen therapy. Preprint, 10.1186/s13293-017-0152-8 10.1186/s13293-017-0152-8.

134. Yang, X., Pabon, L., and Murry, C.E. (2014). Engineering adolescence: maturation of human pluripotent stem cell-derived cardiomyocytes. Circ Res *114*, 511–523. 10.1161/CIRCRESAHA.114.300558.

135. McGill, H.C., Anselmo, V.C., Buchanan, J.M., and Sheridan, P.J. (1980). The Heart Is a Target Organ for Androgen. Science (1979) *207*, 775–777. 10.1126/science.6766222.

136. Abdelgadir, S.E., Connolly, P.B., and Resko, J.A. (1990). Androgen binding in peripheral tissues of fetal rhesus macaques: effects of androgen metabolism in liver. J Steroid Biochem Mol Biol *37*, 545–551. 10.1016/0960-0760(90)90399-6.

137. Altamirano, F., Oyarce, C., Silva, P., Toyos, M., Wilson, C., Lavandero, S., Uhlén, P., and Estrada, M. (2009). Testosterone induces cardiomyocyte hypertrophy

through mammalian target of rapamycin complex 1 pathway. Journal of Endocrinology *202*, 299–307. 10.1677/JOE-09-0044.

138. Sun, M., Maliqueo, M., Benrick, A., Johansson, J., Shao, R., Hou, L., Jansson, T., Wu, X., and Stener-Victorin, E. (2012). Maternal androgen excess reduces placental and fetal weights, increases placental steroidogenesis, and leads to long-term health effects in their female offspring. Am J Physiol Endocrinol Metab *303*, 1373–1385. 10.1152/AJPENDO.00421.2012/ASSET/IMAGES/LARGE/ZH10231267000007.JPEG.

139. Yang, Y.C., Fu, H.C., Hsiao, B.L., Sobue, G., Adachi, H., Huang, F.J., Hsuuw, Y.D., Wei, K.T., Chang, C., Huang, K.E., et al. (2013). Androgen receptor inclusions acquire GRP78/BiP to ameliorate androgen-induced protein misfolding stress in embryonic stem cells. Cell Death & Disease 2013 4:4 *4*, e607–e607. 10.1038/cddis.2013.122.

140. Chen, Z., Lan, X., Thomas-Ahner, J.M., Wu, D., Liu, X., Ye, Z., Wang, L., Sunkel, B., Grenade, C., Chen, J., et al. (2015). Agonist and antagonist switch DNA motifs recognized by human androgen receptor in prostate cancer. EMBO J *34*, 502–516. 10.15252/EMBJ.201490306.

141. Ciccarese, C., Santoni, M., Brunelli, M., Buti, S., Modena, A., Nabissi, M., Artibani, W., Martignoni, G., Montironi, R., Tortora, G., et al. (2016). AR-V7 and prostate cancer: The watershed for treatment selection? Cancer Treat Rev *43*, 27–35. 10.1016/J.CTRV.2015.12.003.

142. Rana, M., Dong, J., Robertson, M.J., Coarfa, C., and Weigel, N.L. (2021). Androgen receptor and its splice variant, AR-V7, differentially induce mRNA splicing in prostate cancer cells. Sci Rep *11*, 1393. 10.1038/S41598-021-81164-0.

143. Krause, W.C., Shafi, A.A., Nakka, M., and Weigel, N.L. (2014). Androgen receptor and its splice variant, AR-V7, differentially regulate FOXA1 sensitive genes in LNCaP prostate cancer cells. Int J Biochem Cell Biol *54*, 49–59. 10.1016/J.BIOCEL.2014.06.013.

144. Scher, H.I., Graf, R.P., Schreiber, N.A., McLaughlin, B., Lu, D., Louw, J., Danila, D.C., Dugan, L., Johnson, A., Heller, G., et al. (2017). Nuclear-specific AR-V7 Protein Localization is Necessary to Guide Treatment Selection in Metastatic Castration-resistant Prostate Cancer. Eur Urol *71*, 874–882. 10.1016/j.eururo.2016.11.024.

145. Wüstmann, N., Seitzer, K., Humberg, V., Vieler, J., Grundmann, N., Steinestel, J., Tiedje, D., Duensing, S., Krabbe, L.M., Bögemann, M., et al. (2023). Co-expression and clinical utility of AR-FL and AR splice variants AR-V3, AR-V7 and AR-V9 in prostate cancer. Biomark Res *11*, 1–14. 10.1186/S40364-023-00481-W/FIGURES/6.

146. Shi, Y., Inoue, H., Wu, J.C., and Yamanaka, S. (2017). Induced pluripotent stem cell technology: A decade of progress. Nat Rev Drug Discov *16*, 115–130. 10.1038/nrd.2016.245.

147. Bedada, F.B., Wheelwright, M., and Metzger, J.M. (2016). Maturation status of sarcomere structure and function in human iPSC-derived cardiac myocytes. Preprint, 10.1016/j.bbamcr.2015.11.005 10.1016/j.bbamcr.2015.11.005.

148. Wu, P., Sai, X., Li, Z., Ye, X., Jin, L., Liu, G., Li, G., Yang, P., Zhao, M., Zhu, S., et al. (2023). Maturation of induced pluripotent stem cell-derived cardiomyocytes and its therapeutic effect on myocardial infarction in mouse. Bioact Mater *20*, 286–305. 10.1016/J.BIOACTMAT.2022.05.024.

149. Skorska, A., Johann, L., Chabanovska, O., Vasudevan, P., Kussauer, S., Hillemanns, M., Wolfien, M., Jonitz-Heincke, A., Wolkenhauer, O., Bader, R., et al. (2022). Monitoring the maturation of the sarcomere network: a super-resolution microscopy-based approach. Cellular and Molecular Life Sciences *79*, 149. 10.1007/S00018-022-04196-3.

150. Lemcke, H., Skorska, A., Lang, C.I., Johann, L., and David, R. (2020). Quantitative Evaluation of the Sarcomere Network of Human hiPSC-Derived Cardiomyocytes Using Single-Molecule Localization Microscopy. Int J Mol Sci *21*. 10.3390/IJMS21082819.

151. Fenix, A.M., Neininger, A.C., Taneja, N., Hyde, K., Visetsouk, M.R., Garde, R.J., Liu, B., Nixon, B.R., Manalo, A.E., Becker, J.R., et al. (2018). Muscle-specific stress fibers give rise to sarcomeres in cardiomyocytes. Elife *7*, 1–33. 10.7554/eLife.42144.

152. Díaz Del Moral, S., Benaouicha, M., Muñoz-Chápuli, R., and Carmona, R. (2022). The Insulin-like Growth Factor Signalling Pathway in Cardiac Development and Regeneration. Int J Mol Sci *23*. 10.3390/IJMS23010234.

153. Valera, I.C., Wacker, A.L., Hwang, H.S., Holmes, C., Laitano, O., Landstrom, A.P., and Parvatiyar, M.S. (2021). Essential roles of the dystrophin-glycoprotein complex in different cardiac pathologies. Adv Med Sci *66*, 52–71. 10.1016/J.ADVMS.2020.12.004.

154. Politano, L., Nigro, V., Passamano, L., Petretta, V., Comi, L.I., Papparella, S., Nigro, G., Rambaldi, P.F., Raia, P., Pini, A., et al. (2001). Evaluation of cardiac and respiratory involvement in sarcoglycanopathies. Neuromuscular Disorders *11*, 178–185. 10.1016/S0960-8966(00)00174-7.

155. Townsend, D., Yasuda, S., McNally, E., and Metzger, J.M. (2011). Distinct pathophysiological mechanisms of cardiomyopathy in hearts lacking dystrophin or the sarcoglycan complex. The FASEB Journal *25*, 3106. 10.1096/FJ.10-178913.

156. Herrmann, S., Hofmann, F., Stieber, J., and Ludwig, A. (2012). HCN channels in the heart: lessons from mouse mutants. Br J Pharmacol *166*, 501. 10.1111/J.1476-5381.2011.01798.X.

157. Ördög, B., Brutyó, E., Puskás, L.G., Papp, J.G., Varró, A., Szabad, J., and Boldogkoi, Z. (2006). Gene expression profiling of human cardiac potassium and sodium channels. Int J Cardiol *111*, 386–393. 10.1016/J.IJCARD.2005.07.063.

158. Nassal, D.M., Wan, X., Liu, H., Maleski, D., Ramirez-Navarro, A., Moravec, C.S., Ficker, E., Laurita, K.R., and Deschênes, I. (2017). KChIP2 is a core transcriptional regulator of cardiac excitability. Elife *6*. 10.7554/ELIFE.17304.001.

159. Borasch, K., Richardson, K., and Plendl, J. (2020). Cardiogenesis with a focus on vasculogenesis and angiogenesis. Anat Histol Embryol *49*, 643–655. 10.1111/AHE.12549.

160. Dallabrida, S.M., Ismail, N., Oberle, J.R., Himes, B.E., and Rupnick, M.A. (2005). Angiopoietin-1 promotes cardiac and skeletal myocyte survival through integrins. Circ Res *96*. 10.1161/01.RES.0000158285.57191.60.

161. Castaño, J., Aranda, S., Bueno, C., Calero-Nieto, F.J., Mejia-Ramirez, E., Mosquera, J.L., Blanco, E., Wang, X., Prieto, C., Zabaleta, L., et al. (2019). GATA2 Promotes Hematopoietic Development and Represses Cardiac Differentiation of Human Mesoderm. Stem Cell Reports *13*, 515–529. 10.1016/J.STEMCR.2019.07.009.

162. Izu, Y., and Birk, D.E. (2023). Collagen XII mediated cellular and extracellular mechanisms in development, regeneration, and disease. Front Cell Dev Biol *11*, 1129000. 10.3389/FCELL.2023.1129000/BIBTEX.

163. Froese, N., Cordero, J., Abouissa, A., Trogisch, F.A., Grein, S., Szaroszyk, M., Wang, Y., Gigina, A., Korf-Klingebiel, M., Bosnjak, B., et al. (2022). Analysis of myocardial cellular gene expression during pressure overload reveals matrix based functional intercellular communication. iScience *25*. 10.1016/J.ISCI.2022.103965.

164. Hua, X., Wang, Y.Y., Jia, P., Xiong, Q., Hu, Y., Chang, Y., Lai, S., Xu, Y., Zhao, Z., and Song, J. (2020). Multi-level transcriptome sequencing identifies COL1A1 as a candidate marker in human heart failure progression. BMC Med *18*, 1–16. 10.1186/S12916-019-1469-4/FIGURES/7.

165. Pan, X., Chen, X., Ren, Q., Yue, L., Niu, S., Li, Z., Zhu, R., Chen, X., Jia, Z., Zhen, R., et al. (2022). Single-cell transcriptomics identifies Col1a1 and Col1a2 as hub genes in obesity-induced cardiac fibrosis. Biochem Biophys Res Commun *618*, 30–37. 10.1016/J.BBRC.2022.06.018.

166. Grossman, T.R., Gamliel, A., Wessells, R.J., Taghli-Lamallem, O., Jepsen, K., Ocorr, K., Korenberg, J.R., Peterson, K.L., Rosenfeld, M.G., Bodmer, R., et al. (2011). Over-expression of DSCAM and COL6A2 cooperatively generates congenital heart defects. PLoS Genet *7*. 10.1371/JOURNAL.PGEN.1002344.

167. Steijns, F., van Hengel, J., Sips, P., De Backer, J., and Renard, M. (2018). A heart for fibrillin: spatial arrangement in adult wild-type murine myocardial tissue. Histochem Cell Biol *150*, 271–280. 10.1007/S00418-018-1686-5/METRICS.

168. Aalders, J., Léger, L., Van der Meeren, L., Van den Vreken, N., Skirtach, A.G., Sinha, S., De Backer, J., and van Hengel, J. (2020). Effects of fibrillin mutations on the behavior of heart muscle cells in Marfan syndrome. Scientific Reports 2020 10:1 *10*, 1–16. 10.1038/s41598-020-73802-w.

169. Bouzeghrane, F., Reinhardt, D.P., Reudelhuber, T.L., and Thibault, G. (2005). Enhanced expression of fibrillin-1, a constituent of the myocardial extracellular matrix in fibrosis. Am J Physiol Heart Circ Physiol *289*. 10.1152/AJPHEART.00151.2005/ASSET/IMAGES/LARGE/ZH40090541430008.JPEG.

170. Sherbet, D.P., and Auchus, R.J. (2007). Peripheral Testosterone Metabolism. The Leydig Cell in Health and Disease, 181–188. 10.1007/978-1-59745-453-7_12.

171. Zwadlo, C., Schmidtmann, E., Szaroszyk, M., Kattih, B., Froese, N., Hinz, H., Schmitto, J.D., Widder, J., Batkai, S., Bähre, H., et al. (2015). Antiandrogenic therapy with finasteride attenuates cardiac hypertrophy and left ventricular dysfunction. Circulation *131*, 1071–1081. 10.1161/CIRCULATIONAHA.114.012066/-/DC1.

172. Tissue expression of SRD5A3 - Staining in heart muscle - The Human Protein Atlas https://www.proteinatlas.org/ENSG00000128039-SRD5A3/tissue/heart+muscle.

173. Tissue expression of SRD5A1 - Staining in heart muscle - The Human Protein Atlas https://www.proteinatlas.org/ENSG00000145545-SRD5A1/tissue/heart+muscle.

174. Tissue expression of SRD5A2 - Staining in heart muscle - The Human Protein Atlas https://www.proteinatlas.org/ENSG00000277893-SRD5A2/tissue/heart+muscle.

175. Tissue expression of CYP19A1 - Staining in heart muscle - The Human Protein Atlas https://www.proteinatlas.org/ENSG00000137869-CYP19A1/tissue/heart+muscle.

176. Uo, T., Plymate, S.R., and Sprenger, C.C. (2018). The potential of AR-V7 as a therapeutic target. Expert Opin Ther Targets *22*, 201–216. 10.1080/14728222.2018.1439016.

9 Supplementary data

Table S1. Percentage of cTNT-positive cells of hiPSC1 cell line after differentiation before selection. Four independent experiments were used for each group of cell seeding numbers.

Number of seeded cells/well	#1 (%)	#2 (%)	#3 (%)	#4(%)
150,000	45,43	44,42	37,22	40,32
200,000	50,25	52,93	60,82	50,21
250,000	59,26	50,73	63,56	56,56
300,000	75,89	79,02	70,46	79,39
350,000	71,06	66,28	73,99	69,16

Table S2. Percentage of cTNT-positive cells of hiPSC2 cell line after differentiation before selection. Three to four independent experiments were used for each group of cell seeding numbers.

Number of seeded cells/well	#1 (%)	#2 (%)	#3 (%)	#4(%)
40,000	23,27	26,99	30,88	26,8
50,000	31,8	30,54	36,73	
60,000	69,56	79,45	81,7	
70,000	75,48	79,07	74,51	77,03
80,000	73,72	78,32	75,12	
90,000	72,54	70,06	75,65	67,82

Table S3. Percentage of cTNT-positive cells of RhiPSC1 cell line after differentiation before selection. Three to four independent experiments were used for each group of cell seeding numbers.

Number of seeded cells/well	#1 (%)	#2 (%)	#3 (%)	#4(%)
80,000	44,56	37,71	33,54	44,04
100,000	42,74	50,57	56,5	36,13
120,000	60,69	56,96	62,9	51,23
140,000	52,68	51,24	65,88	55,38
160,000	20,28	11,65	38,4	
180,000	25,75	13,04	23,45	

Table S4. Percentage of cTNT-positive cells of RhiPSC2 cell line after differentiation before selection. Three to four independent experiments were used for each group of cell seeding numbers.

Number of seeded cells/well	#1 (%)	#2 (%)	#3 (%)	#4(%)
70,000	35,74	40,4	39,6	30,1
90,000	61,89	65,86	66,17	65,37
110,000	27,46	17,21	27,46	
130,000	4,89	5,48	8,11	
150,000	13,2	16,8	2,51	

Table S5. Percentage of cTNT-positive cells in hiPSC1, hiPSC2, RhiPSC1, and RhiPSC2 after metabolic selection. Three independent experiments were used for each group.

Cell line	#1 (%)	#2 (%)	#3 (%)
hiPSC1	97,65	97,04	97,72
hiPSC2	74,66	72,09	70,03
RhiPSC1	82,44	86,16	92,99
RhiPSC2	95,71	95,21	96,13

Table S6. Testosterone and E2 measurement in serum of male and female rhesus macaques using ELISA.

Animal-ID	Sex	Testosterone dilution	Testosterone EIA value (pg/50µl)	Serum testosterone (ng/ml)	Estradiol dilution	Estradiol EIA value (pg/ml)	Serum estradiol (pg/ml)
16120	male	40	10,5	8,40	4	9,9	39,6
16110	male	40	13,5	10,80	4	23,1	92,4
2245	male	40	15,7	12,56	4	42,9	171,6
2519	male	40	11,2	8,96	4	23,6	94,4
2375	female	40	0,8	0,64	4	65,8	263,2
2602	female	40	0,3	0,24	4	14,1	56,4

2718	female	40	1,3	1,04	4	12,6	50,4
2243	female	40	1,1	0,88	4	35,8	143,2
2544	female	40	0,7	0,56	4	42,3	169,2

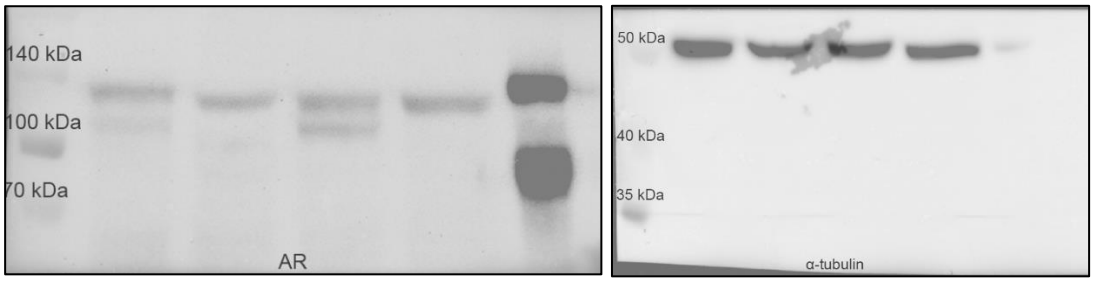

Figure S1. Western blot images used for Figure 19 B merged with colorimetric pictures containing protein ladder.

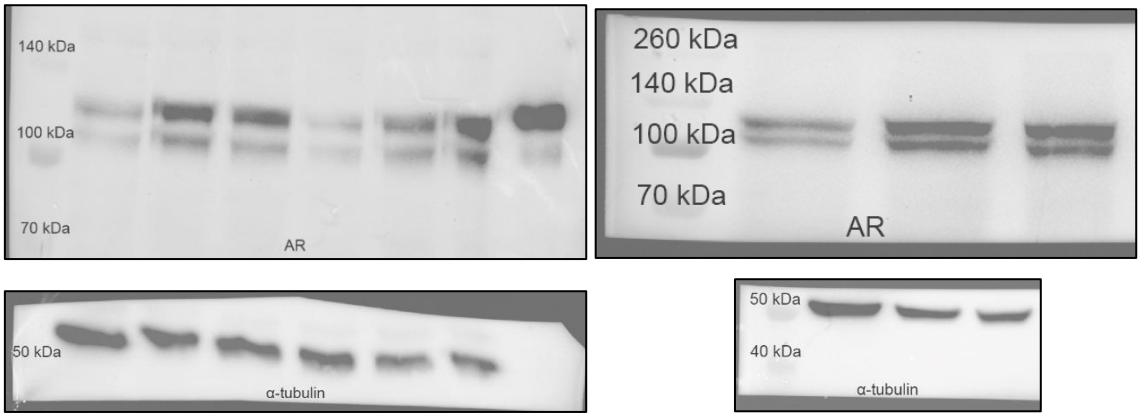

Figure S2. Western blot images used for Figure 20 B merged with colorimetric pictures containing protein ladder.

Table S7. Densitometry analysis values presented on Fig. 20 B. The ratio was measured by dividing the AR value by the α-tubulin value. Next, the average of the control group was calculated and used for further fold change calculations.

Group	AR	α-tubulin	Ratio	DMSO average	Fold change
DMSO1	14.498.413	36.552.291	0,396648544	0,379121837	1,046229749

25 T1	46.864.860	24.921.421	1,880505128		4,960160421
100 T1	37.586.375	24.296.472	1,546989003		4,080453443
DMSO2	7.420.057	21.619.401	0,343212886		0,905283876
25 T2	31.905.688	15.909.087	2,005500881		5,289858531
100 T2	50.731.730	15.571.158	3,258057622		8,593695503
DMSO3	11.839.409	29.784.371	0,39750408		1,048486375
25 T3	26.889.430	17.548.966	1,53225153		4,041580785
100 T3	24.046.329	14.026.480	1,714352354		4,521903484

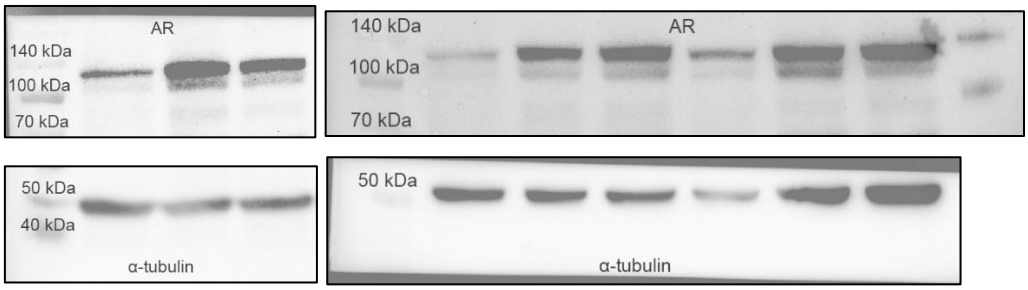

Figure S2. Western blot images used for Figure 20 B merged with colorimetric pictures containing protein ladder.

Table S8. Densitometry analysis values presented on Fig. 21 B. The ratio was measured by dividing the AR value by the α-tubulin value. Next, the average of the control group was calculated and used for further fold change calculations.

Group	AR	α-tubulin	Ratio	DMSO average	Fold change
DMSO1	10.740.368	24.423.451	0,439756364	0,75315928	0,583882
25 T1	34.280.179	13.100.430	2,616721665		3,474327
100 T1	23.552.945	13.525.551	1,741366766		2,312083
DMSO2	3.995.711	18.357.773	0,217657719		0,288993
25 T2	19.826.966	14.299.581	1,386541746		1,840967
100 T2	28.150.229	14.303.702	1,968037995		2,613044
DMSO3	9.109.924	5.686.368	1,602063743		2,127125
25 T3	35.851.856	22.185.208	1,616025236		2,145662
100 T3	75.351.357	30.787.986	2,447427285		3,249548

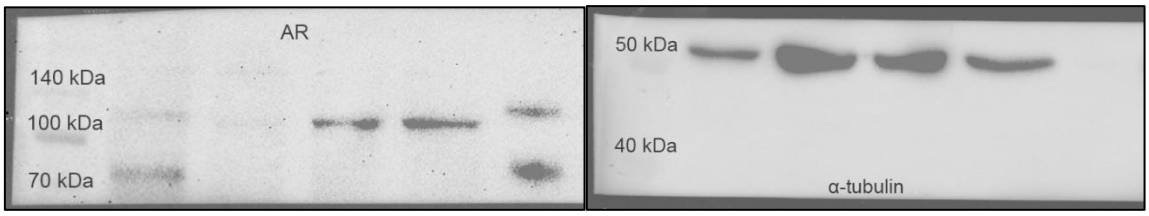

Figure S4. Western blot images used for Figure 22 B merged with colorimetric pictures containing protein ladder.

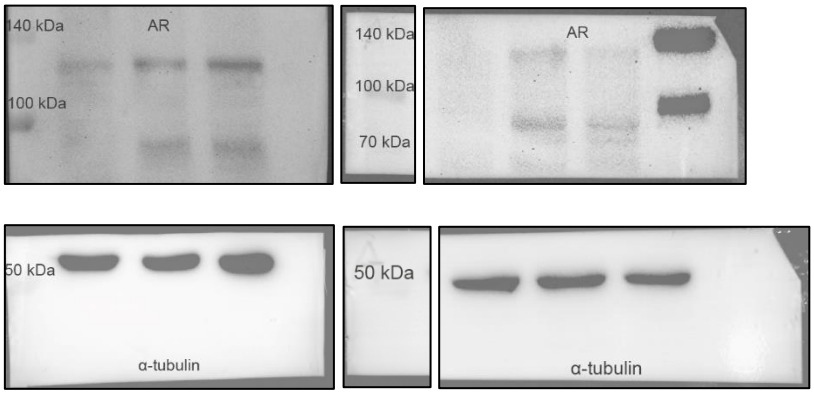

Figure S5. Western blot images used for Figure 22 B merged with colorimetric pictures containing protein ladder.

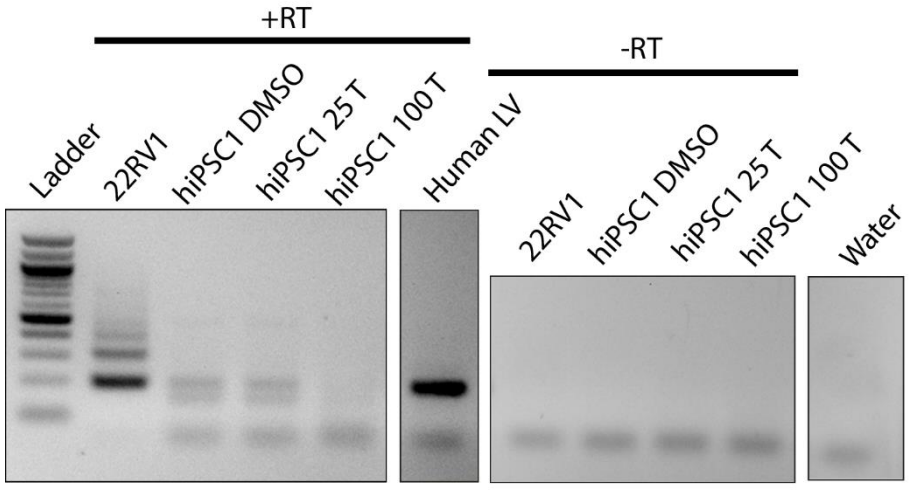

Figure S6. PCR analysis visualization used for Figure 23 C containing +RT (reverse transcriptase), -RT samples, and water control.

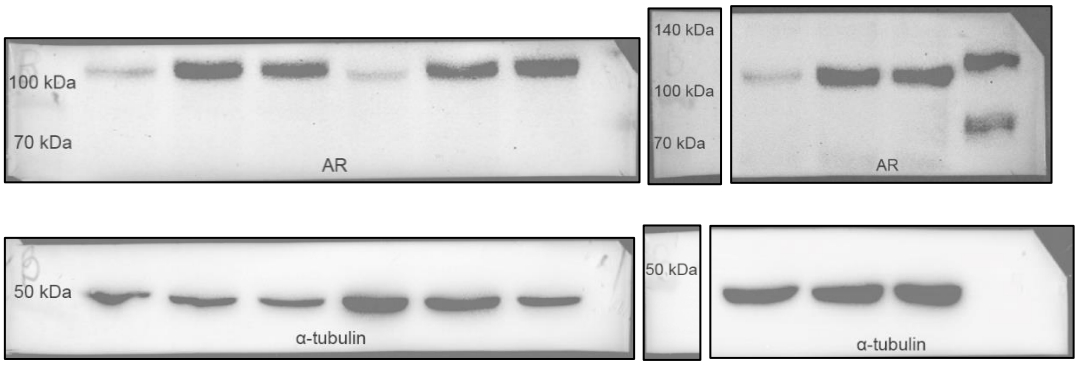

Figure S7. Western blot images used for Figure 24 B merged with colorimetric pictures containing protein ladder.

Table S9. Densitometry analysis values presented on Fig. 22 B. The ratio was measured by dividing the AR value by the α-tubulin value. Next, the average of the control group was calculated and used for further fold change calculations.

Group	AR	α-tubulin	Ratio	DMSO average	Fold change
DMSO1	2.941.225	24.549.279	0,119809018	0,17427105	0,687487
25 T1	28.520.823	29.085.300	0,980592361		5,626823
100 T1	27.198.016	32.072.321	0,848021445		4,866106
DMSO2	3.368.225	11.365.045	0,296367062		1,70061
25 T2	24.061.045	11.837.439	2,032622512		11,66357
100 T2	20.512.338	10.215.368	2,007988161		11,52221
DMSO3	2.517.861	23.611.501	0,106637058		0,611903
25 T3	21.848.187	21.314.773	1,025025554		5,881789
100 T3	25.536.309	11.969.610	2,133428658		12,24201

Table S10. Descriptive statistics of values used for sarcomere length analysis in RhiPSC1-CMs depicted in Fig. 25.

	Sarcomere length			Sarcomere organization score		
	DMSO	25 T	100 T	DMSO	25 T	100 T
Number of values	45	47	46	45	47	46
Minimum	1,790	1,777	1,782	0,05640	0,08690	0,1442
Maximum	2,032	1,988	1,948	0,4807	0,5279	0,4473
Range	0,2420	0,2110	0,1660	0,4243	0,4410	0,3031

Mean	1,891	1,904	1,875	0,2570	0,2997	0,2727
Std. Deviation	0,04626	0,04027	0,04057	0,1110	0,09165	0,07589
Std. Error of Mean	0,006896	0,005874	0,005981	0,01655	0,01337	0,01119

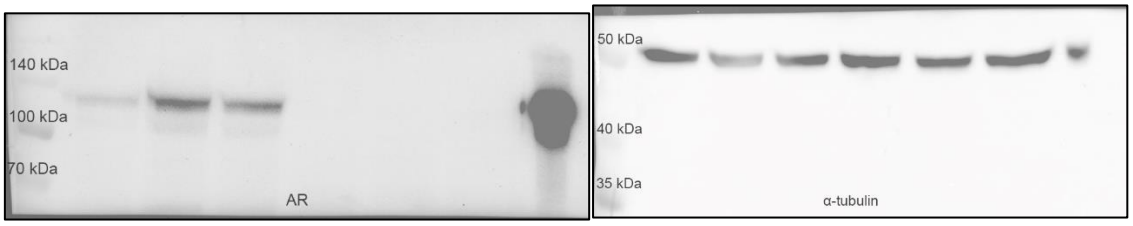

Figure S8. Western blot images used for Figure 28 B merged with colorimetric pictures containing protein ladder.

Table S11. Percentage of cTNT-positive cells of hiPSC1 AR KO cell line after differentiation before selection. Four independent experiments were used for each group of cell seeding numbers.

Number of seeded cells/well	#1 (%)	#2 (%)	#3 (%)	#4(%)
150,000	40,27	58,77	61,07	46,5
200,000	60,36	63,05	60,06	59,58
250,000	59,42	48,16	58,41	57,98
300,000	57,08	58,28	39,48	34,58
350,000	65,46	38,35	55,67	42,73

Table S12. Descriptive statistics of values (%) used for proliferation analysis in RhiPSC1-CMs depicted in Fig. 31. Three independent experiments were used for each group of cell seeding numbers.

	DMSO WT	25 T WT	100 T WT	DMSO KO	25 T KO	100 T KO
Number of values	30	30	30	30	30	30
Minimum	56,56	56,39	56,51	65,37	60,36	54,48
Maximum	74,17	73,84	74,17	83,50	87,43	88,68

Range	17,61	17,45	17,66	18,13	27,06	34,20
Mean	62,67	63,74	63,91	76,82	74,22	74,16
Std. Deviation	4,391	4,811	3,963	5,138	6,561	8,980
Std. Error of Mean	0,8016	0,8783	0,7236	0,9381	1,198	1,640

able S13. Descriptive statistics of values used for sarcomere organization score analysis in WT and KO hiPSC1-CMs depicted in Fig. 32.

	DMSO WT	25 T WT	100 T WT	DMSO KO	25 T KO	100 T KO
Number of values	45	44	45	38	47	46
Minimum	1,804	1,826	1,818	1,818	1,772	1,815
Maximum	2,034	2,132	2,064	2,127	2,186	2,067
Range	0,2300	0,3060	0,2460	0,3090	0,4140	0,2520
Mean	1,915	1,945	1,941	1,972	1,973	1,959
Std. Deviation	0,05321	0,05683	0,06004	0,07628	0,07497	0,05605
Std. Error of Mean	0,007932	0,008568	0,008951	0,01237	0,01093	0,008264

Table S14. Descriptive statistics of values used for sarcomere organization score analysis in RhiPSC1-CMs depicted in Fig. 32.

	DMSO WT	25 T WT	100 T WT	DMSO KO	25 T KO	100 T KO
Number of values	44	44	45	38	47	46
Minimum	0,1390	0,1477	0,1236	0,03672	0,05109	0,04682
Maximum	0,5258	0,7216	0,5853	0,4003	0,2849	0,3942
Range	0,3868	0,5739	0,4617	0,3636	0,2338	0,3473
Mean	0,2975	0,3313	0,3358	0,1686	0,1479	0,2034
Std. Deviation	0,08892	0,1293	0,09184	0,07731	0,05750	0,07953
Std. Error of Mean	0,01341	0,01949	0,01369	0,01254	0,008388	0,01173

Table S15. Data obtained from LC-MS/MS analysis in arbitrary units and used to generate Fig. 39.

Sample	Treatment	Testosterone	Androstenedione	DHT/Androstenediol /Androsterone
Media control	100 nM T	191310	887	-
hiPSC1-CMs 24 hours	DMSO	-	-	-
	25 T	16012	8738	817
	100 T	51475	44477	826
hiPSC1-CMs 48 hours	DMSO	-	-	-
	25 T	3373	15626	3151
	100 T	9212	68913	2813
RhiPSC1-CMs 24 hours	DMSO	-	-	-
	25 T	25133	649	2760
	100 T	159455	2722	2761
RhiPSC1-CMs 48 hours	DMSO	-	-	-
	25 T	25039	941	2361
	100 T	152871	5081	2678